Florida International University

FIU Digital Commons

2022

Photonic Crystal Hydrogels: Simulation, Fabrication & Biomedical Application

Mehenur Sarwar
Florida International University, msarw001@fiu.edu

Follow this and additional works at: https://digitalcommons.fiu.edu/etd

⊙ Part of the Other Biomedical Engineering and Bioengineering Commons

FLORIDA INTERNATIONAL UNIVERSITY

Miami, Florida

PHOTONIC CRYSTAL HYDROGELS:

SIMULATION, FABRICATION & BIOMEDICAL APPLICATION

A dissertation submitted in partial fulfillment of

the requirements for the degree of

DOCTOR OF PHILOSOPHY

in

BIOMEDICAL ENGINEERING

by

Mehenur Sarwar

2022

To: Dean John L. Volakis
    College of Engineering and Computing

This dissertation, written by Mehenur Sarwar, and entitled Photonic Crystal Hydrogels: Simulation, Fabrication & Biomedical Application, having been approved in respect to style and intellectual content, is referred to you for judgment.

We have read this dissertation and recommend that it be approved.

_____
Joshua Hutcheson

_____
Hector R. Fuentes

_____
Jin He

_____
Raj Pulugurtha

_____
Wei-Chiang Lin, Major Professor

Date of Defense: June 29, 2022

The dissertation of Mehenur Sarwar is approved.

_____
Dean John L. Volakis
College of Engineering and Computing

_____
Andrés G. Gil
Vice President for Research and Economic Development
and Dean of the University Graduate School

Florida International University, 2022

DEDICATION

I dedicate this Doctoral Dissertation to my family, my doctoral committee, and my mentor, Dr. Wei-Chiang Lin.

Thanks to my family and friends for their patience and tireless support through the many years of research and investigation.

Thanks to my dissertation committee for providing support, guidance, and critical review of my dissertation research to help me refine and improve my approach and outcomes.

Finally, sincere thanks to Dr. Wei-Chiang Lin for providing incredible mentorship and leadership in helping me overcome numerous obstacles while educating and training me.

`

ACKNOWLEDGMENTS

ABSTRACT OF THE DISSERTATION

PHOTONIC CRYSTAL HYDROGEL:

SIMULATION, FABRICATION & BIOMEDICAL APPLICATION

by

Mehenur Sarwar

Florida International University, 2022

Miami, Florida

Professor Wei-Chiang Lin, Major Professor

Photonic crystal (PhC) hydrogels are a unique class of material that has tremendous promise as biomedical sensors. The underlying crystal structure allows for simple analysis of microstructural properties by assessing the diffraction pattern generated following laser illumination. The hydrogel medium provides elasticity, regenerability, and potential functionalization. Combining these two properties, photonic crystal hydrogels have the potential for sensing physical forces and chemical reagents using a low-cost, reusable platform.

The development of biomedical sensors using this material is limited due to the lack of a method to accurately predict the diffraction pattern generated. To overcome this, a computational model was developed specifically for PhCs and validated against existing analytical models and an existing electromagnetic scattering model in the literature. Assessment of its accuracy in comparison to existing analytical equations and a more generalized multiparticle scattering model in the literature, CELES, found clear alignment. Another challenge is the lack of a technique to assess the specific positions of each particle in the crystal structure non-destructively. To overcome this, a novel fabrication approach

was created using fluorescent particles, allowing subsequent confocal fluorescence microscopy and analyses to extract per-particle position information. This technique was used to directly compare experimental, computational, and analytical results within a single sample.

To demonstrate a novel biomedical application of this material, ultrasound detection was chosen since it would be able to leverage the elastomeric structure of the PhC hydrogel as well as the ability to optically measure small changes in crystal microstructure. The sensitivity, frequency bandwidth, and limit of detection of fabricated PhC hydrogels were assessed using three ultrasound transducers. All transducers created a measurable optical response, with the limit of detection growing steadily with transducer frequency.

These results provide evidence that the platform can be utilized across a variety of biomedical disciplines. For biomedical imaging, this platform can be used for all-optical non-contact ultrasound sensing. For cell and tissue engineering, this platform can provide a novel approach for characterizing and monitoring contractile cells, such as cardiomyocytes. Finally, for environmental engineering, this platform can be used as a continuous monitoring solution for dangerous toxins in environmental waterways.

TABLE OF CONTENTS

LIST OF TABLES

LIST OF FIGURES

ABBREVIATIONS AND ACRONYMS

Photonic bandgap	PBG
Photonic crystal	PhC
Polystyrene	PS
Piezoelectric transducer	PZT
Crystalline colloidal array	CCA
CUDA-accelerated electromagnetic scattering by large ensembles of spheres	CELES
Compute Unified Device Architecture	CUDA
N,N'-diethoxy-4,4'-azobis(pyridinium) hexafluoro-phosphate	DEAP
Scanning electron microscopy	SEM

Chapter 1: Introduction

Statement of Problem

While the naturally occurring photonic crystal structures (e.g., opals, wings of

Parides sesostris butterfly, *Lamprocyphus Augustus* beetle) have captured the attention of

philosophers and the general public for their beautiful colors and opalescent qualities,

laboratory-fabricated photonic crystals are not yet sufficiently investigated for their

biomedical applications. These materials are composed of a self-assembled ordered array

(e.g. square or hexagonally) of particles. Typically, these laboratory-fabricated photonic

crystals are embedded within a polymer substrate, such as a hydrogel. The arrangement

of the particles controls the interaction of light in a wavelength-dependent and

observation-angle-specific manner. Additionally, the transmission of light through these

materials creates a characteristic diffraction pattern (Debye ring) whose properties are

related to the arrangement of the particles, the illumination wavelength, the refractive

index of the particles and medium, and the position of the observation plane.

Functionalization of the photonic crystal can allow the lattice spacing to be modified

through environmental triggers, allowing the utilization of these materials for diverse

sensor applications.

To develop optimal sensors for biomedical applications, it is critical to understand

the physical and functional properties of the underlying material. For photonic crystals,

optimization requires a firm understanding of the arrangement of particles and the impact

of specific fabrication parameters. These parameters can include the density of the

monomer and crosslinker, which affect gel elasticity. The primary goal of this Ph.D.

research is to develop a comprehensive understanding of biosensors based on photonic crystals through the parallel development of experimental and computational approaches.

Many existing sensors can detect external stimuli but each of these approaches has its unique tradeoffs in terms of cost of manufacturing, the requirement of highly trained personnel, long assay times, and high cost of equipment. In contrast, the use of photonic crystal (PhC) based sensors are promising to address many of these challenges. PhC-based sensors can be utilized as point of care devices due to their low cost of manufacturing, portability, high efficiency, selectivity, and sensor regenerability for repeated use.

This dissertation aims to advance the theoretical and practical knowledge of photonic crystals, specifically photonic crystal hydrogels. To advance theoretical understanding, a novel computational model is developed to predict the diffraction pattern formed based on monochromatic illumination of a self-assembled particle array of defined arrangement. This finding creates a substantial opportunity for the proposed project to generate a tool for the scientific community. A self-assembled array is also fabricated using fluorescent particles for convenient imaging using confocal fluorescent microscopy and verifies the simulation's accuracy by comparing the experimental diffraction pattern to a simulated one using the microscopy-derived particle positions as input. Furthermore, existing analytical and literature models are used to validate the computational model. Finally, a valuable application for photonic crystals is explored – ultrasonic wave detectors.

Background and Theory

<u>Fundamentals of Photonic crystal sensors</u>

Photonic Crystal and Photonic Crystal Hydrogel Sensors

Studying the 'photonic crystal hydrogel sensor' requires a deep understanding of

photonic crystals (PhCs). Simply put, PhCs are periodic dielectric structures [1]. The

dielectric constant changes periodically along the axes in PhC materials, which is similar

to a grating. Therefore, the light intensity transmitting through or reflected by PhCs will

be wavelength and observation angle-dependent due to the diffraction effects. For this

reason, they are also classified as a type of photonic bandgap (PBG) materials[2].

Furthermore, when spherical particles self-assemble into a body-centered or face-

centered position, they form a crystalline colloidal array (CCA)[3]. The particle size, the

distance between particles, the lattice constant, and the crystal structure influence the

diffraction pattern they will create. It has been shown that photonic crystal structures can

be engineered to diffract infrared, visible, and ultraviolet wavelengths of light[4].

Hydrogels are a network of polymers that can absorb an extensive amount of

water and can reversibly transition between a de-swelling and a swelling state[5]. This

drastic change of hydrogel is referred to as volume collapse or phase transition and can

be influenced by chemical stimuli (e.g. pH[6], molecular species[7], and ionic

strength[8]) or physical stimuli (e.g., pressure[9], sound[10,11], temperature[12],

light[13], electric and magnetic field[14]). Therefore, when photonic crystal structures

are combined with a hydrogel polymer backbone, the fabricated "photonic crystal

hydrogel" (PhC hydrogel) can be utilized to detect external stimuli, contributing to the

opportunity to develop colorimetric sensors. This is due to the direct relationship between hydrogel swelling behavior and the lattice spacing of the embedded particle array.

Physics Relating Interaction Between Light and Photonic Crystals

In 1887, Lord Rayleigh first described the phenomenon of light reflection by 1D photonic crystals (dielectric mirror). However, it was not until 100 years later that the theoretical explanation was confirmed by E. Yablonovich [15] and S. John [16]. To explain the constructive and destructive interference that occurs in PhC materials requires careful examination and understanding of the principles of solid-state physics and electromagnetism. PhCs appear iridescent due to their inherent ability to diffract electromagnetic waves in the visible wavelength region. This phenomenon is governed by Bragg-Snell's law, that is $m\lambda = 2d\sqrt{n_{eff}^2 - sin^2\theta}$, where m is the order of diffraction maximum, λ is the wavelength of reflected light, n_{eff} is the effective refractive index of the periodic structure, d is the lattice spacing of the crystal in the direction of light propagation, and "θ" is the angle of incidence of light with respect to the normal[17–19]. This principle lets us realize that any change in the PhC materials, which affects the average refractive index or spacing between the crystal structure, will cause a change in the reflection wavelength. The narrow bandgap of the PhC material also generates an angle-specific reflection maxima for each illuminating wavelength. Additionally, using Bragg diffraction of visible light $\lambda_{max} = 2dn_{eff}$, the position of the maximum reflection peak of the photonic hydrogels can be determined, which is previously used by Jia et al[20].

Existing studies also point out another optical phenomenon of PhC besides the observation-angle dependence of the reflection spectral peak under broadband illumination. When a two-dimensional photonic crystal (2D PhC) is illuminated with monochromatic light, a Debye ring pattern is produced on a parallel screen behind the sample. The diameter of the Debye ring D can be estimated by the following two equations: $D(\lambda) = 2h \times \tan(\theta)$ and $\theta = sin^{-1}(\frac{2\lambda}{d\sqrt{3}})$. Here d is the particle spacing of the 2D PhC, h is the distance between the PhC and the screen, and the incident angle is zero [21]. In this dissertation, it is demonstrated that this equation provided in the literature is only true for hexagonal particle arrays. Additionally, the Debye ring becomes diffused for an imperfect PhC with disordered particle arrangement due to the variability of interference maxima caused by this arrangement disorder.

To scientifically explain the interaction between light and PhC, both light scattering and diffraction theories must be considered. Mie scattering theory is commonly used to describe the scattering event of a single spherical scatterer. However, it is not directly applicable to PhCs because PhCs contain many orderly-closely packed spherical particles. In other words, the light scattering event of a spherical particle on PhC is affected by the surrounding particles [22]. Moreover, the orderly packed particles in PhC also behave similarly to the grooves of a grating; the forward scattered light by the particles will interfere with each other either constructively or destructively (i.e., diffraction) and hence produce a Debye ring [23,24]. Therefore, light-PhC interaction is inherently a complex hierarchical process. Currently, there is not a computational model suitable to describe this interaction within PhC hydrogels.

*Effects of Intrinsic PhC Properties on Optical Characteristics *

While the diffraction peaks observed in X-ray crystallography are highly analogous to peaks observed in PhC, the former one is in the angstrom range, whereas the latter is in the sub-micrometer range. If the periodicity of the particles is proportional to the wavelength of light, a specific bandwidth of light is reflected at each observation angle. Three main factors which are regarded to affect this behavior are (1) the change in refractive index in solid/void spheres and the material surrounding the spheres (2) the distance between the spheres or lattice spacing, and (3) the area (2-D) or the volume (3-D) occupied by the spheres in comparison to surrounding phase. Therefore, external stimuli that can alter these parameters will result in a reflection peak shift and hence are often referred to by scientists as "tunable materials." Furthermore, by changing the size of the particle, it is possible to fabricate different colored PhC materials[25].

The properties of a Debye ring are intricately connected to the experimental conditions. According to Braggs Law, $m\lambda = 2nd\sin\theta$, the Debye ring diameter increases as (1) illumination wavelength increases or (2) particle center-to-center spacing decreases. Additionally, the thickness of the Debye ring becomes larger when the intrinsic disorder existing in the PhC structure elevates [21]. The appearance of the Debye ring as a set of discrete points versus a continuous circle is based on whether the PhC is a perfect crystal or a polycrystal composed of randomly oriented crystallites [26]. When in the polycrystal state, each crystallite contributes to a set of discrete points, but due to their random orientations a superposition occurs at the observation plane, generating the appearance of a ring. Finally, the size of the scatterers (in this case, particles) controls the implementation of Mie theory, affecting the intensity of the first-

order diffraction ring and any secondary rings that form concentrically outside of the primary ring.

Signal Collection from Photonic crystal sensors

Transmission-Mode Approaches Utilizing PhC

A valuable application of photonic crystals has been found in the measurement of glucose. While the team reported a change of color of the functionalized hydrogel (from reflection mode), they relied on the characteristic of the Debye diffraction ring (from transmission mode) for measuring glucose level. Furthermore, they relate the shrinking of the hydrogel to decreasing of polystyrene particle spacing, hence increasing the size of the Debye diffraction ring. The size of the Debye ring was measured with a homemade portable optical reader. The forward diffraction angle (θ) is defined in terms of gel to screen distance (h) and radius (r) of the Debye diffraction ring, which is $\theta = \tan^{-1}$ (r/h). Lan *et al.* used the following formula to calculate particle spacing, $d = \frac{2\lambda}{\sqrt{3}\sin(\theta)}$ [27]. According to their report, the particle spacing decreased from 849nm to 769 nm when glucose concentration increased from 0.1 mmol^{-1} to 10 mmol^{-1}.

Similar to Lan's group, Qi et al. utilized the spacing formula to determine the concentration of Dipterex, a pesticide widely used in the agricultural field [28]. Dipterex is considered a nerve agent and extremely harmful to humans. By functionalizing a 2D PhC with acetylcholinesterase, it becomes sensitive to the concentration of Dipterex by modifying the particle spacing. The lattice spacing was found to be inversely proportional to the concentration of the logarithm of the Dipterex concentration.

Urease functionalized 2-D PhC hydrogel with embedded polystyrene particle has been utilized to detect urea and urease inhibitors [29]. To monitor these targets, this research group also relied on the diameter of the Debye diffraction ring. Urease is an enzyme that produces OH^-, NH_4^+, and HCO_3^-. Thus, this increases the pH of the reaction media and results in a volumetric transition of the hydrogel. During the swelling of the hydrogel, the embedded polystyrene particle also moves away from each other, increasing the particle spacing. The shrinking of the hydrogel occurs when the active site of the hydrogel gets blocked by an enzyme inhibitor, reducing the particle spacing. The hydrogel also goes through a colorimetric change that can be visible at a specific angle.

Reflection-Mode Approaches Utilizing PhC

Reflection-mode approaches rely on the peak wavelength shift of reflected light under broadband illumination to detect analyte concentration change [30–34]. For these sensors, the change in color relies on the volume change of the hydrogel, influencing the particle spacing. Different particles may affect the structural color of the hydrogel differently. Jia *et al.* used Fe_3O_4 nanoparticle embedded hydrogel film, which they explained displayed brilliant structural color compared to more common polystyrene embedded films. When magnetic particles are used, it enables the use of an external magnetic field, hence, affecting the arrangement of the particles and improving the response time of the sensor[20]. The reflection peak redshifted almost 202 nm in response to a pH change from 2 to 7. The detector (USB4000, Ocean Optics Spectrometer) was placed at a fixed 90-degree angle to collect reflectance change of the hydrogel film.

1-D photonic crystal gas sensors have also recently been engineered and they process an ultra-high sensitivity (S = 1.9×10^5 nm/RIU), and a low detection limit (DL = 1.4×10^{-7} RIU) compared to existing gas sensors [35]. This gas sensor contains a gas cavity sandwiched between a porous silicon photonic crystal and silver layers. The peak wavelength is modulated due to alteration of the effective refractive index of the 1D PhC structure or surrounding medium, which occurs when the chamber is filled with gas. The authors utilized Tamm plasmon resonance which can be created by placing a metallic layer in front of a 1D photonic crystal layer [36]. Tamm plasmons, which are explained as electromagnetic modes within distributed Bragg reflector (DBR) and a noble metal (e.g., gold), can be excited at normal incidence and utilized as a convenient platform for enhanced light-matter interaction at the nanoscale.

Additionally, in 2017 Harvard University and two other universities' researchers jointly reported a new type of photonic crystal hydrogel sensor with a stopband that can be modulated across the entire visible spectrum [37]. The sensor has two parts - a core and a shell. The core is made with polystyrene particles (controls scattering); the shell is of poly(N-isopropyl acrylamide- co-bisacrylamide-co-acrylic acid, pNiPAm-BIS-AAc) (controls interparticle spacing). These two parts are assembled to form a highly reflective sensor using the depletion attraction force induced by the presence of non-adsorbing polymer. The temperature change from 20˚C to 40˚C causes the reflection peak to blue shift from 650 nm to 440 nm. This temperature sensor also demonstrates a reversible and reusable characteristic, cooling the sensor causes a reversible shift in peak wavelength.

Choosing Between Transmission and Reflection Measurement Scheme

Comparing transmission and reflection techniques, transmission methodologies generating a Debye ring are far superior to be utilized as point of care devices. Transmission techniques require a simple laser pointer and a method of measuring the size of the generated diffraction ring on a screen. In contrast, reflection-mode measurements require an expensive setup utilizing a spectrometer, a broadband light source, a reflectance fiberoptic probe, a computer, and software for data visualization. Therefore, a transmission-based detection system is more practical, cheap, portable, and convenient to be utilized in point of care settings.

Existing Methodologies for Fabricating PhC Sensors

While many methods have been published for the fabrication of PhC materials, common techniques include dip coating, spin coating and centrifugation-assisted techniques [38–41]. Alternative methodologies also include the Langmuir-Blodgett method to create thin films/monolayers [42–44], assembly at liquid-liquid interface technique using surface tension and capillary forces to create thin films/monolayers [45–47], electrophoretic methods [48,49] using charged particles to create thin films/electrode patterning, magnetic-field assisted techniques [50,51], and micro-confined assembly for microfluidic devices [52,53].

Dip Coating

1-D PhC materials are fabricated by stacking materials with different refractive indices. Researchers used a dip-coating method to coat glass substrate with SiO_2

alternating with TiO_2, followed by a heating protocol to cure the sensor. The thermal treatment is essential to obtain a desired orderly porous structure. This sensor was developed to detect dihexadecyl phosphate (DHDP): DHDP binds with Titania sites and changes the refractive index of that layer, causing a dramatic change in optical properties of PhC [54]. However, if the goal is to achieve a thicker photonic crystal layer, the dip coating method is not always suitable because this method provides too thin of a coating layer on the substrate. To overcome this, a high concentration of dipping solution may be used[55].

Spin Coating

Bragg stacks are designed to have alternating materials of low and high refractive indices[56]. When incident light interacts with this type of layered structure, it produces brilliant color due to stopband reflection. Such layers/stacks can be achieved by spin coating and the thickness of the layers can be controlled by the spinning speed and the concentration of the deposits. Hydrogel based Bragg stacks were previously fabricated[57–59]. In one example, TiO_2 nanoparticles embedded PMMA-co-pHEMA-co-PEGDMA polymer was used for sensing application[60]. Another group reported fabrication of temperature PhC sensors by spin coating photo cross-linkable copolymers: poly(paramethyl styrene) and poly(*N*-isopropyl acrylamide)[61]. The spin coating approach has several limitations, (1) spin coating and stacking requires careful processing and complex long drying and annealing steps (2) angle of observation is fixed and therefore the detector has to be carefully designed for wavelength shift monitoring (3) Bragg stack requires low and high refractive index materials stacking. If the stacking materials are not compatible, such as when one layer is chemically reactive with another,

this would result in morphological distortion of the layers[55,62]. Heat treatment is also

a required step in the spin coating process, but this can cause substantial damage to the

PhC material.

Centrifugation assisted

A damage-free, robust and tunable PhC film fabrication by centrifugation assisted

method has been reported by Fan et al. [63]. Centrifugation approaches have multiple

advantages: (1) the cracking of the structure can be avoided as the spheres spontaneously

self-assemble during centrifugation due to capillary force forming a compact film, and

(2) the centrifugal force relaxes the spheres hydrophobicity letting the spheres adsorb to

each other.

Review of 2D and 3D PhC Fabrication Processes

For the fabrication of 2D PhC, Coukouma et al. relied on self-assembly of

nanoparticles on liquid-liquid interface[64]. The assembled particles were then

transferred to a glass substrate by inserting the glass and carefully lifting it. Later, the 2D

PhC was infiltrated with polymer solution to create 2D PhC hydrogel construct. To

fabricate 3D PhC hydrogels the self-assembly process takes place because either of

gravity and/or capillary and/or centrifugal and/or electrostatic or magnetic field would

cause close-packed or non-close packed assembly of the nanoparticles[65]. Methods of

fabrication involve different complex processes such as Brownian motion, solvent

evaporation, and crystallization (i.e., nucleation and crystal growth)[66]. A combination

of face-centered, and hexagonal close-packed arrangements can be seen within one 3D

PhC structure. The entropy difference between these two arrangements may result in

planar stacking dislocations and other defects in the crystal structure [67]. The PhC

hydrogel fabricated by Mu et al. arranges nanoparticles in a 3D polymer space [68].

However, they removed these particles in order to create 3D inverse opal hydrogel

structure. These researchers fabricated the PhC hydrogel in a bead shape (3D) rather than

a film shape (2D). This is advantageous as the bead shape for instance, facilitates staining

procedures. These beads can be vortexed/shaked with staining solutions easily to enhance

the diffusion process of the staining solution, thus improving the staining quality.

Sensors Based on Photonic Crystals

Biochemical Sensing

Existing studies of photonic crystal sensors for the detection of analyte typically

show either a bathochromic (red) [69,70] or hypsochromic (blue) shift [69,71,72] upon

binding of an analyte to the PhC material. This shift in the reflection in visible

wavelength provides a significant advantage, contributing to the field of colorimetric

sensor development for visual detection. The Asher group from the University of

Pittsburgh is one of the pioneers to utilize PhC materials for sensor development. Their

contribution brought us novel sensors for the detection of lectin protein[73] , 2,4,6-

trinitrotolune[70], *Candida albicans*[72]*,* glucose[74,75], pH[76,77], ethanol[77],

organophosphate[78], Pb^{2+}[79] etc. In the following paragraph the detection mechanism

of these analytes is briefly described.

Briefly, in response to lectin protein[73], *Candida albicans*[72]*,* the volume of the

hydrogel, and hence the embedded particle spacing would change, which can be

quantified by the diameter of the Debye ring created by the sensor under monochromatic

laser illumination. The interparticle spacing of the glucose sensitive hydrogel changes

due to the rising concentration of the glucose, which alters the forward diffraction color from red, through yellow, to green[74,75]. A novel PhC sensing material has been reported which can semi-quantitatively measure glucose level from a urine sample [80]. This sensor also has been tested clinically on a random selection of 20 patients with or without diabetes. The PhC materials have huge potential to be utilized as a non-invasive, real-time, and reusable sensor. 2-D PhC hydrogel sensors for glucose detection has been recently developed by functionalizing polyvinyl alcohol with 4-boronobenzaldehyde, which changes color from red through yellow to green as the glucose concentration increases from 0 mM to 20 mM. To explain the scientific reason for the color change due to glucose, researchers relies on Flory's theory. According to Flory, the total osmotic pressure (π_t) is the sum of three factors: (1) the osmotic pressure from the polymer absorbing solvent- π_{mix} (2) the osmotic pressure from the elongating polymer - π_{el}, and (3) the osmotic pressure from the non-uniform presence of counter-ions (Donnan potential) - π_{ion}. Therefore, $\pi_t = \pi_{mix} + \pi_{el} + \pi_{ion}$.

Since the tear specimen contains a high concentration of ions, the distribution of ion is not non-uniform and therefore, $\pi_{ion} = 0$. The mechanism of glucose detection thus depends on the typical PhC mechanism - swelling or shrinking ability of the functionalized-polystyrene nanoparticle embedded polymer.

The increase in the level of pH causes ionization of the carboxyl group covalently attached to the gel, and thus the counterions start to mobilize inside the gel[76,77]. This reaction results in the swelling of the gel and a forward diffraction red shift. The high concentration of ethanol causes swelling of the hydrogel, which decreases the overall refractive index of the hydrogel and solvent mixture below to the Silica[77]. Thus,

refractive index mismatch increases between the hydrogel solution medium and silica, overall shifting the diffraction wavelength.

To determine the level of 2,4,6-trinitrotolune researchers dependent on the hydrogel color change due to swelling of the particle and increase in the hydrogel refractive index [70]. For organophosphate detection, enzyme organophosphorus hydrolase reacts with methyl paraoxon, which produces two protons in addition to other products [78]. The protons then react with the phenolates bounds on hydrogel, and creates an unfavorable mixing environment for the hydrogel, which results in shrinking of the hydrogel. Due to this shrinkage the lattice constant of the hydrogel decreases, and blue shifts the diffracted light. The diffraction shift is proportional to the concentration of the methyl paraxon. A optrode sensing device consists of a Pb^{2+} sensing PhC hydrogel film was utilized to detect Pb^{2+}. Similar to the other sensors which change color due to the change in volume of the hydrogel, a red diffraction shift is observed.

Yetisen et al. utilized laser pulses (532 nm) on ordered silver nanoparticles embedded phenylboronic acid-functionalized hydrogel to produce off-axis Bragg diffraction gratings [81]. These gratings consist of silver nanoparticles polymerized with a functionalized (phenylboronic acid) hydrogel. The developed sensor was reported to have excellent functionality, could be reused a minimum of 400 times without compromising its detection accuracy, had a response time of 5 min, and could reset to baseline in approximately 10 s. The sensor's sensitivity towards glucose permits the use of this sensor to diagnose glucosuria in diabetic patients and was reported to have improved performance compared to high-throughput commercial devices.

In another study, a 2D PhC based microcavity biosensor for protein detection was developed on a silicon-on-insulator wafer [82]. This sensor could detect protein as small as ~2.5 fg (1fg =10^{-18} kilograms). Additionally, a multiplex mycotoxin detection technique had been reported by Deng et al [83]. Instead of using a hydrogel platform, this group surface-modified silica microspheres with three different artificial mycotoxin antigens and created suspension arrays of PhC. The detection scheme involved centrifuging the PhC microspheres with fluorescein isothiocyanate (FITC) labeled antibodies (Abs) of these mycotoxins. A fluorescent scanner was used to detect the signal and a low detection limit of 0.5, 1, and 0.8 pg/mL for Aflatoxin B1 (AFB1), fumonisin B1 (FB1), and citrinin (CIT), respectively, was reported. The detection time was below 3 hours and the achieved results conformed with the classic enzyme-linked immunosorbent assay (ELISA) method.

Mechanical Sensing

Since PhC properties are highly dependent on particle spacing within the embedded crystal structure, they are commonly used for mechanical sensing applications. One common implementation is through the fabrication of photonic crystal fibers, which appear in design similar to fiberoptic cables but replace glass fibers with air waveguides [84]. Geometric tuning of the design allowed for a wide variety of sensing capabilities, including twist / torsion sensing [85] [86] and transversal load sensing [87] [88]. These fibers have also shown promise for the measurement of frequency and amplitude of vibration [89][90] – a valuable tool for detecting and monitor structural damage on various critical mechanical assemblies such as airplane rotor blades.

Mechanical sensing is not only possible for PhCs fabricated as fibers – it is also possible for more traditional layered 2D structures. In this configuration, one valuable application which has emerged is displacement sensing, which could measure displacement as small as 115 nm due to modulation of the PhC pore structure [91]. 2D PhCs have been shown to provide force sensing when fabricated as a cantilever within an optical nanoelectromechanical system (NEMS) [92] and strain sensing when fabricated as a 2D PhC nanocavity resonator [93].

Gas Sensing

Photonic crystal fibers have been found to be highly suitable for gas sensing, since the periodic air channels allows for detection of gases with a unique refractive index when diffusing within the PhC fiber structure. One research team developed a method for measuring methane concentration by infiltrating the PhC fiber with cryptophane E, which when interacting with methane creates a shift in the resonant wavelength of the photonic crystal microcavity [94]. Gas sensing is not limited solely to photonic crystal fibers, as many advancements have been made with porous silicon PhCs, multilayer PhC films, colloidal self-assembled PhCs and inverse opal PhCs [95].

Research Questions

This dissertation is composed of three critical research questions, each of which encompasses a unique rationale and methodology and hence forms a specific aim:

1. Can a computational simulation be developed which combines diffraction and Mie theories to predict the diffraction patterns of photonic crystal hydrogels with various particle arrangement?

17

a. Will the diffraction pattern have the expected response to variation in experimental conditions, such as illumination wavelength and particle spacing?

b. Will the diffraction pattern change due to the particle arrangement? Does this match the theoretical predictions?

c. Will incorporation of Mie theory impact the distribution of scattered light?

d. Will the simulation demonstrate the expected difference between a perfect crystal and polycrystalline structure?

e. Will the diffraction pattern change due to microscopic error in crystal structure?

f. Will the simulation produce results comparable to existing analytical equations, published models and published experimental results?

2. Can a 2D PhC hydrogel be fabricated with fluorescent particles to facilitate analysis using conventional fluorescence microscopy?

a. Can the specific position of each particle in the fabricated PhC hydrogel be used to link experimental results to simulated results?

b. Can the unique positions of each particle be used to assign an index that characterizes the relative proportion of hexagonal versus 2D crystallite configurations? Can this index link experimental results and theoretical results?

3. Can the fabricated PhC hydrogel be used for ultrasonic detection, due to being elastomeric and having a pressure-sensitive effective refractive index?

a. What is the frequency response/bandwidth of the fabricated PhC when exposed to pulsed ultrasound waves?

b. What is the sensitivity of the fabricated PhC to ultrasonic pressure?

c. What is the limit of detection of ultrasonic pressure of the fabricated PhC?

Research Question 1

Can a computational simulation be developed which combines diffraction and Mie theory to predict the diffraction patterns of photonic crystal hydrogel with various particle arrangements?

Rationale

While the utilization of photonic crystal hydrogel as a sensor is not a novel concept, researchers have not yet attempted a computational simulation to understand how a unique arrangement of particles influences the associated diffraction pattern. Therefore, a computational model was developed to predict the diffraction patterns of PhCs with various particle arrangements.

Hypotheses

- A PhC computational model can be built using diffraction and scattering theories.

- This computational model can predict diffraction patterns of PhCs with various 2D particle arrangements.

- Simulated results from the computational model will match theoretical expectations resulting from varying particle configurations, particle spacing, illumination wavelengths, microscopic error and macroscopic error.

Novelty & Impact

This computational model is novel and the scientific literature does not provide a specialized tool simulating crystal structures and subsequent diffraction resulting from transmission-mode PhC hydrogel illumination. This model can be used to fine-tune design of a sensor based on predicting the size of the resulting diffraction pattern (Debye Ring) on an observation screen at a defined location. Furthermore, this model can assist in troubleshooting challenges in PhC design by allowing researchers to input a specific collection of discrete particle coordinates instead of using built-in pre-designed particle configurations.

Research Question 2:

Can a 2D PhC hydrogel be fabricated with fluorescent particles to facilitate analysis using conventional fluorescence microscopy? Can the specific positional characteristics of each fabricated gel be used to link experimental results to the derived simulation?

Rationale

While approaches have been reported in the literature to fabricate PhC hydrogels, many require expensive tools and long fabrication processes - sometimes even weeks. To achieve a high quality hydrogel sensor, researchers must choose from a variety of particles (e.g., metal particles [96], silver particles [97] and polystyrene particles [69], etc.) and polymer agents (e.g., poly(hydroxyethyl methacrylate [69], poly(*N*-Isopropylacrylamide [11] and poly(2-hydroxyethyl methacrylate) [98], etc.). To date, the scientific field still lacks a convenient method for the fabrication of high-quality PhC whose particle configurations can be readily assessed. The incorporation of fluorescent

particles provides a distinct advantage to this process: the morphological and structural properties of the hydrogel can be reliably monitored through a fluorescent microscope. By using large fluorescent particles (i.e., diameter greater than 900 nm), validation of PhC structure no longer will require the use of SEM. SEM-based monitoring of the final structure of the polymerized PhC is not well-suited due to the need of a vacuum chamber (i.e., it exerts physical stress on hydrogel and causes changes in morphology) and gold sputtering, which substantially degrades the quality of the substrate.

Hypotheses

- A 2D PhC can be composed of fluorescently-labeled particles while still retaining the optical properties of a traditional PhC, such as producing the Debye diffraction ring under laser illumination,

- A 2D PhC composed of fluorescently-labeled particles will allow monitoring of its configuration with fluorescence microscopy, a far more accessible and less expensive tool than conventional SEM.

- Fluorescence microscopy will allow the extraction of the unique position of each imaged particle, allowing for the PhC to be indexed based on its relative proportion of hexagonal vs 2D crystallites.

- The unique position of each imaged particle can serve as an input into the developed computational model to assess the degree to which an experimental debye ring's characteristics can be predicted using the computational model.

Novelty & Impact

Due to the challenge of characterizing individual particle positions within a PhC hydrogel and the lack of an established computational model, this work is novel in its linkage of experimental and simulated diffraction outcomes. While the scientific literature commonly compares experimental outcomes to theoretical outcomes based on a perfect crystal structure, this work provides a significant and novel improvement by generating an index which can provide a more accurate theoretical outcome based on the relative proportion of the particle configurations. This work is very impactful as it introduces a significant improvement to existing theoretical frameworks and provides tangible evidence as to the accuracy of the developed computational model.

Research Question 3

Can the fabricated PhC hydrogel be used for ultrasonic detection due to being elastomeric and having a pressure-sensitive effective refractive index?

Rationale

Understanding the link between the particle spacing and change in diffraction patterns requires testing the PhC hydrogel in the presence of external stimuli. Stimuli, which create a change in the particle spacing, will modify the forward diffraction pattern. Many researchers have used PhC hydrogel for the detection of analytes, but the use of PhC hydrogel to monitor pressure is still limited[99–101]. A potential application that was considered includes using the hydrogel as a scaffold for growing contractile cells and monitoring their contractility through a rhythmic change in the PhC hydrogel properties. Another potential application is embedding it at the tips of fingers of robotic hands to

22

provide pressure feedback. PhC pressure sensors are an intriguing application due to their unique combination of elasticity, sensitivity and regenerability that other commercial options cannot match. One of the greater limitations of the currently available pressure sensor is their limitation to register consecutively exerted pressure within a short time [102]. PhC pressure sensors would be thin-film, soft, reusable optical sensors (hence, not affected by electronic interference)[29,103,104]. Furthermore, their responsivity can be readily tuned by modifying their fabrication parameters by controlling the degree of cross-linking. Finally, as an optical sensor, they are capable of both semi-quantitative (e.g. colorimetric) and quantitative (e.g. reflectance mode: spectral reflectance, transmission mode: debye ring characteristics) measurement. An exciting potential application for PhCs as ultrasonic detectors is as part of an all-optical ultrasound platform, using a pulsed laser to induce an ultrasonic signal and a PhC to transduce it for detection by a steady-state laser.

Hypotheses

- In response to ultrasonic pressure, the cyclic modulation of the effective refractive index due to alteration of particle spacing will create a measurable change in the intensity of optical diffraction, which can provide an ultrasound monitoring methodology.

- A PhC functioning as an ultrasound transducer will have a measurable frequency bandwidth, pressure sensitivity and limit of detection.

- Incorporation of the computational model will allow prediction of the optimal photodetector location to capture the intensity fluctuations resulting from the ultrasonic wave.

Novelty and Impact

In recent years, PhCs have begun attracting interest for ultrasound detection. The literature currently focuses on PhCs with sub-micron particles, typically in the 200-500 nm range. This dissertation examines the unique characteristics of PhC hydrogels with micron-scale particles, whose frequency bandwidth of responsivity can provides an additional option for sensor development where properties are required that are not met by current solutions.

Chapter 2: Computational Simulation of PhC Hydrogel

Introduction

<u>Photonic Crystal Debye Rings</u>

PhCs can be engineered to sense biological or chemical analytes and physical parameters from its local environment through geometric changes in their underlying crystal structure. Of the various methodologies available to characterize the crystal structure, the formation of a Debye ring under collimated monochromatic illumination and measurement of its size is the simplest [105]. To date, there are no computational models available in the published literature which allow simulation of the diffraction pattern of PhCs based on parameters of an input crystal structure and defined experimental conditions. Analytical solutions are only available for well-defined perfect crystal structures (i.e. hexagonal or 2D) with no microscopic or macroscopic error – a perfect case which does not exist in manually fabricated PhCs. Without a computational model which can consider diffraction patterns from arbitrary positions of particles in a PhC, experimentally generated PhCs will be extremely difficult to optimize for sensor design. The proposed computational model solves this problem and utilizes two theories – Braggs Diffraction and Mie Scattering – to simulate Debye ring generation from photonic crystals due to interference and scattering of light.

<u>Braggs Law and Interference</u>

Braggs law is a special case of Laue diffraction which explains the presence of periodic 'Braggs peaks' resulting from interference following crystal illumination. Laue diffraction describes the generic scattering of waves during crystal diffraction while

Braggs diffraction considers interference – specifically angles for coherent and incoherent scattering. Interference describes the superposition of waves when incident at the same point, whereby the resultant amplitude at the point is equivalent to the vector sum of the individual wave amplitudes. When interfering, waves interact through a combination of constructive and destructive forces based on the offset of their phases [106]. When phase differences occur at multiples of 2π, the waves exhibit pure constructive interference, providing the strongest signal at the target position. These calculations provide instantaneous estimations of energy flux in an area – defined as the energy per unit area per unit time passing through a plane located perpendicular to the wavefront [107]. Measurement of this flux over time – such as by a measuring device – requires a time average over a complete cycle of the electromagnetic wave. This calculation converts energy flux to Intensity, a parameter which provides a more stable reflection of the energy level at that point.

Interference is a key phenomenon for understanding Debye rings since the intensity of light at a specific point on an observation screen is dependent on the combination of constructive and deconstructive interferences from the numerous paths from each illuminated particle in the crystal to the specific point on the screen. This realization was first understood by Lawrence Bragg in 1913 who identified the relationship between the location of X-ray interference maxima and particle spacing as dependent on constructive interference [108]. X-ray wavelengths are compatible with the very small inter-atomic distances within solid crystals, just as visible light wavelengths are compatible with the much larger spacing of particles within a photonic crystal hydrogel. Use of interference as an underlying component of the proposed model is

beneficial as it takes into consideration the effect of constructive and destructive interferences due to pathlengths traveled by light. This analytical framework is insufficient on its own since it does not consider the preferential scattering angles of light.

 Scattering

Consideration of interference on its own may lead to the false conclusion that scattering is isotropic – implying that it is equally likely to scatter in any direction. While there are many scattering models which exist, the relevant one for the proposed application is Mie Scattering theory, also known as the Lorenz-Mie-Debye solution to Maxwell's equations [109]. Mie scattering describes scattering of an electromagnetic plane wave by a homogeneous sphere when the size of the scattering particles are only a few orders of magnitude larger than the incident light [110]. This is appropriate in the proposed computational simulation since the range of visible illumination (400-700 nm) is only approximately a single order of magnitude less than the 2 micron-sized spherical particles utilized. An additional assumption of Mie theory is that the sphere has a refractive index unique from the medium surrounding it, which is satisfied based on the embedding of the crystal within a cured hydrogel medium. Incorporation of Mie theory allows for the calculation of the angular dependence of scattering intensities. This model is extremely valuable for the proposed computational model since it identifies the probabilistic distribution of energy on the observation screen independent of interference.

The specificity of Mie theory is also one of its core limitations. As it is only a unique solution to Maxwell's equations it only perfectly applies to scattering of a single homogeneous sphere. Experimentally, scatterers are typically not perfect spheres nor

homogeneous. To resolve this limitation, other groups have developed multi-sphere scattering simulations. One option, CELES, provides a MATLAB/CUDA implementation that generates the scattered electrical field resulting from the superposition of spherical vector wave functions [111].An alternative approach, BIMSIM, calculates the electromagnetic field resulting from interactions with numerous spherical scatterers while taking into account the focusing optics and detector [112].

Proposed Computational Model

The proposed computational model considers both interference and scattering phenomena to simulate the intensity of distinct points on an observation screen located parallel to the photonic crystal and perpendicular to the incident laser light source. This model takes into account the experimental setup (e.g. incident light wavelength, distance of observation plane from photonic crystal) and photonic crystal properties (e.g. distinct locations of each particle, particle diameter, particle refractive index, hydrogel refractive index). Since particle positions can be included into the model individually, this model can be used to assess the resulting diffraction pattern from different particle arrangements (e.g. hexagonal, 2D, centered-square), microscopic positional error, macroscopic error (polycrystal structures) and even experimentally-collected particle positions. This chapter will verify that the computational model matches theoretical expectations for each of these scenarios and compare its outcome with a more generalized multiparticle Mie scattering simulator available in the scientific literature, CELES.

Methods

<u>Computational Model Development</u>

To simulate the creation of a Debye ring, three steps were required. First, a collection of input parameters and system characteristics were defined which characterized the PhC hydrogel to generate defined positions and geometric orientations. Second, simulation conditions were defined which characterize the observation screen size and location as well as the illumination conditions. Using this information, simulation of pathlength differences and phase shifts of each scattering event during illumination were used to identify the constructive and destructive interferences on the observation screen, considering both Bragg's law of diffraction and Mie theory.

Defining PhC Hydrogel Properties

PhC hydrogel properties can be subdivided into particle parameters, medium parameters, and particle arrangements. The particle parameters considered were the particle size and particle refractive index and the medium parameter considered was the medium refractive index. Particle arrangement is more widely configurable, with control over the center-to-center particle spacing, the particle arrangement and the presence of crystal error. Supported particle arrangements include hexagonal array, 2D array and centered square array. The unit cell for each configuration and its lattice geometry is provided in Figure 2.1.

Figure 2.1 Simulation Lattice Geometries. To generate each of the three lattice geometries available in the simulation, the following particle spatial relationships were utilized to generate the resulting unit cell. A simulated particle array demonstrates the unit cell within the generated crystal structure.

Crystal error as a parameter is used to provide control over whether the crystal is 'perfect' or has the presence of microscopic and/or macroscopic error. A perfect crystal has identical particle spacing throughout its entire structure with no defects. Both microscopic and macroscopic error represent unique types of particle defects. Microscopic error refers to error in the center-to-center particle spacing. To incorporate microscopic error, the position of each particle was modified by a randomly generated amount within a user-defined range. For example, a perfect crystal with 2 µm particle spacing and an induced 25% microscopic positioning error would have each particle's position along the X and Y axes modified by a value randomly generated between -0.5 µm and 0.5 µm. Macroscopic error refers to the subdivision of a crystal structure into multiple crystallites, each with typically unique rotational orientations. To incorporate

30

macroscopic error, the user can define the number of crystallites, the particle array size within each crystallite, the particle spacing of each crystallite and the lattice geometry of each crystallite. The crystallites were then individually generated, given randomly generated orientations, and arranged into a larger crystal structure. Due to the precise control over each crystallite's properties, many different configurations could be tested – such as the presence of mixed hexagonal/2D crystallites commonly seen in experimental samples. The presence of both microscopic and macroscopic error is common in experimentally fabricated samples, making this extensive configurability valuable for emulating experimental scenarios.

Defining Simulation Conditions

In addition to the characteristics of the PhC hydrogel, there are many experimental conditions which could be configured. The observation screen from which the intensity of the diffraction pattern is collected has a controllable dimension and a pixel resolution. The distance of the observation screen from the illuminated PhC hydrogel could be controlled as well as the illumination beam's wavelength and beam diameter.

Calculating Intensity Distribution on Observation Plane

Creating a computational model first requires a clear definition of the simulated experimental environment, including the PhC plane, the observation plane and the notation used to describe the position and angle of scattering vectors. This geometry is described in Figure 2.2.
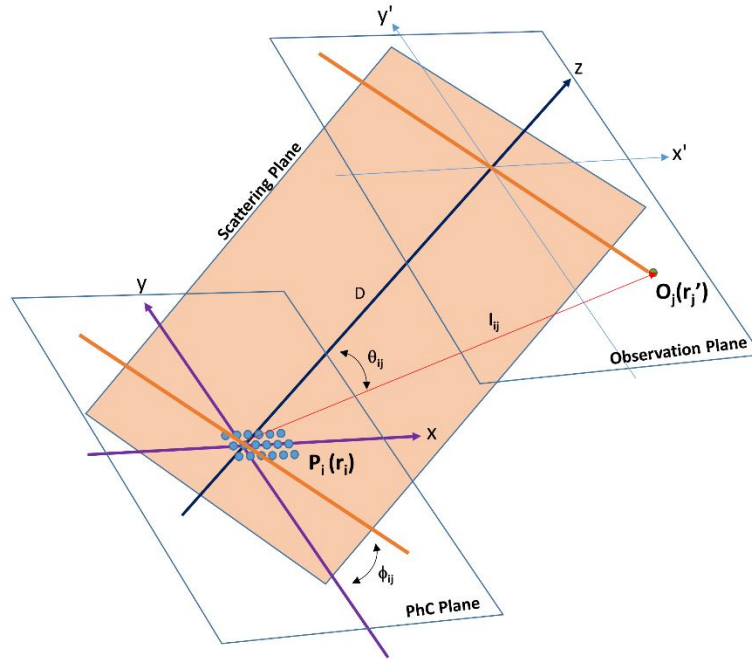
Figure 2.2 Computational Model Geometry. The computational model geometry takes into consideration the plane of the 2D PhC array (x,y,z=0) as well as the parallel observation plane (x',y',Z=D), separated by the distance D. Each particle P_i is located at a distance r_i from the PhC plane origin, where $r_i = \sqrt{x_i^2 + y_i^2}$. The angle ϕ represents the angle of a particle from the PhC plane's y axis while the angle θ_{ij} represents the angle between the particle i, observation plane point j and the illumination axis –referred to as the 'scattering angle'. Finally, the point on the observation plane reached by the scattered photon O_j is located a distance r_j from the observation plane origin, where $r_j = \sqrt{x'^2_j + y'^2_j}$. Additional detail of the computational model's implementation is provided in the mathematical model section.

Mathematical Model

    Measurement of the intensity at each point on the observation screen was a multistep

process which is repeated for each distinct observed location on the screen. First, the

pathlength of each particle to the observation point was calculated. Then, the pathlength,

Mie scattering coefficient and incident electric field were combined to identify the

complex electric field reaching the observation point. Finally, the intensity was

calculated from the electrical field contributions of all particles. A flowchart of this simulation design is provided in Figure 2.3.
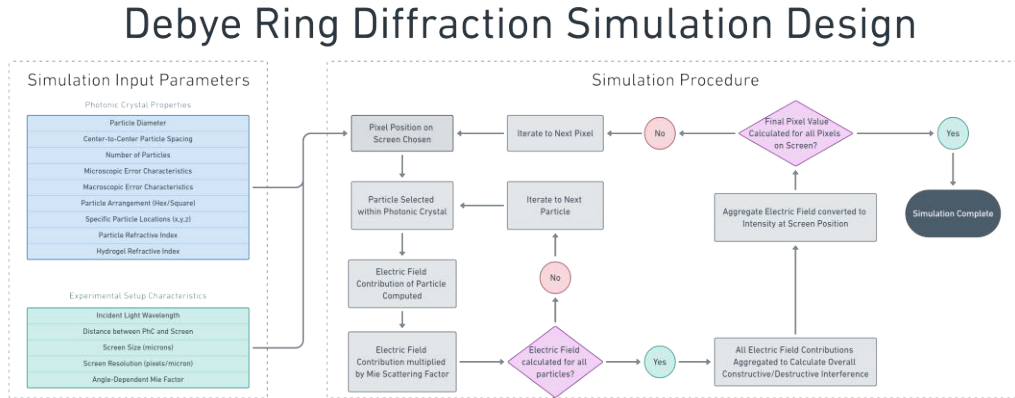
Figure 2.3 Computational Model Design. *The Debye Ring diffraction simulation first requires simulation parameters – the photonic crystal properties and the experimental setup characteristics. A specific sequence of steps is repeated for each pixel on the observation screen to calculate the intensity of the diffraction pattern at that point. The intensity at the observation point is calculated by summing the aggregate electric field contributions from each particle in the photonic crystal. The electric field contribution from a single particle is calculated through consideration of the phase shift based on the pathlength and the angle-dependent Mie factor based on the scattering angle between the particle and the observation plane point.*

In this computational model, three assumptions are made:

(1) The incident light on the PhC is coherent with a uniform intensity

(2) The effective dimension of the PhC is much smaller than the screen distance (D) as well as the screen size.

(3) The medium between the PhC and the screen does not create attenuation

Observation Screen Intensity from Illumination of a 2D Photonic Crystal

For n particles, each particle, *i,* located at position (x_i, y_i) on the PhC plane (x,y,z=0), the pathlength difference (L_{ij}) to a specific observation point O_j located at position (x'_j, y'_j) on the observation plane (x', y', z=D) could be calculated as:

33

$$L_{ij} = \sqrt{(x_i - x_j')^2 + (y_i - y_j')^2 + D^2}$$

The scattering angle between the particle and the observation point could be described as:

$$\theta_{ij} = \sin^{-1}\left(\frac{\sqrt{x_j'^2 + y_j'^2}}{L_{ij}}\right)$$

The electric field contribution of this particle to the observation point, U_{ij} is described by:

$$U_{ij} = E_i e^{i(\phi_i)} * S(\theta_{ij}) * e^{i\,(kL_{ij})}$$

where:

$E_i e^{i(\phi_i)}$ represents the incident electric field

$S(\theta_{ij})$ represents the scattering coefficient

k represents the wavenumber $\frac{2\pi}{\lambda}$

To calculate the entire electric field from all particles, each contribution is summed:

$$U_j = \sum_{i=1}^{n} E_i e^{i(\phi_i)} * S(\theta_{ij}) * e^{i\,(kL_{ij})}$$

Electric field is converted to intensity at the observation screen point O_j by multiplying this term by its complex conjugate:

$$I_j = U_j * U_j^*$$

Scattering Coefficient Calculation

The scattering coefficient is derived using a web-based Mie calculator [113], which provides an angle-dependent normalized scattering coefficient using as input the particle diameter, illumination wavelength, particle refractive index, medium refractive index and particle density. In the developed computational model, it is assumed that incident light is randomly polarized. The normalized factor is derived based on the Mie scattering model as follows:

$$S(\theta_{ij}) = \sqrt{Mie_{natural}(\theta_{ij})}$$

$$Mie_{natural}(\theta_{ij}) = \frac{(|S_1(\theta_{ij})|^2 + |S_2(\theta_{ij})|^2)}{\pi X^2 Q_{sca}}$$

where:

$S_1 \ and \ S_2$: Scattering coefficients derived by Mie theory

X: Particle size parameter

Q_{sca}: Scattering cross-section

Computational Model Evaluation

This computational model was used to carry out numerous simulations to verify alignment with analytical models and compare with an existing simulation, CELES.

Comparison of Computational Model and Analytical Models

The developed computational model was assessed under nine configurations as shown in Table 2.1. These conditions represent the nine possible permutations between the three supported particle configurations (2D array, centered square, hexagonal) and three

different crystal defects states (perfect crystal, microscopic error, macroscopic error). Within each of these conditions nine individual trials which will be run, comparing the computational model and analytical model. The nine trials represent a 2:1, 3:1 and 4:1 ratio of particle distance to particle radius at three unique radii – 0.25, 0.5 and 1 micron. For all trials, the particle array is of size [50x50], the illumination wavelength is 530 nm, the screen distance is 10 mm and the screen size is 40x40 mm – represented by a 251x251 pixel array. The microscopic error defect reflects an error of 10%. The macroscopic error defect reflects a crystal containing 100 crystallites, each composed of 25 particles. The output parameter measured from both the analytical and computational model was the 1st order diffraction diameter. Preliminary statistical analysis compared the analytical results and computational model results using the paired-sample Wilcoxon test. Following this, the specific effect of the independent variables – (1) particle distance to particle radius ratio, (2) the particle radius, (3) the particle configuration and (4) the crystal defect type on the percent difference between the analytical and computational result was assessed. This analysis utilized the independent-sample median, the independent-sample Kruskal-Wallis test and the independent-samples Jonckheere-Terpstra test for ordered alternatives to assess the similarity of medians and distributions across each of the independent variables.

PhC Configurations & Defects per Condition				Trials per Condition		
Condition	Configuration	Crystal Defect		Trial	Particle Radius (um)	Particle Distance (um)
C1	2D Array	None - Perfect Crystal		T1	0.25	0.5
C2	Centered Square	None - Perfect Crystal		T2	0.25	0.75
C3	Hexagonal	None - Perfect Crystal		T3	0.25	1
C4	2D Array	Microscopic Error		T4	0.5	1
C5	Centered Square	Microscopic Error		T5	0.5	1.5
C6	Hexagonal	Microscopic Error		T6	0.5	2
C7	2D Array	Macroscopic Error		T7	1	2
C8	Centered Square	Macroscopic Error		T8	1	3
C9	Hexagonal	Macroscopic Error		T9	1	4

Table 2.1 Comparison of Computational and Analytical Models. The comparison of the computational and analytical models includes 9 unique conditions encompassing all three particle configurations and all three potential defect states – perfect crystal, microscopic error and macroscopic error. Within each condition, nine trials are chosen to assess the suitability of the computational model to assess various particle radii and particle center-to-center distance.

Comparison of Computational Model and CELES

The developed computational model was also compared to an existing multi-particle Mie scattering model in the literature, CELES. As described in Table 2.2, this comparison was performed using only perfect crystals in the 2D and hexagonal configuration. Comparisons were subdivided into three rounds –reflecting a 2:1, 3:1 and 4:1 ratio of particle distance to particle radius. Within each round, the perfect 2D array tested three unique particle radii (0.25, 0.5 and 1 µm) and three unique numbers of particles (1, 4 and 9 particles). The hexagonal array assessment tested the same three particle radii but only assessed 7 particles (a hexagonal unit).

Round 1

Round 1	Particle Radius (um)	Particle Distance (um)	# of Particles (Perfect 2D Array)		Particle Radius (um)	Particle Distance (um)	# of Particles (Perfect Hexagonal Array)
Trial 1	0.25	0.5	1		0.25	0.5	7
Trial 2	0.25	0.5	4		0.5	1	7
Trial 3	0.25	0.5	9		1	2	7
Trial 4	0.5	1	1				
Trial 5	0.5	1	4				
Trial 6	0.5	1	9				
Trial 7	1	2	4				
Trial 8	1	2	4				
Trial 9	1	2	9				

Round 2

Round 2	Particle Radius (um)	Particle Distance (um)	# of Particles (Perfect 2D Array)		Particle Radius (um)	Particle Distance (um)	# of Particles (Perfect Hexagonal Array)
Trial 1	0.25	0.75	1		0.25	0.75	7
Trial 2	0.25	0.75	4		0.5	1.5	7
Trial 3	0.25	0.75	9		1	3	7
Trial 4	0.5	1.5	1				
Trial 5	0.5	1.5	4				
Trial 6	0.5	1.5	9				
Trial 7	1	3	1				
Trial 8	1	3	4				
Trial 9	1	3	9				

Round 3

Round 3	Particle Radius (um)	Particle Distance (um)	# of Particles (Perfect 2D Array)		Particle Radius (um)	Particle Distance (um)	# of Particles (Perfect Hexagonal Array)
Trial 1	0.25	1	1		0.25	1	7
Trial 2	0.25	1	4		0.5	2	7
Trial 3	0.25	1	9		1	4	7
Trial 4	0.5	2	1				
Trial 5	0.5	2	4				
Trial 6	0.5	2	9				
Trial 7	1	4	1				
Trial 8	1	4	4				
Trial 9	1	4	9				

Table 2.2 – Comparison of Computational & CELES Models. This comparison includes 3 unique rounds for 2D array and hexagonal array perfect crystals, each assessing a unique radii to particle spacing ratio across multiple trials. 2D array configurations are tested using 1, 4 and 9 particles while hexagonal configurations are tested using 7 particles. Both configurations test the same three particle radii. 2D array observation planes were generated using a screen distance of 10 mm and a screen size of 40x40 mm. Hexagonal array observation planes were generated using a screen distance of 10 mm and a screen size of 10 mm. In all trials, the screen resolution chosen was [501x501] pixels with an illumination wavelength of 550 nm, a medium refractive index of 1 and a particle refractive index of 1.6.

The output of both CELES and the computational model is a simulated diffraction pattern. The analysis strategy used for comparison is provided in Figure 2.4. Briefly, the extraction of diffraction maxima (peaks) is extracted from each diffraction pattern and the position and intensity of each is recorded. By matching the corresponding peaks in both diffraction patterns, the difference in peak location and difference in peak intensity are collected. Subsequent statistical analysis analyzes the effect of the available independent variables (particle size, particle distance and number of particles (for 2D array)) on the error in peak position and error in peak intensity. Like the previous analysis, this analysis utilized the independent-sample median, the independent-sample Kruskal-Wallis test and the independent-samples Jonckheere-Terpstra test for ordered alternatives to assess the similarity of medians and distributions across each of the independent variables.
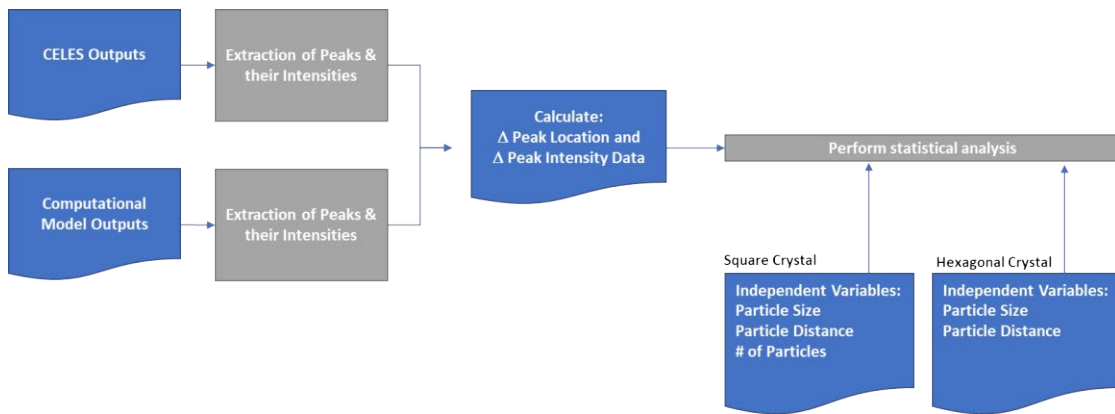
Figure 2.4 Analysis strategy for simulation comparison. The analysis strategy for comparison of CELES and the Computational Model relies on assessment of the diffraction maxima (peaks) and their intensities. The location of the peaks and intensities for both simulations are compared to calculate the error between both models. This error is then statistically analyzed to assess the impact of the available independent variables on that error.

In addition to the monochromatic diffraction simulations, broadband light simulations were also performed to verify that the simulation can capture the opalescent properties of a photonic crystal hydrogel. To accomplish this, the existing computational model is used to first generate a particle array with a defined configuration and spacing characteristic. Next, based on these array characteristics, a Mie factor is generated for every scattering angle in 1-degree increments. This process is also repeated at each incident monochromatic wavelength used in the simulation, since the calculation of the correct Mie factor is both angle-dependent and wavelength-dependent.

Once these steps are complete, the photonic crystal diffraction simulation (either forward or backward diffraction) is carried out 38 times, corresponding to individual monochromatic simulations from 430 to 800 nm in 10 nm increments. Each greyscale image generated is normalized and then thresholded. A lower threshold (average pixel value + 10% of the standard deviation of all pixels) is used which sets all pixels below this value to zero. A higher threshold (maximum pixel value - 10% of the standard deviation of all pixels) is used which sets all pixels above this value to 1. These thresholds were experimentally identified to remove background noise while segregating the constructive interference peaks. This thresholding procedure is repeated for the diffraction pattern generated by each monochromatic illumination.

After individual images are thresholded, they are all combined into one composite stack, of size (x, y, λ). Each (x, y) pixel is then compared across the λ dimension in order to identify the 'dominant' color which should appear at that screen position. The dominant color at that pixel is written to an RGB image of size $(x, y, 3)$. If all pixels

across the λ dimension have a value of 0, this implies that this screen (x,y) location fell

below the lower threshold in each diffraction pattern corresponding to every illumination

wavelength. As a result, this specific pixel location in the final image is written as black

(RGB: 0,0,0). Similarly, if all pixels across the λ dimension have a value of 1, this

implies that this screen (x,y) location fell above the upper threshold in each diffraction

pattern (commonly occurring at the center of the screen). Subsequently, the specific

pixel in the final image is written as white (RGB: 255, 255, 255).

For all other pixel locations, the dominant wavelength is identified based on the

monochromatic diffraction pattern which generated the highest greyscale value at that

(x,y) position. This wavelength is then converted to an RGB image using a color-

matching function, specifically the CIE 1964 style. Since color to wavelength matching

varies intrinsically based on individual biology and the angle by which the light enters the

eye, conversion of monochromatic light to an RGB value is an imperfect estimate.

Results

Computational Model Diffraction Patterns

To verify that the computational model provided diffraction patterns which

matched theoretical expectations, each of the various model inputs were investigated.

Figure 2.5 provides representative images of the diffraction pattern resulting from each

particle configuration.
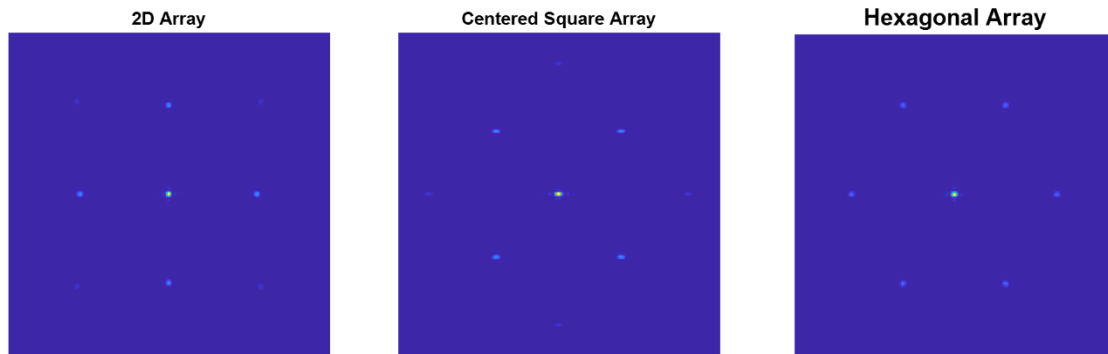
Figure 2.5 Perfect Crystal Diffraction Pattern. Representative image of the diffraction pattern generated by a perfect crystal structure under different configurations. A [251x251] pixel screen was generated representing a [10x10] mm screen located at a distance of 10 mm from the PhC hydrogel. The PhC hydrogel was composed of 400 particles with 2 micron particle spacing and a 0.5 micron particle diameter in a perfect crystal with either a 2D array, centered square array or hexagonal array configuration. A simulated 530 nm light source illuminated the PhC hydrogel.

A focus only on perfect crystalline structures is not realistic since experimental photonic crystals typically include a combination of microscopic and macroscopic error. Microscopic error is characterized by small defects of the individual particle positions within a crystal structure. Macroscopic error is characterized by the presence of smaller crystallites within a polycrystal which combine to create a macroscopic structure. The debye ring commonly referred to experimentally exists because of macroscopic error, since each crystallite has a unique orientation, resulting in the superposition of a 'perfect' diffraction pattern at many rotational angles - a circular final pattern. A typical experimental photonic crystal will have a combination of both microscopic and macroscopic error. As shown in Figure 2.6, microscopic error does not change the diffraction pattern dimensions significantly since the average particle spacing is retained. Macroscopic error results in a characteristic debye ring.
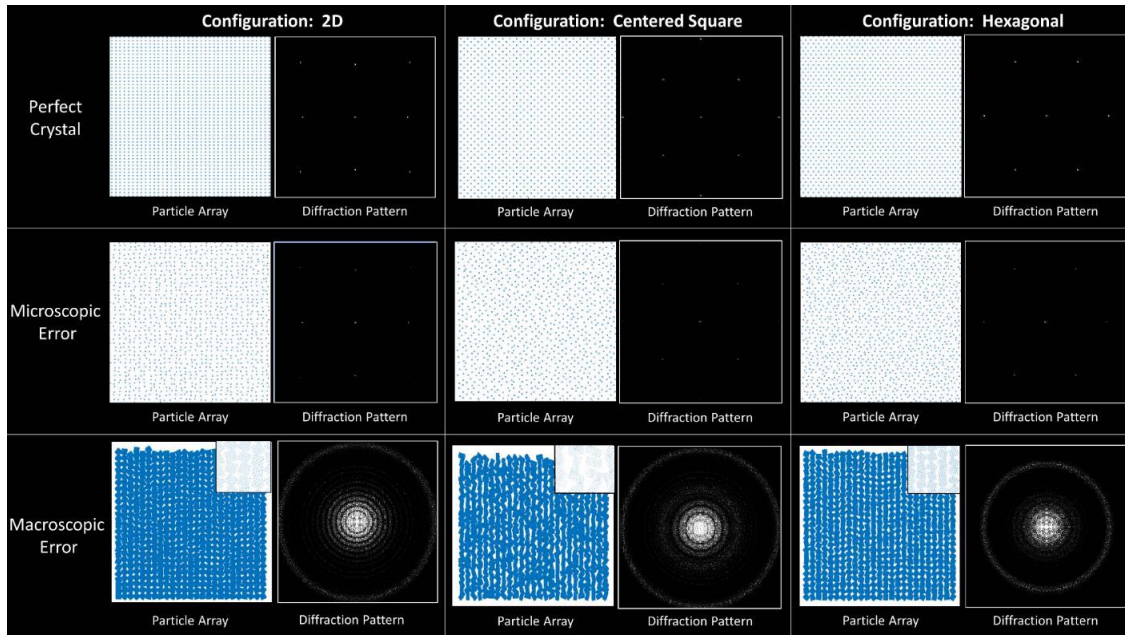
Figure 2.6 Simulation of Microscopic and Macroscopic Error. Crystal structures are experimentally corrupted with both microscopic as well as macroscopic error. Microscopic error is simulated here as randomly applied ±25% error (±0.5 µm) of a perfect crystal structure, and results in a weaker higher-order diffraction peak. Macroscopic error is simulated as a collection of randomly oriented crystallites within a larger crystal structure, generating the characteristic Debye Ring seen experimentally. The macroscopic error is generated using a 25 x 25 crystallite array, each containing a 10 x 10 particle configuration. The inset image provides a zoomed view of the crystallite structure. The following simulation conditions were used: Particle Spacing (2 µm), Wavelength (530 nm), Screen Distance (12 cm), Screen Size ([10 x 10 cm], [500 x 500 pixels])).

While the previous figure highlights distinct types of error for specific particle configurations, an experimental photonic crystal will typically have macroscopic error characterized by crystallites which have both 2D as well as hexagonal configurations. This characteristic is depicted in Figure 2.7, which considers various densities of both configurations within a larger crystal. When only macroscopic error is present, each configuration generates a unique debye ring, with the hexagonal pattern generating a smaller diameter than the 2D pattern. Intensity of the ring is proportional to circumference, as the 50%/50% configuration appears to have the smaller ring be brighter

since the same intensity is distributed over a smaller area. This phenomenon also describes why the 25% Hex, 75% 2D combination has approximately equivalent intensities, since the outer ring while having a larger intensity contribution is distributed over a larger circumference. When microscopic error is added, the two distinct rings combine into a more diffuse ring.
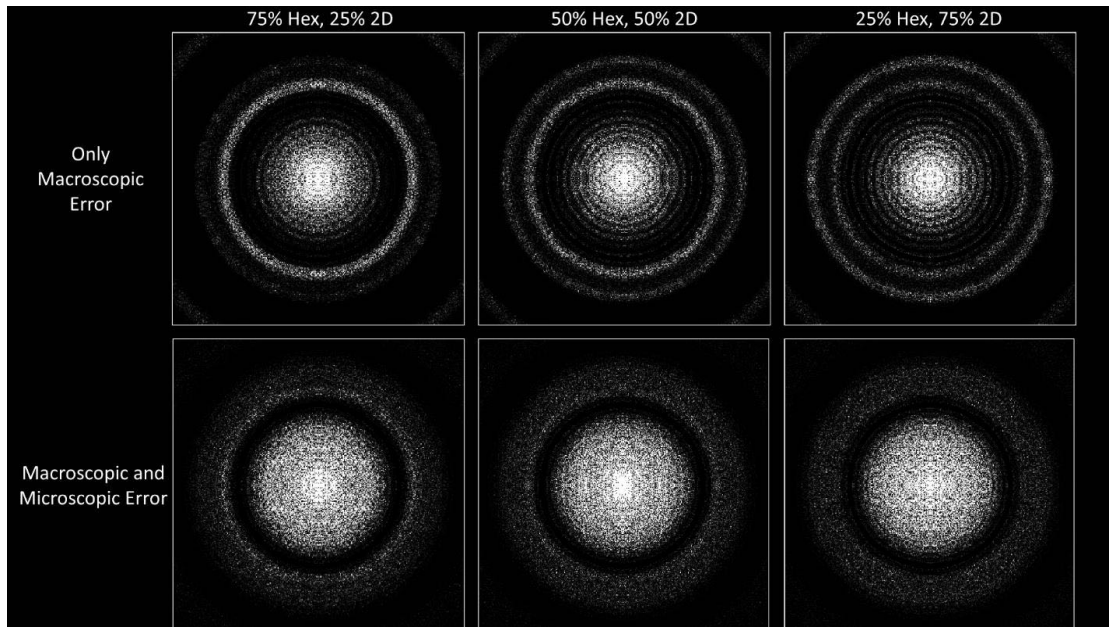
Figure 2.7 Simulation of Mixed-Configuration Macroscopic Error. Fabricated photonic crystals commonly have both macroscopic and microscopic error, as well as a mixture of both hexagonal and 2D configuration crystallites. The developed photonic crystal simulator allows for characterization of all of these cases. When microscopic error is not present, each set of crystallites generates a unique debye ring, with intensity proportional to the quantity of each. The presence of microscopic error creates the characteristic 'thickening' of the Debye ring, which encompasses both individual rings created if microscopic error was not present. The following simulation conditions were used: 625 crystallites, each [10x10] particles, Particle Spacing (2 μm), Wavelength (530 nm), Screen Distance (12 cm), Screen Size ([12 x 12 cm], [400 x 400 pixels]), ±0.5 μm microscopic error.

Computational Model vs Analytical Models

The proposed computational model was compared to the existing analytical models to confirm its accuracy. Trial 1 was excluded from analysis since the analytical equations cannot be evaluated when the particle spacing is below the illumination

wavelength – a limitation that does not apply to the computational model. As demonstrated in Figure 2.8, the difference between the two models was not significantly different for any of the nine scenarios tested based on the outcomes of a nonparametric paired sample Wilcoxon test. A closer inspection reveals that while the two approaches provide very similar results, there is a noticeable difference due to either too small of a 1st order diffraction diameter to be well reproduced by the computational model (trial 8 and trial 9 of each configuration) or due to the presence of macroscopic error, which complicates the precise measurement of 1st order diffraction diameter.
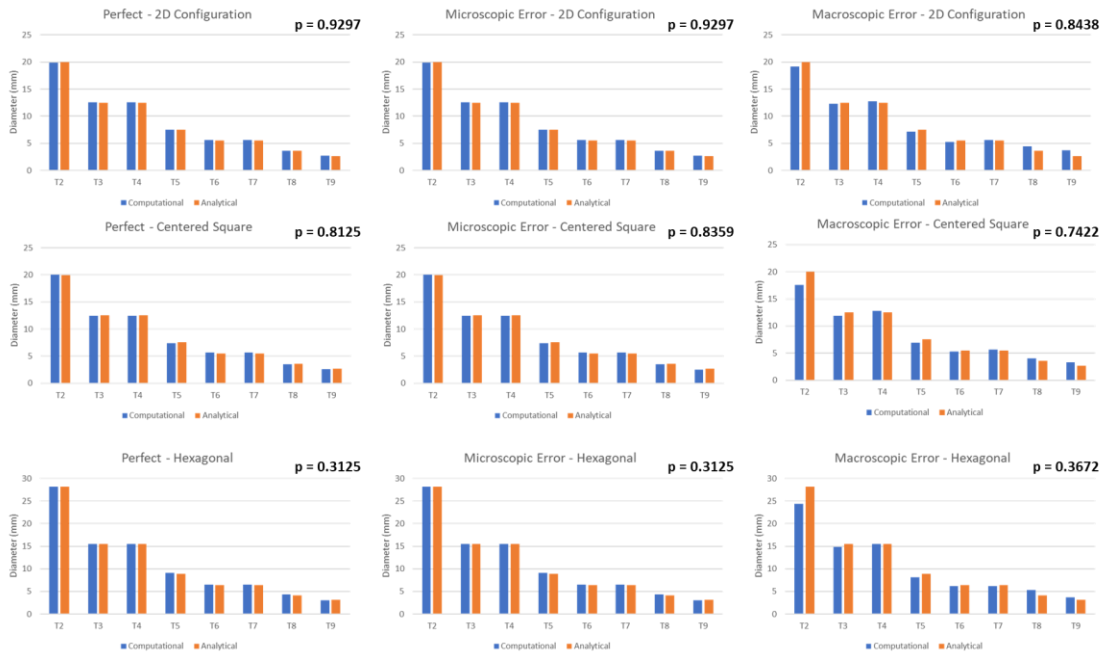
Figure 2.8 Comparison of Analytical and Computational Model Outcomes. Comparison of analytical and computational model for each condition and trial. The p value in the top-right corner of each figure represents the outcome of a nonparametric paired sample Wilcoxon test which assessed if a statistically significant difference existed between the two methods for each configuration. No significant difference was found for any configuration.

Additional statistical analysis was performed to assess if the percent difference between the computational model and analytical equations could be significantly explained by the various independent variables present in the experimental design – (1) the particle spacing: radius ratio, (2) the particle radius, (3) the particle configuration and (4) the crystal defect type. As demonstrated in Table 2.3, no significant effects were found except for the effect of particle radius, which was found to have a significant impact on both the median and distribution of the percent difference between computational model and analytical model.

Independent Variable: Particle Spacing : Radius Ratio

Hypothesis	Test Used	Significance
The medians of **CM:Analytical % Difference** are the same across **D/R Ratio** Categories.	Independent-Samples Median Test	0.395
The distribution of **CM:Analytical % Difference** is the same across **D/R Ratio** Categories	Independent-Samples Kruskal-Wallis Test	0.921
The distribution of **CM:Analytical % Difference** is the same across **D/R Ratio** Categories	Independent-Samples Jonckheere-Terpstra Test for Ordered Alternatives	0.767

Independent Variable: Particle Radius

Hypothesis	Test Used	Significance
The medians of **CM:Analytical % Difference** are the same across **Radius** Categories.	Independent-Samples Median Test	0.011
The distribution of **CM:Analytical % Difference** is the same across **Radius** Categories	Independent-Samples Kruskal-Wallis Test	Less than 0.001
The distribution of **CM:Analytical % Difference** is the same across **Radius** Categories	Independent-Samples Jonckheere-Terpstra Test for Ordered Alternatives	0.004

Independent Variable: Particle Configuration

Hypothesis	Test Used	Significance
The medians of **CM:Analytical % Difference** are the same across **Configuration** Categories.	Independent-Samples Median Test	0.946
The distribution of **CM:Analytical % Difference** is the same across **Configuration** Categories	Independent-Samples Kruskal-Wallis Test	0.590
The distribution of **CM:Analytical % Difference** is the same across **Configuration** Categories	Independent-Samples Jonckheere-Terpstra Test for Ordered Alternatives	0.352

Independent Variable: Crystal Defect Type

Hypothesis	Test Used	Significance
The medians of **CM:Analytical % Difference** are the same across **Defect** Categories.	Independent-Samples Median Test	0.485
The distribution of **CM:Analytical % Difference** is the same across **Defect** Categories	Independent-Samples Kruskal-Wallis Test	0.290
The distribution of **CM:Analytical % Difference** is the same across **Defect** Categories	Independent-Samples Jonckheere-Terpstra Test for Ordered Alternatives	0.869

Table 2.3 Statistical Analysis of Computational and Analytical Model Outcomes. Statistical analysis of the impact of each independent variable on the percent difference between the computational model and analytical model 1st order diffraction diameter. The only significant factor identified was the impact caused by the particle radius, which affects both the median and distribution.

To better understand the impact of each of these independent variables, Figure 2.9 highlights the distribution of the percent difference between the computational and analytical model for each level of each categorical independent variable. Additionally, a

histogram of all of the values is provided. The individual boxplots reveal that the most

significant drivers of error between the models is the 1 μm particle radius (since it

represents the conditions with the smallest debye ring diameter) and the presence of

macroscopic error. Assessment of these results also reveals that the perfect crystal

provides the most aligned results, followed by microscopic error and then macroscopic

error.
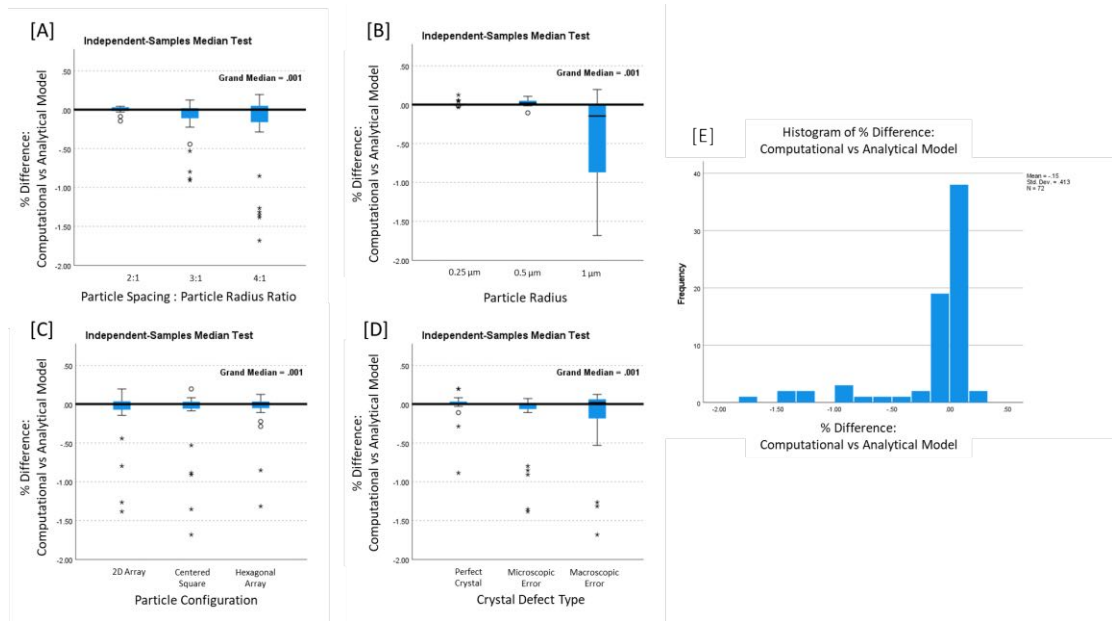
Figure 2.9 Visualization of Analytical and Computational Model Outcomes. Visualizations are provided for the distribution of the percent error between the models based on each of the independent variables – particle spacing : [A] particle radius ratio, [B] particle radius, [C] particle configuration, and [D] crystal defect type. Additionally, a histogram of all of the percent error values is provided [E].

Computational Model vs CELES

The comparison of the computational model and CELES relied on a quantitative

analysis of the resulting diffraction pattern – specifically the location and intensity of

each diffraction maxima (peak). Representative images of a 2D array and hexagonal

array diffraction pattern and the resulting horizontal and vertical profiles are provided in

Figure 2.10. The line profiles demonstrate similar, but imperfect matches for both

intensity and peak position.
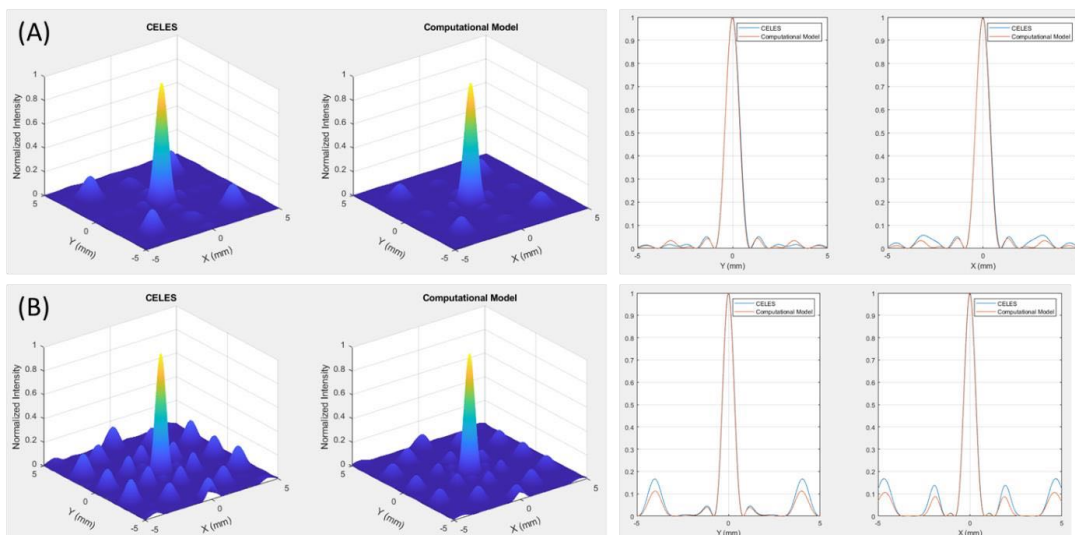
Figure 2.10 Representative Examples of Computational Model / CELES Comparison. Visualizations are provided for the intensity distribution of the diffraction pattern for a 2D array [A] and hexagonal array [B] crystal for both CELES and the Computational Model. The 2D array diffraction pattern (Round 1, Trial 9) was generated using 9 particles, each 1 µm in radius and spaced 2 µm apart. The Hexagonal array diffraction pattern (Round 2, Trial 3) was generated using 7 particles, each 1 µm in radius and spaced 3 µm apart.

Prior to statistical analysis, descriptive statistics were generated to assess the

distribution of the peak positional error and peak intensity error across all the peaks

present in all trials, provided below. Figure 2.11 demonstrates that intensity error is

typically below 10% while positional error is typically below 10 pixels (approximately

790 µm).
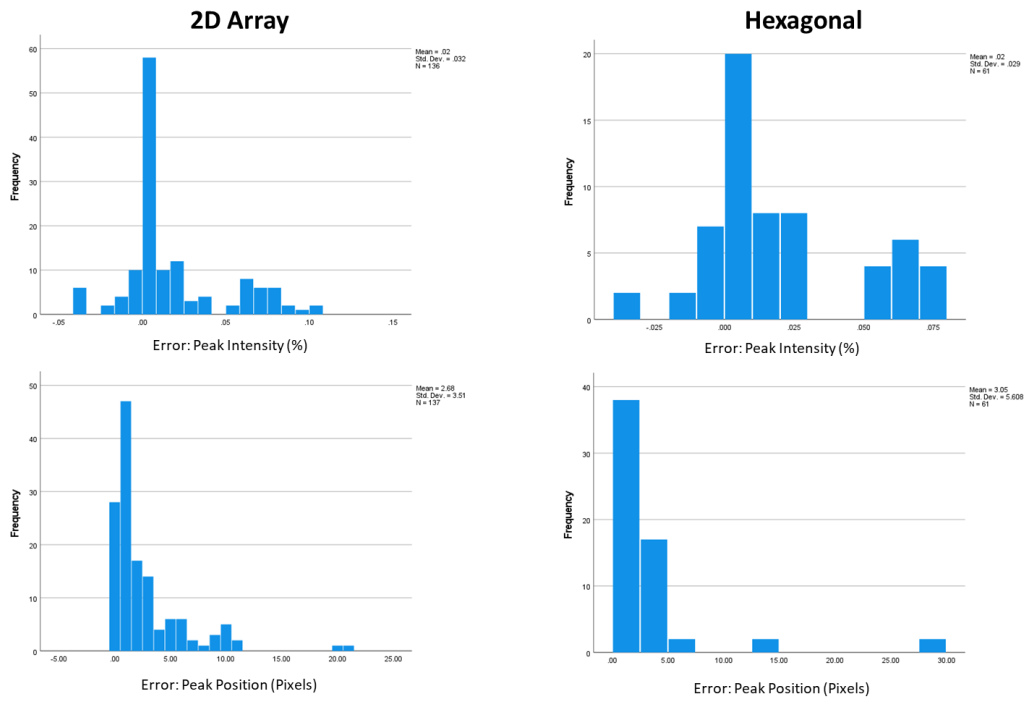
Figure 2.11 Descriptive Statistics of Error. Distributions of intensity and position error across all trials are provided for both the 2D array and hexagonal array configuration.

Statistical Analysis: 2D Array

Analysis of the effects of the particle spacing to radius ratio on peak intensity error and peak location error of the 2D array configuration is provided in Figure 2.12. The '1 particle' scenario for 2D array was excluded since it does not generate additional diffraction peaks beyond the 0th order diffraction. These results demonstrate that the

particle spacing to radius ratio does not significantly impact the peak intensity error, but significantly affects the peak position error.

Hypothesis	Test Used	Significance
The medians of **ΔPeak Intensity** are the same across **D/R Ratio** Categories.	Independent-Samples Median Test	0.359
The distribution of **ΔPeak Intensity** is the same across **D/R Ratio** Categories	Independent-Samples Kruskal-Wallis Test	0.519
The distribution of **ΔPeak Intensity** is the same across **D/R Ratio** Categories	Independent-Samples Jonckheere-Terpstra Test for Ordered Alternatives	0.250
The medians of **ΔPeak Position** are the same across **D/R Ratio** Categories	Independent-Samples Median Test	Less than 0.001
The distribution of **ΔPeak Position** is the same across **D/R Ratio** Categories	Independent-Samples Kruskal-Wallis Test	Less than 0.001
The distribution of **ΔPeak Position** is the same across **D/R Ratio** Categories	Independent-Samples Jonckheere-Terpstra Test for Ordered Alternatives	Less than 0.001
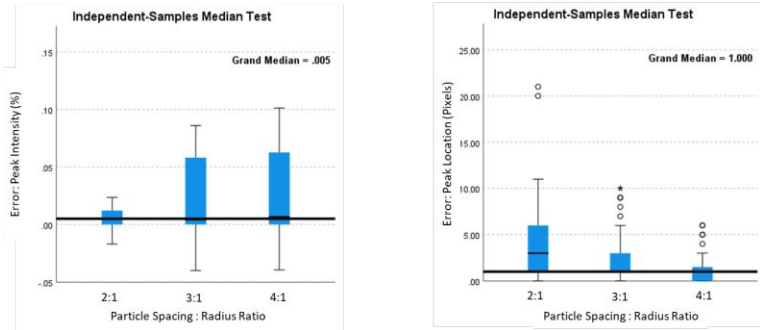
Figure 2.12 Impact of Particle Spacing : Radius on CELES Comparison for 2D Array. Analysis of the impact of particle spacing: particle radius ratio on peak intensity error and peak position error for the 2D array configuration.

Analysis of the effects of the quantity of particles on peak intensity error and peak location error of the 2D array configuration is provided in Figure 2.13. These results demonstrate that the number of particles does not significantly affect intensity error but does significantly impact positional error.

Hypothesis	Test Used	Significance
The medians of **ΔPeak Intensity** are the same across **Particle Count** Categories.	Independent-Samples Median Test	0.153
The distribution of **ΔPeak Intensity** is the same across **Particle Count** Categories	Independent-Samples Kruskal-Wallis Test	0.130
The distribution of **ΔPeak Intensity** is the same across **Particle Count** Categories	Independent-Samples Jonckheere-Terpstra Test for Ordered Alternatives	0.130
The medians of **ΔPeak Position** are the same across **Particle Count** Categories	Independent-Samples Median Test	0.009
The distribution of **ΔPeak Position** is the same across **Particle Count** Categories	Independent-Samples Kruskal-Wallis Test	Less than 0.001
The distribution of **ΔPeak Position** is the same across **Particle Count** Categories	Independent-Samples Jonckheere-Terpstra Test for Ordered Alternatives	Less than 0.001
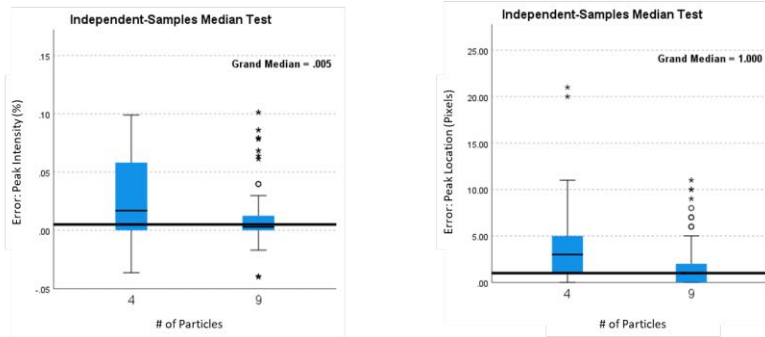
Figure 2.13 Impact of Number of Particles on CELES Comparison for 2D Array. Analysis of the impact of the number of particles on peak intensity error and peak position error for the 2D array configuration.

Analysis of the effects of the particle radius on peak intensity error and peak location error of the 2D array configuration is provided in Figure 2.14. These results demonstrate that particle radius affects both intensity and positional error.

Hypothesis	Test Used	Significance
The medians of **ΔPeak Intensity** are the same across **Particle Radius** Categories.	Independent-Samples Median Test	Less than 0.001
The distribution of **ΔPeak Intensity** is the same across **Particle Radius** Categories	Independent-Samples Kruskal-Wallis Test	Less than 0.001
The distribution of **ΔPeak Intensity** is the same across **Particle Radius** Categories	Independent-Samples Jonckheere-Terpstra Test for Ordered Alternatives	Less than 0.001
The medians of **ΔPeak Position** are the same across **Particle Radius** Categories	Independent-Samples Median Test	0.001
The distribution of **ΔPeak Position** is the same across **Particle Radius** Categories	Independent-Samples Kruskal-Wallis Test	0.002
The distribution of **ΔPeak Position** is the same across **Particle Radius** Categories	Independent-Samples Jonckheere-Terpstra Test for Ordered Alternatives	0.073
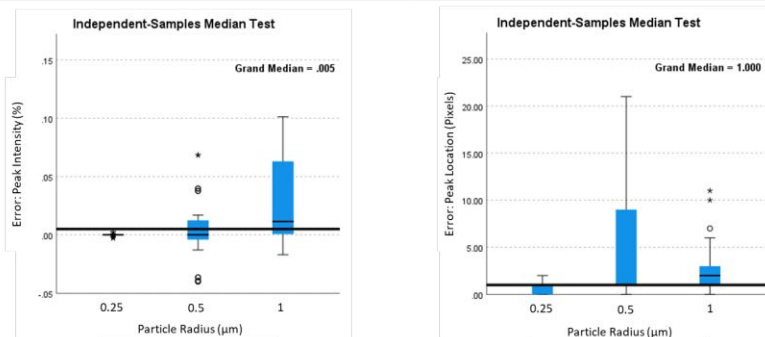
Figure 2.14 Impact of Particle Radius on CELES Comparison for 2D Array. Analysis of the impact of the particle radius on peak intensity error and peak position error for the 2D array configuration.

51

Statistical Analysis: Hexagonal Array

Analysis of the effects of the particle spacing to radius ratio on peak intensity error and peak location error of the hexagonal array configuration is provided in Figure 2.15. These results demonstrate that the spacing to radius ratio for hexagonal particles contributes to intensity error, but for positional error only the distribution but not the median value.

Hypothesis	Test Used	Significance
The medians of ΔPeak Intensity are the same across D/R Ratio Categories.	Independent-Samples Median Test	Less than 0.001
The distribution of ΔPeak Intensity is the same across D/R Ratio Categories	Independent-Samples Kruskal-Wallis Test	Less than 0.001
The distribution of ΔPeak Intensity is the same across D/R Ratio Categories	Independent-Samples Jonckheere-Terpstra Test for Ordered Alternatives	0.003
The medians of ΔPeak Position are the same across D/R Ratio Categories	Independent-Samples Median Test	0.144
The distribution of ΔPeak Position is the same across D/R Ratio Categories	Independent-Samples Kruskal-Wallis Test	0.005
The distribution of ΔPeak Position is the same across D/R Ratio Categories	Independent-Samples Jonckheere-Terpstra Test for Ordered Alternatives	0.069
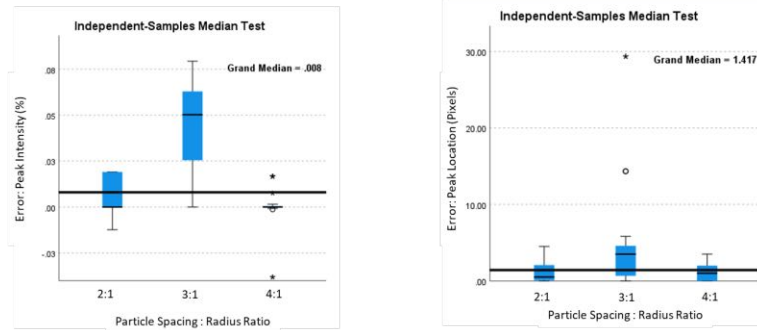
Figure 2.15 Impact of Particle Spacing : Radius on CELES Comparison for Hex Array. Analysis of the impact of the particle spacing : particle radius ratio on peak intensity error and peak position error for the hexagonal array configuration.

Analysis of the effects of the particle radius on peak intensity error and peak location error of the hexagonal array configuration is provided in Figure 2.16. These results suggest that neither peak intensity nor peak position error are significantly impacted by particle radius.

Hypothesis	Test Used	Significance
The medians of ΔPeak Intensity are the same across Particle Radius Categories.	Independent-Samples Median Test	0.157
The distribution of ΔPeak Intensity is the same across Particle Radius Categories	Independent-Samples Kruskal-Wallis Test	0.217
The distribution of ΔPeak Intensity is the same across Particle Radius Categories	Independent-Samples Jonckheere-Terpstra Test for Ordered Alternatives	0.103
The medians of ΔPeak Position are the same across Particle Radius Categories	Independent-Samples Median Test	0.157
The distribution of ΔPeak Position is the same across Particle Radius Categories	Independent-Samples Kruskal-Wallis Test	0.281
The distribution of ΔPeak Position is the same across Particle Radius Categories	Independent-Samples Jonckheere-Terpstra Test for Ordered Alternatives	0.987
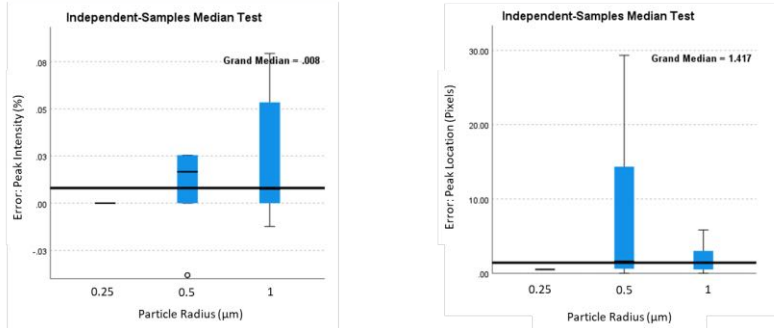
Figure 2.16 Impact of Particle Radius on CELES Comparison for Hex Array. Analysis of the impact of the particle radius on peak intensity error and peak position error for the hexagonal array configuration.

Broadband Illumination Simulation

All previous simulations have focused on monochromatic illumination. Due to the reflection-mode detection methodology for photonic crystals, it has been well described that diffraction peaks occur at unique angles for various input wavelengths. This same phenomenon was captured using transmission-mode simulations in Figure 2.17. A collection of 37 distinct wavelengths distributed between 430 and 800 nm were used to generate individual diffraction patterns. The maximum intensity for each pixel across all diffraction patterns was used to assign the pixel an RGB value based on color-matching functions relating the wavelength to a particular RGB value. Before thresholding, this causes each pixel to be assigned a unique color, even if it represents background across all illumination wavelengths. Utilizing a thresholding routing prior to combining diffraction patterns, the effect of broadband illumination for different configurations and types of errors could be simulated.
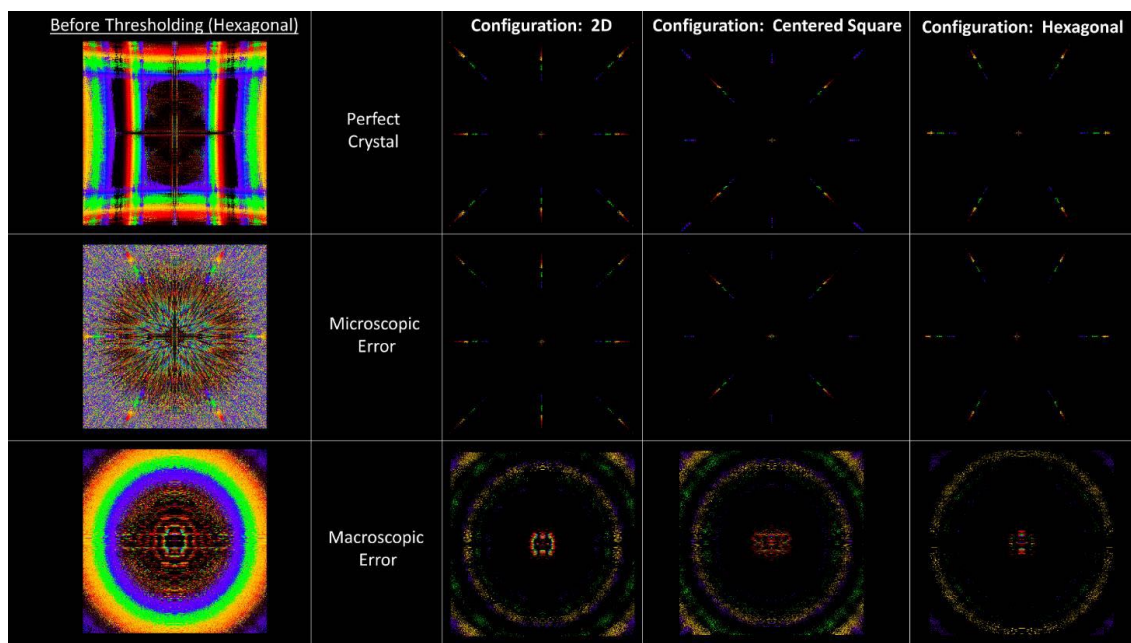
Figure 2.17 Broadband Illumination Simulation. The simulation could also be extended to consider broadband illumination through the creation of a unique observation screen for each discrete wavelength – 430 nm to 800 nm in 10 nm increments. The color assigned to a specific pixel is then chosen based on the highest intensity across each of the generated observation screens. Without thresholding, this would allow very low-intensity pixels to fill the observation screen. After incorporating a thresholding approach, the resulting images properly reject low-intensity values.

Discussion & Conclusion

Novelty & Impact

The proposed computational model plays an important role to enhance Debye ring theoretical models. The theoretical Debye ring model is a rapid and simple analytical equation, but it is only valid for perfect hexagonal or 2D particle arrangements in a 2-dimensional structure. Multiparticle Mie scattering model provide accuracy in arbitrary arrangement and are polarization sensitive, but typically require a uniform particle structures and substantial computational resources to model a relatively small number of particles. The proposed computational model has the flexibility of allowing irregular organization of large numbers of particles with low computational resource requirements.

54

Furthermore, it can provide diffraction patterns for both transmission and reflection. Through the numerous verification tests performed in this specific aim, the validity of the computational model has been demonstrated.

Model Performance Evaluation

Although existing theoretical equations for Debye ring formation are only valid for perfect crystals, they are still useful for validating the computational model. Only two theoretical equations exist, one to describe the scattering angle θ for a 2D / centered square array ($\theta = sin^{-1}(\frac{\lambda}{d})$) and one to describe the scattering angle for a hexagonal array ($\theta = sin^{-1}(\frac{2\lambda}{\sqrt{3}d})$), where λ is the wavelength of light and d is the average particle spacing. Comparisons of the theoretical and simulated diffraction pattern size while varying the particle configuration, particle spacing, illumination wavelength and screen distance all demonstrated a clear alignment between the two sets of results, validating the ability of the computational model to align with theory under its limited use cases. Furthermore, the concept of diffraction pattern generation in the transmission axis as well as in the reverse direction via reflection is supported in the literature[24].

Alignment of Experimental & Simulated Results

To provide clear evidence of the accuracy of the diffraction pattern resulting from the computational model, it is necessary to compare its output to other published literature. Fortunately, an article in the scientific literature exists which presented sufficient parameters to serve as model inputs that could generate a diffraction pattern. This article illuminated a hexagonal photonic crystal with nearest-neighbor particle spacing of 1.26 μm with a 532 nm monochromatic light source onto an observation

screen 13.4 cm from the crystal [71]. The article described a resulting diffraction ring diameter of 15.0 cm. These parameters served as inputs to the computational model developed to simulate the diffraction pattern on a screen with a 0.02 cm/pixel resolution. The simulated diffraction pattern had a diameter of 15.02 cm, generating error of only 0.13% from the literature value.

Comparison of Perfect Crystal and Polycrystal Structure

The computational model demonstrates that a perfect crystal structure generates a series of distinct, uniformly spaced diffraction peaks while the presence of microscopic and macroscopic error creates the characteristic debye ring. Experimentally, the difference between these two scenarios could occur simply due to the spot size of the laser. A perfect crystal structure can be present over a small area of a photonic crystal (e.g. within a crystallite) but if the observation area is expanded then the presence of microscopic and macroscopic error becomes far more likely. This observation is directly supported by the scientific literature, which identified that illumination of a hexagonally-configured photonic crystal with a 0.25 mm spot size generated six symmetrical spots identical to the computational model result for a perfect crystal [26]. When the spot size was expanded to 4 mm, a debye ring pattern was seen instead. These results support the computational model in both the diffraction pattern of a perfect hexagonal structure as well as the effect of a polycrystal. Additional research into the diffraction pattern formed by perfect crystals has also found that a square particle array generates a diffraction pattern which matches the computational model [114].

Independence of Microscopic Error from Diffraction Pattern Diameter

According to the theoretical equations predicting debye ring diameter, the average particle spacing plays a critical role in the resulting diffraction pattern. Based on this, it can be assumed that error applied to the individual particle positions which doesn't impact the average spacing would not have significant effect on the resulting diffraction pattern dimensions. This was clearly demonstrated in the outcomes of the computational model where randomly generated positional error was applied within a specific range which did not change the size of the resulting diffraction pattern, providing additional verification of the computational model's accuracy.

Impact of Macroscopic and Microscopic Error on Debye Ring Diffraction Pattern

The proposed computational model demonstrated unique diffraction patterns resulting from perfect crystals, macroscopic error, and a combination of microscopic and macroscopic error. These results are corroborated by an experiment in the scientific literature which used sodium chloride to induce defects in photonic crystal formulation and assessed the impact on the resulting diffraction pattern [21]. The authors found that a near-perfect hexagonal structure generated a diffraction pattern of six equally spaced bright points concentrically oriented around the transmission axis. When a low salt concentration was induced during self-assembly, the photonic crystal acquired macroscopic, but not microscopic error. The resulting diffraction pattern, a debye ring, further supports the computational model. Finally, the authors used a high salt concentration to induce both microscopic and macroscopic error. This resulted in a diffused debye ring, matching the simulated results.

<u>Wavelength-dependent Diffraction Angle</u>

A well understood phenomena associated with photonic crystals is the wavelength-dependent diffraction angle [115], providing the opalescent qualities of this material. This aspect of the material was successfully validated through the broadband diffraction simulation, which demonstrated a unique diffraction angle for wavelengths distributed across the visible spectra. This phenomenon was also validated through the separate assessment of the effect of different input monochromatic wavelengths.

<u>Computational Model Evaluation</u>

For each comparison an independent-samples median test was used along with two measures of distribution - the kruskal-wallis test and Jonckheere-Terpstra test for ordered alternatives. The kruskal wallis test functions as a non-parameteric one way anova for comparing each of the various levels of the independent variables tested while the Jonckheere-Terpstra test for ordered alternatives is a rank-based test which is specialized for identifying trends in data when categorical independent variables fall within a sequence.

Comparison of the computational model and the existing analytical equations clearly demonstrated that the computational model provides a high-quality reproduction of the analytical expectations for all three configurations and for all crystal defect states. An advantage of the computational model over the analytical model is its ability to predict diffraction order diameter when the particle spacing is below the light wavelength - a scenario that the analytical model cannot provide a solution for. A disadvantage of the computational model is its challenge in calculating diffraction order diameter when the diameter is very small and nearly aligned with the transmission axis. Statistical

comparison of the two models' outcomes using all available independent variables demonstrated that smaller debye ring diameters and the presence of macroscopic error are the largest contributors of error between the two models.

Comparison of the computational model and CELES required a unique strategy since the unique peaks of each required extraction and comparison. The previous analysis already demonstrated the value of the computational model's positional accuracy, but the CELES model is understood to more likely provide accurate intensity distributions due to its use of the multi-particle Mie scattering model. Assessment of the distribution of intensity error and positional error of the diffraction maxima revealed that the models provided very similar outcomes - with peak intensity error within 10% of one another and positional error below 800 microns.

Assessment of the 2D array trials revealed that particle count and the spacing:radius ratio did not significantly impact intensity error but impacted positional error. Position error was driven by lower spacing:radius ratio and lower particle counts. The impact of lower particle counts is likely due to the more diffused diffraction peaks which occur at these lower particle counts. Particle radius significantly impacted both positional and particle error, with larger sizes generating additional error. According to its authors, CELES is designed to be used with smaller particles, which may cause these results. Particle spacing to radii ratio did not create a significant effect on positional error as measured by the Jonckheere-Terpstra test but was significant as measured by Kruskal-Wallis, suggesting that a significant difference exists but it is not a 'trend' significance which is based on a steadily increasing or decreasing pattern from 0.25 to 0.5 to 1 micron.

Assessment of the hexagonal array trials revealed that the particle spacing to radius ratio significantly impacted peak intensity but to a lesser extent peak position. Particle spacing to radii ratio did not create a significant effect on positional error as measured by the Jonckheere-Terpstra test but was significant as measured by Kruskal-Wallis, suggesting that a significant difference exists but it is not a 'trend' significance which is based on a steadily increasing or decreasing pattern from 2:1 to 3:1 to 4:1. Particle radii did not have a significant effect on either peak intensity error or peak position error.

Limitations and Future Work

While the proposed computational model has many powerful capabilities, it does have intrinsic limitations. First, it is polarization insensitive, preventing its use for simulating platforms where this information is required. Second, it cannot provide accurate intensity measurements since it relies on a single particle Mie scattering model for angular distribution calculations. Despite these limitations, this computational model provides a flexible, lightweight platform for PhC diffraction simulation which serves the broader scientific community by providing a tool to aid PhC sensor design. Unlike tools such as CELES, this computational model does not require a high-powered CUDA-compatible graphics card or large amounts of RAM. Future improvements to the model can include incorporating polarization state, allowing for non-perpendicular incident light trajectories to the PhC plane and parallelization of the underlying mathematics using parallel processing on the CPU or graphics card.

Chapter 3: Fabrication of PhC Hydrogel

Introduction

<u>PhC Hydrogel Fabrication Methods</u>

Many methodologies for traditional PhC hydrogel fabrication have been described in Chapter 1. In this chapter, a novel approach will be implemented where fluorescent markers are incorporated during PhC hydrogel fabrication to help facilitate the extraction of particle positional information to support validation of the computational model described in the previous chapter.

The incorporation of fluorescent markers within fabrication of PhC hydrogels has been used in the scientific literature for functionalization and sensing of analytes. These markers are typically attached to the hydrogel matrices instead of the particles themselves. One group functionalized the hydrogel component of a PhC to be fluorescent using polyethylenimine-capped CdS quantum dots and found that the ability of nitrite to significantly quench fluorescence activity made the platform a valuable sensor for nitrite [116]. An alternative fluorescent functionalization approach utilized Cadmium Telluride crystals embedded within the hydrogel structure of a PhC to generate photonic crystal supraballs (macroscopic spherical PhC hydrogel structures) which could be monitored via fluorescence microscopy [117]. A separate group attempting to enhance fluorescence enhancements of PhC hydrogels utilized an infiltration strategy via soaking an inverse opal photonic crystal with Fluor 488 dye [118]. The inverse opal photonic crystal generates a local resonance mode which enhances Fluor 488 emission 7.7-fold, making it a valuable platform for biological fluorescence sensing. None of

these approaches provide fluorescent labels to the actual particles, as they simply functionalize the surrounding hydrogel matrix.

Limited examples of use of fluorescent particles to fabricate PhC hydrogels can be found in the scientific literature compared to the use of fluorescent hydrogels in PhCs. One research team utilized scattered fluorescent silica particles embedded within a much larger group of non-fluorescent particles to generate 3D PhC structures[119]. Fluorescent imaging of the structure allowed analysis of particle configurations immediately surrounding each fluorescent particle due to image contrast from transmission of the emission photons through non-fluorescent particles. This study used the results to verify the presence of specific configurations of particles immediately adjacent to labeled particles within the photonic crystal – however it did not provide particle detailed positional information throughout the entire crystal structure.

Pros and Cons of PhC Hydrogel Fabrication Methods

Typical fabrication methodologies do not provide the ability to nondestructively assess the positions of individual particles within the crystal array, making them insufficient for the proposed study. Thus, a novel solution was proposed and implemented whereby the PhC hydrogel was fabricated using fluorescent particles within a hydrogel matrix. This approach allows fluorescent microscopy to image unique particles and support downstream positional analysis.

Most examples of photonic crystal fabrication in the scientific literature use sub-micron particles, including the use of 500 nm polystyrene [7], 570 nm and 409 nm polystyrene [8], 590 nm polystyrene [9] and 650 nm polystyrene [10] particles. The fluorescent particles selected in this study were chosen to be in the micron range instead

of the sub-micron range to maximize forward scattering (improving the signal strength of experimental debye ring generation) and ensure simpler fluorescence visualization under high magnification microscope (due to the larger particle size) to facilitate centroid identification for each particle.

Existing PhC Hydrogel Evaluation Methods

Typical PhC hydrogel evaluation which could provide particle positional information would use scanning electron microscopy (SEM). SEM-based monitoring of the final structure of the polymerized PhC is not well-suited due to the need of a vacuum chamber (i.e., it exerts physical stress on hydrogel and causes changes in morphology) and gold sputtering, which substantially degrades the quality of the substrate.

An alternative approach for PhC hydrogel evaluation occurs through evaluation of the diffraction pattern it generates in conjunction with existing analytical models. The scientific literature commonly [120] [121] [21] [122] calculates the particle spacing of a PhC hydrogel from the diameter of a debye ring using the formula $\sin(\alpha) = \frac{2\lambda}{\sqrt{3}d}$, where α refers to the scattering angle, λ the laser wavelength and d the average particle spacing. The computational model developed in the previous chapter demonstrated that this formula is only accurate for hexagonal configurations. For 2D configurations (2D array and centered square array), the computational model demonstrated that the equation for first-order constructive interference, $\sin(\alpha) = \frac{\lambda}{d}$, provides an accurate measurement of debye ring diameter.

<u>Pros and Cons of PhC Hydrogel Evaluation Methods</u>

The use of SEM is inadequate for PhC hydrogel assessment and monitoring due to its destructive nature, which prevents analysis of crystal structure in the hydrated hydrogel state. To overcome this, our approach utilizes confocal fluorescence microscopy to collect data cube mosaics over large regions. Using this data, particle positions must be extracted using centroid analysis. The typical approach used in modern studies has involved the calculation of a brightness-weighted centroid [123] or template matching approaches [124]. More modern approaches have also included analyses of brightness gradients using spherical harmonic functions to better detect antiparallel gradients on opposite sides of spherical objects [125]. An open-source MATLAB toolbox is also available which can support spheroid detection using analysis of the centroid, radial symmetry and partial radial symmetry [126]. For this study, Bitplane Imaris was used to automate the rapid collection of hundreds of thousands of particle centroids per dataset due to its convenience and broad acceptance as an established scientific tool for this purpose.

The use of analytical equations for characterizing PhC hydrogel structure is also inadequate due to the common imperfections created during experimental fabrication. Analytical equations are only designed for perfect 2D or hexagonal crystal structures – however experimental materials commonly contain a mixture of both configurations in unknown quantities. We hypothesize that mixed configuration polycrystals will generate a debye ring diameter which will be a weighted average of the two equations dependent on the relative frequency of hexagonal versus 2D configurations. We will validate this

hypothesis through characterization of a particle index, which aims to identify the configuration of individual imaged particles to assess the overall crystal structure.

While the proposed indexing approach is developed specifically for crystallite configuration analysis, efforts to perform pattern detection on self-assembled particle colloids is an active area of research. The ability to better characterize colloidal structure has received renewed attention due to advances in material science which aim to incorporate colloids into optoelectronics and biosensing but require a better method to predict physical properties from colloid self-assembly morphology [127]. Furthermore, being able to define a complex colloidal structure with a few key parameters can enhance understandings of colloidal interactions and the influence of preparation processes on the final colloidal pattern [128]. In a recent example from the scientific literature, colloidal structures had individual centroids identified and undergo Voronoi tessellation and Delaunay triangulation to characterize the presence of defects, pore distributions and the nearest-neighbor quantity [129]. This example demonstrates the scientific community interest for colloid analysis solutions, with the proposed one in this chapter being the first specific one for PhC hydrogel configuration analysis.

Objectives

In this chapter, a PhC hydrogel fabrication and analysis pipeline will be developed to facilitate validation of the previously described computational model. In parallel, existing theoretical models will be expanded by demonstrating enhancements to the analytical equation approach which support imperfect crystal structures. This process facilitates a quantitative link between experimental, theoretical, and simulated results.

Finally, an approach for particle structural analysis is developed which is nondestructive, improving the utility of the platform for research teams who require this type of assessment.

Methods

PhC Hydrogel Fabrication

Monodispersed fluorescent polystyrene (PS) particles solution (2 μm, Bangs laboratories, Inc.), was centrifuged for 10 minutes. The supernatant was removed, and the pellet was resuspended in DI water. This step was repeated several times to clean manufacturer provided solvent from the particles. In the final step the particles were suspended at 25% (w/v) and mixed with 8% (w/v) AG501-X8 (D) ion exchange resin (20–50 mesh, mixed bed, Bio-Rad, Hercules, CA, USA). The particles were ultrasonicated for 10 mins and shaken at 210 RPM for 1 hour. The PS solution was mixed with alcohol at a 3:1 ratio and 100 ul was injected into a microwell chamber made with glass slide, silicon spacer and coverslip. The solution was allowed to evaporate overnight. During the evaporation process, the polystyrene particles self-assemble into a PhC structure on the glass slide surface.

The pre-polymer solution was prepared by mixing acrylamide (Millipore sigma,USA) and bis-acrylamide (Millipore sigma,USA) in a molar ratio of 50:1, and 5 ul of a photo initiator DEAP (Fisher scientific, USA). The 150 ul of pre-polymer solution was then carefully injected from the side until the particle layer was completely covered with the polymer solution. To polymerize the PhC structure, a UV light (Black Ray 365 nm, mercury lamp) was illuminated 4 inches from the PhC structure for 40 minutes. After 40 minutes, the cured gel was washed with ultra-pure DI water. A volumetric change of the

hydrogel was observed. The PhC hydrogel was stored in air-dried condition and rehydrated

with DI water before usage. This process is highlighted in Figure 3.1.

[1]	[2]	[3]
Polystyrene Particles	Ion Exchange Resin	
Step 1: Cleaning Particle Solvent	Step 2: Ultrasonicate with Ion-Exchange Resin	Step 3: Orbital Shaking to Enhance Ion-Exchange
[4]	[5]	[6]
Step 4: Injection of Polystrene Solution Suspended in Ethanol for Overnight Drying	Step 5: Injection of Polymer Solution above Dried Photonic Crystal	Step 6: Photocuring of Photonic Crystal Hydrogel

Figure 3.1 PhC Hydrogel Fabrication. Fabrication of a PhC hydrogel consists of six steps. First, the polystyrene particle solution from the manufacturer undergoes multiple cycles of centrifugation, and DI water resuspension to remove all manufacturer solvents. Next, ion exchange resin beads are added and the solution is ultrasonicated. After ultrasonication, the tube undergoes further orbital shaking to enhance the ion exchange process. The polystyrene particles solution is then mixed with ethanol and injected in a microwell chamber and allowed to dry overnight. During the overnight drying, evaporation of the particles causes self-assembly of the PhC on the glass slide surface. Next, a polymer solution is injected on top of the dried PhC and allowed to infiltrate. The combination is then photocured.

Experimental Measurements of Diffraction Pattern

Fabricated PhC hydrogels with polycrystalline configuration produces Debye

Ring under illumination, shown in Figure 3.2. A monochromatic laser light source, 530

nm collimated source with a 2 mm spot size (Edmund Optics), is mounted on a laboratory

stand, which illuminates a PhC hydrogel mounted on a glass slide. The illumination axis

is perpendicular to the PhC hydrogel plane. An observation screen was placed below the

sample on which the debye ring diffraction pattern was projected, with the distance

67

between the PhC hydrogel and observation plane confirmed for each experiment. Since

the experimental study requires quantification of the debye ring dimensions, a

smartphone (Xiaomi Redmi Note 7) is mounted on the laboratory stand parallel to the

observation screen to collect an image of the diffraction pattern. An object of known size

[1 cm x 1 cm] was placed on the observation plane to support scaling of the camera

image. Three unique debye rings were imaged from different regions of the photonic

crystal. The debye ring is only formed in the presence of a self-assembled PhC.
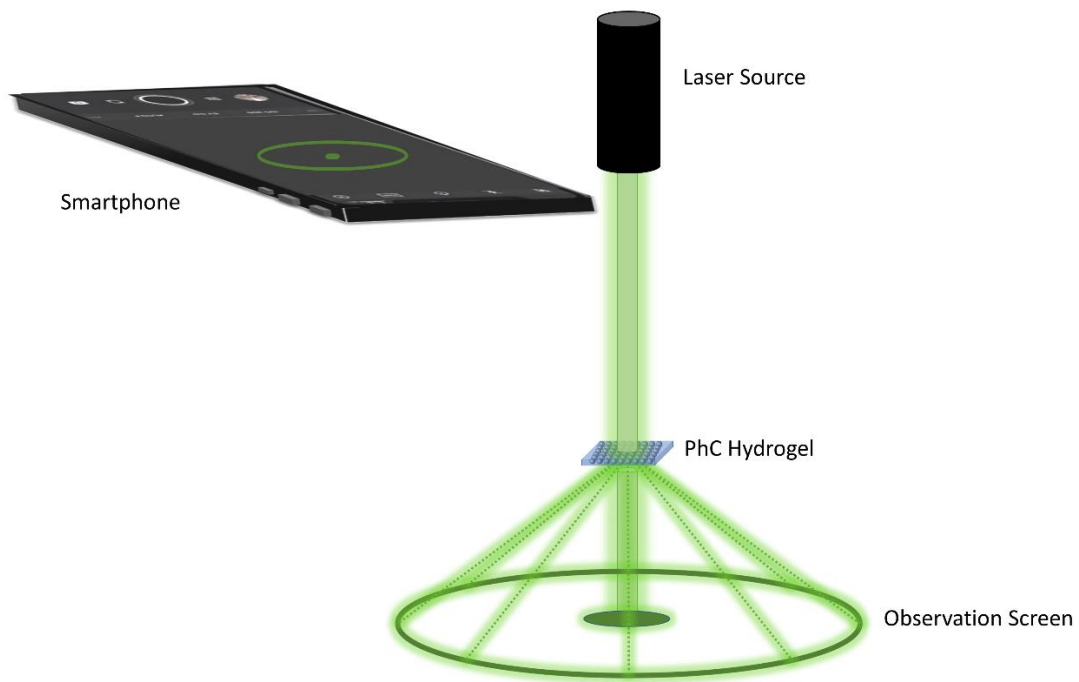
Figure 3.2 Debye Ring Experimental Measurement Technique. To generate an experimental diffraction pattern, a laser light source is attached to a laboratory stand and illuminates the mounted PhC hydrogel at an incident angle perpendicular to the PhC plane. A smartphone mounted parallel to the observation screen captures the diffraction pattern.

A smartphone was chosen as the tool for Debye ring characterization to

demonstrate that the platform can be readily assessed with consumer hardware. While a

smartphone is not as reliable for intensity characterization as a laboratory camera, it is

sufficient for geometric measurements of Debye ring diameter. The Xiaomi Redmi Note 7 collected the photographs using the FV-5 application, which allows fine control over image collection. This app was used to collect raw format, uncompressed camera data with automatic white balancing disabled. The following settings were used: F-stop: 1/8, ISO Speed: ISO-100, Exposure Time: 1/1000 seconds,

Focal Length: 5 mm, Image Dimensions: 3000x4000, Bit Depth: 24. Images were analyzed using ImageJ and MATLAB.

Quality Assessment of PhC Hydrogel: Confocal Imaging & Imaris Processing

Immediately after experimental measurements, each PhC hydrogel was imaged using a Nikon C2+ confocal laser-scanning fluorescent microscope. Reducing the delay between measurements is critical since the hydration state of the hydrogel significantly affects particle positioning.   Due to the use of confocal imaging techniques which capture very thin focal planes, XZ and YZ cross-sections of the image stacks can be assessed to validate that the crystal is 2-dimensional.

Mosaic scanning was performed for each PhC hydrogel at 3 locations, with a minimum size of 3 x 3 panels per location. Using a 20x magnification objective + 3x optical zoom, 1-1.5 mm^2 was analyzed per PhC hydrogel across all locations. A 20x magnification objective was critical since a 60x oil immersion objective may generate pressure which would impact the validity of subsequent particle spacing measurements. The 20x objective combined with the 3x optical zoom provided a panel size of 210 x 210 microns, which due to the 1024x1024 size of each image (16-bit depth) resulted in an image resolution of 0.205 microns per pixel. A pixel dwell of 2.4 nanoseconds was

incorporated and a Z-spacing of 1 micron was used over the PhC thickness across the

mosaic. The Z-sectioning capabilities of confocal microscopy enhances the ability to

later determine the centroid of each particle. Imaging was performed using the

microscope's 'FITC' channel setup, which was composed of a 488 nm excitation laser

and an emission filter with a central wavelength of 510 nm and a bandwidth of 84 nm.

Using Bitplane Imaris 8.3.1, each TIFF image stack could be used to extract

discrete particle positions through using the 'Spot' functionality to identify spherical

objects. Each PhC hydrogel imaged yielded over 100,000 distinct particles whose

location could be accurately assessed across the locations imaged. Imaris generates a

.csv format output which describes the particle positions in three dimensions which is

used for further analysis.

Simulation of Diffraction Pattern from Particle Positions

The array of particle positions extracted from the raw microscopy images using

Bitplane Imaris was then used as an input into the computational simulation previously

developed. The observation screen distance, laser wavelength and Mie constants were

used to generate a [500 x 500] pixel image representing a [12 x 12] cm observation plane.

Measurement of Debye Ring Diameter

The Debye Ring diameter for both experimental (collected from smartphone) and

simulated (collected from computational model) diffraction patterns were measured using

the same method. A square 5 mm simulated photodiode was scanned along the

horizontal as well as vertical axis of the debye ring image for both the smartphone image

of the experimental diffraction pattern as well as the diffraction pattern generated by the computational model. At each point in the scan along the axis, the total pixel value from the simulated photodiode area is summed. The resolution of the resulting profile is therefore based on the resolution of the diffraction pattern image, which was 0.24 mm/pixel in the computational model and 0.2 mm/pixel from the experimental assessment using a smartphone. The resultant profile of the scanned photodiode provides a characteristic peak at each side of the debye ring as well as at the transmission point at the center of the ring. To reliably measure the ring diameter, the derivative was taken of the line profile. The intensity peak on each side of the debye ring corresponds to a derivative of zero. The debye ring diameter measured from the horizontal and vertical axes of the ring are then averaged to generate an overall diameter for each debye ring.

PhC Hydrogel Indexing

By identifying each particle's position, it is possible to assess whether it is part of a crystallite structure of a defined configuration. Additionally, by characterizing the relative frequency of hexagonal vs 2D oriented crystallites, it is possible to enhance existing theoretical models which only provide analytical solutions for perfect crystals of each type. Therefore, this improvement has led to the creation of an 'enhanced theoretical model.' To determine the particle configuration, an expanding-search nearest neighbor analysis was carried out per particle. The search radius was initialized to the particle diameter and the radius was incremented by ¼ of this diameter each time it was expanded. As centered square and 2D array configurations both generate the same theoretical solution, they were combined into a single scenario, whereby either 4 or 8 neighbors were found. In contrast, hexagonal configurations are characterized by having

6 neighbors. When the number of neighbors found was less than 4, the search radius

would be increased. If the number of neighbors did not conform to the target values

[4,6,8] but over 4 neighbors were found, the particle was removed from consideration due

to the high likelihood of microscopic error. This algorithm is shown in Figure 3.3.

Particle Configuration Indexing & Display
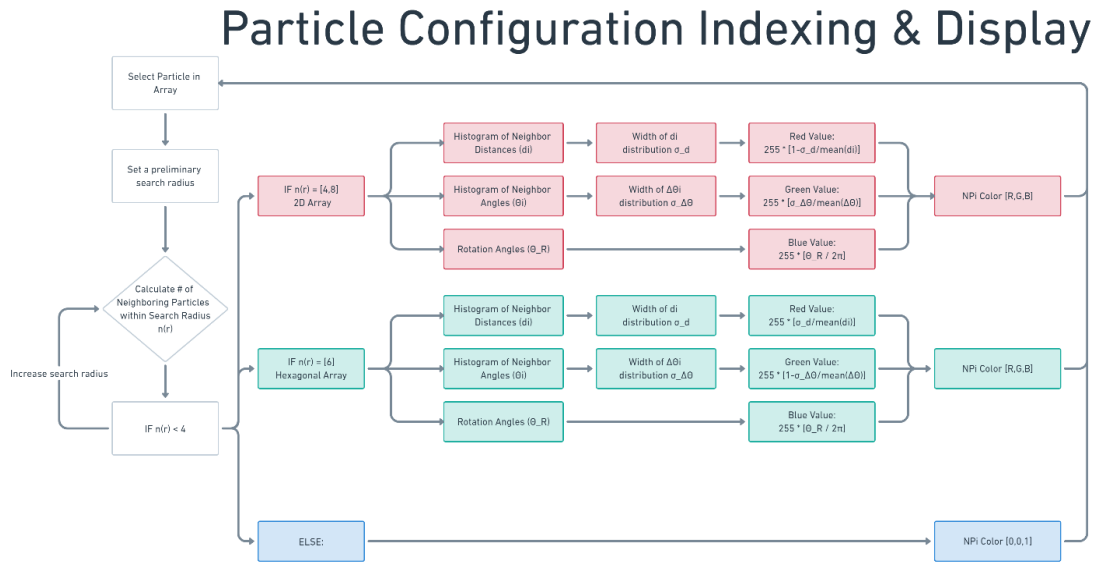
Figure 3.3 Particle Indexing Algorithm. The particle indexing algorithm uses an expanding search technique to identify the quantity of nearest neighbor particles. The preliminary search radius begins at the boundary of the current particle, and incrementally increases. For perfect crystals, a quantity of particle neighbors representing 4, 6, or 8 corresponds to one of the known geometric configurations (2D, hexagonal, centered square). Due to microscopic or macroscopic error, the quantity of nearest neighbors may not match any of these patterns and an additional category is used. For particles which match the known configurations, the distribution of nearest-neighbor distances and rotational angles of the particle array are used to fine-tune the particle color, allowing for distinction not only between different configurations, but also between adjacent crystallites with the same configuration but different rotation.

Once the particle type was identified, it was assigned an RGB value to generate a

convenient visual representation of the crystal structure. Generally, 2D particles would

appear red, hexagonal particles would appear green and particles with microscopic error

would appear blue. The variability in nearest-neighbor distance and nearest-neighbor

angle as well as the rotational angle of the crystallite formed around the particle serve as

additional inputs to the RGB value, providing a unique shade of color corresponding to each particle's unique characteristics. This can cause microscopic error to reduce the appearance of a 2D crystallite from a pure red to a blended red-yellow color.

To generate an index, the number of hexagonal and the number of 2D/Centered square particles are extracted after running the indexing algorithm for each particle in the dataset. Using this data, a normalized index is generated where 0 represents only 2D/Centered square particles and 1 represents only Hexagonal particles, using the following formula:

$$\text{Index} = \frac{\#\ Hexagonal\ Particles}{(\#\ Hexagonal\ Particles + \#\ of\ 2D\ or\ Centered\ Square\ Particles)}$$

This index is also used to predict the debye ring diameter by leveraging existing theoretical models. First, two theoretical diameters are predicted based on the assumption of either a perfect hexagonal or perfect 2D crystal. Afterwards, the predicted diameter based on the particle index is calculated using a weighted average based on the Index, using the following equation:

$$Predicted\ Diameter = (Index * Theoretical\ Hexagonal\ Diameter) + ((1 - Index) *$$
$$Theoretical\ 2D\ Diameter).$$

Validation of Particle Configuration Indexing and Enhanced Theoretical Model

To validate the particle configuration indexing approach and its relationship to the enhanced theoretical model, the computational model was used to generate crystal structures with a known ratio of hexagonal to square crystallites and known quantities of microscopic error. Microscopic error was tested at 0% (perfect spacing), 10%, 20% and 50%. The hexagonal to square crystallite ratios tested were 100% : 0%, 75% : 25%,

50% : 50%, 25% : 75% and 0% : 100%. Fixed parameters included the particle spacing (2 um), crystallite size (25 x 25 particles), and crystal size (4 x 4 crystallites). The expected index was calculated based on the ratio of hexagonal and square crystal structures, with '1' representing all hexagonal structures and '0' representing all square structures. The actual index was calculated for all combinations of microscopic error and hexagonal : square crystallite ratios to validate the indexing algorithm and assess the impact of microscopic error.

Comparison of Simulated, Theoretical & Experimental Results

To test the efficacy of the computational simulation and the enhanced theoretical approach, nine unique PhC hydrogels were fabricated. From each, a minimum of 3 experimental debye rings were captured as well as 3 unique locations scanned with fluorescence microscopy. The compilation of all of the previous methodologies described allowed creation of an analysis pipeline, which is also highlighted in Figure 3.4. The pipeline begins with the fabrication of a PhC hydrogel and experimental imaging of its diffraction pattern using a smartphone. The PhC hydrogel then undergoes fluorescent confocal imaging and Bitplane Imaris is used to convert the image data to an array of unique particle positions. This particle position array serves as an input into the indexing algorithm to generate a configuration 'index' for the PhC hydrogel. The experimental conditions used during experimental study are combined with the index to generate an 'enhanced theoretical' debye ring diameter. Finally, the particle positions from Bitplane Imaris are combined with the experimental conditions and are inputted into the computational model to generate a simulated debye ring diameter.

The analysis pipeline generates a unique Debye Ring diameter for the experimental, simulated and enhanced theoretical approach, which is then compared statistically. A Kolmogorov-Smirnov test was used to demonstrate normality, which allowed a subsequent ANOVA to compare the 3 methods for each photonic crystal hydrogel.
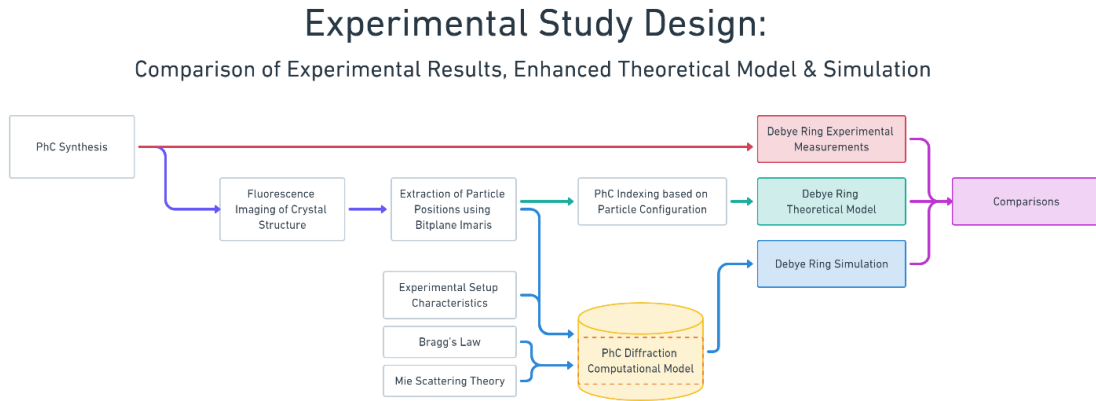
Figure 3.4 Experimental Study Design. *The experimental study design aims to compare experimental diffraction patterns with the predicted diffraction pattern based on the new 'enhanced theoretical model' and the computational model generated in the previous chapter. First, a PhC hydrogel is synthesized. Experimental measurements of the PhC hydrogel generates a diffraction pattern and debye ring diameter and the experimental conditions are recorded to be used as input to the other two approaches. Fluorescence imaging of the crystal structure and subsequent extraction of particle positions using Bitplane Imaris serves as the source of input to these alternative approaches. A configuration index is generated using the particle positions, which is then combined with the experimental characteristics to generate a predicted debye ring diameter based on this new 'enhanced theoretical' model. The particle positions and experimental characteristics both serve as inputs to the computational model to generate a simulated diffraction pattern, whose debye ring diameter is extracted for comparison to the other two approaches.*

Results

PhC Hydrogel Fabrication

Nine PhC hydrogels were fabricated using the described method, each approximately 1x1 cm in diameter. Figure 3.5 provides representative images throughout the process.
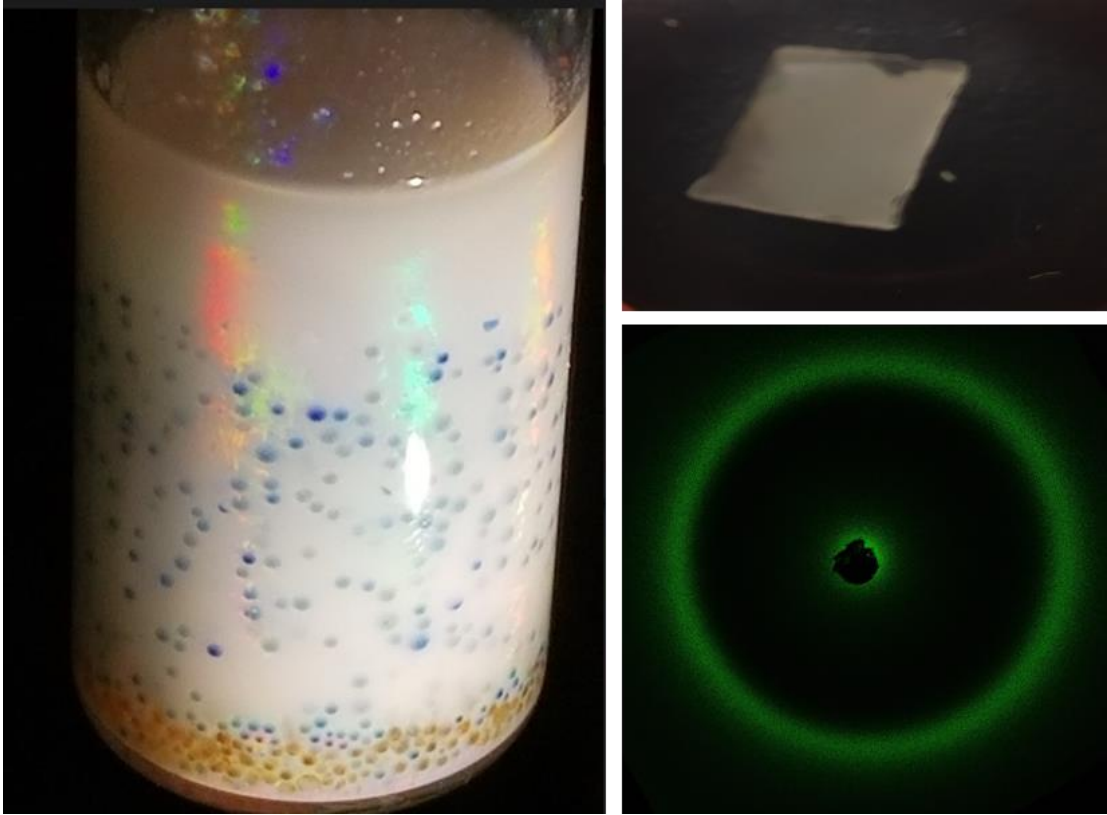
Figure 3.5 Representative Images of Fabrication Process. The fabrication process begins with extensive mixing of the particle suspension in ion-exchange resin. The emergence of iridescence seen in the image provides an indication of the success of this step. The subsequent fabrication steps result in the creation of the PhC hydrogels shown in the top-right of the figure. A representative image of the debye ring generated using the PhC hydrogel is shown in the bottom-right. The center of the observation screen has a hole to remove the transmission axis spot, whose brightness reduces the ability to analyze the debye ring.

Quality Assessment of PhC hydrogel

A representative image of the imaged PhC hydrogel is shown in Figure 3.6. This figure highlights the complexity of the crystal structure, its relatively small individual crystallites and the lack of lakes or fractures seen commonly in the scientific literature.
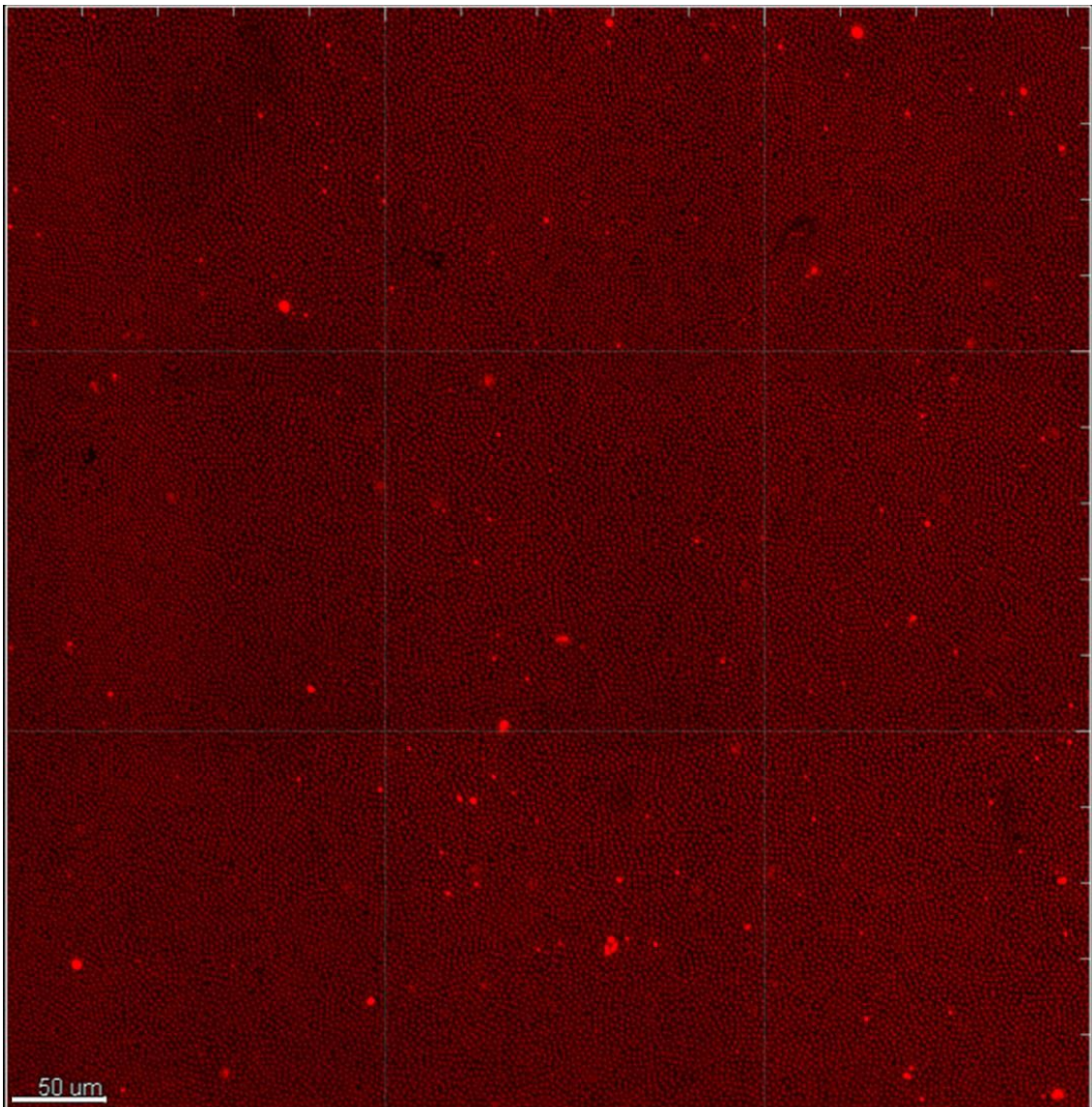
Figure 3.6 Particle Positional Extraction. Extracting Particle Positions using Fluorescence Microscopy & Bitplane Imaris. For the experimental study, between 1 and 1.5 mm^2 was collected from each PhC sample at 20x magnification with an additional 3x optical zoom. Confocal imaging of each sample was performed immediately after the diffraction pattern was imaged to ensure parity between both conditions. A mosaic scanning and stitching technique was used to collect this data.

Debye Ring Comparison

Calculation of Debye Ring Diameter

The experimental debye ring measurements and the simulated debye ring

generation using confocal data both provide an image of a debye ring whose diameter

must be measured. As shown in Figure 3.7, measurement of diameter is not straightforward as the presence of microscopic error broadens the ring thickness. To resolve this challenge, a methodology was created which allows for diameter measurement. A simulated square photodetector is scanned along the X and Y axes of the image, summing all intensities within as it scans through the image. This approach smooths the noisy data and allows for clear visualization of the peak on each side of the debye ring. The derivative of the resultant line profile is then calculated to identify the zero-derivative point at the peak of the ring intensity distribution. The horizontal and vertical profiles are averaged to provide an overall diameter.
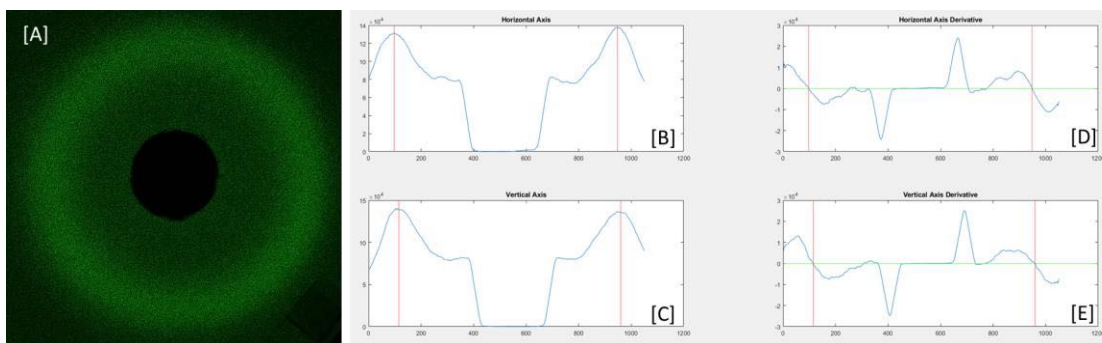
Figure 3.7 Ring Diameter Measurement Methodology. *Ring Diameter Measurement Methodology. To measure the ring diameter of the experimental diffraction pattern (A), a simulated photodetector was scanned across the horizontal and vertical axes of the image. The intensity along the horizontal and vertical axes is shown respectively in (B) and (C). The derivative is then calculated for each of these profiles in (D) and (E). The horizontal green line in (D) and (E) represents a derivative of zero. Its intersection with each side of the debye ring is highlighted by a vertical red line in both sets of images.*

Comparison of Experimental, Simulated and Enhanced Theoretical Results

For the nine fabricated PhC hydrogels, the debye ring diameters were generated using three methods. The first method, experimental, collects an image of the debye ring generated under monochromatic illumination. The second method, simulated, uses the unique centroid of each particle collected during microscopy as an input to the

computational model to generate a resultant diffraction pattern. The final method,

enhanced theoretical, applies the particle indexing methodology to the particle centroid

data to identify the 'index' of the crystal and predict the debye ring diameter using a

weighted average of the square and hexagonal analytical equations. The results of the

subsequent analysis and representative data for the simulated, experimental, and

enhanced theoretical are shown in Figure 3.8. Debye ring diameter is shown in two

different ways – (1) by a measured diameter and (2) by the diffraction angle which

generates the measured ring. The experimental condition of the first three gels uses a

shorter distance from observation screen to the gel, thus resulting in a smaller debye ring

compared to others. The effect of the specific observation screen distance is removed by

considering the debye diffraction angle. The debye ring diameters from experimental,

simulated and enhanced theoretical versions were typically within millimeters of one

another, validating the ability of the enhanced theoretical and simulated approaches to

predict experimental results. Of the nine PhC hydrogels, only two were found to have

significantly different outcomes between the 3 approaches following ANOVA analysis.
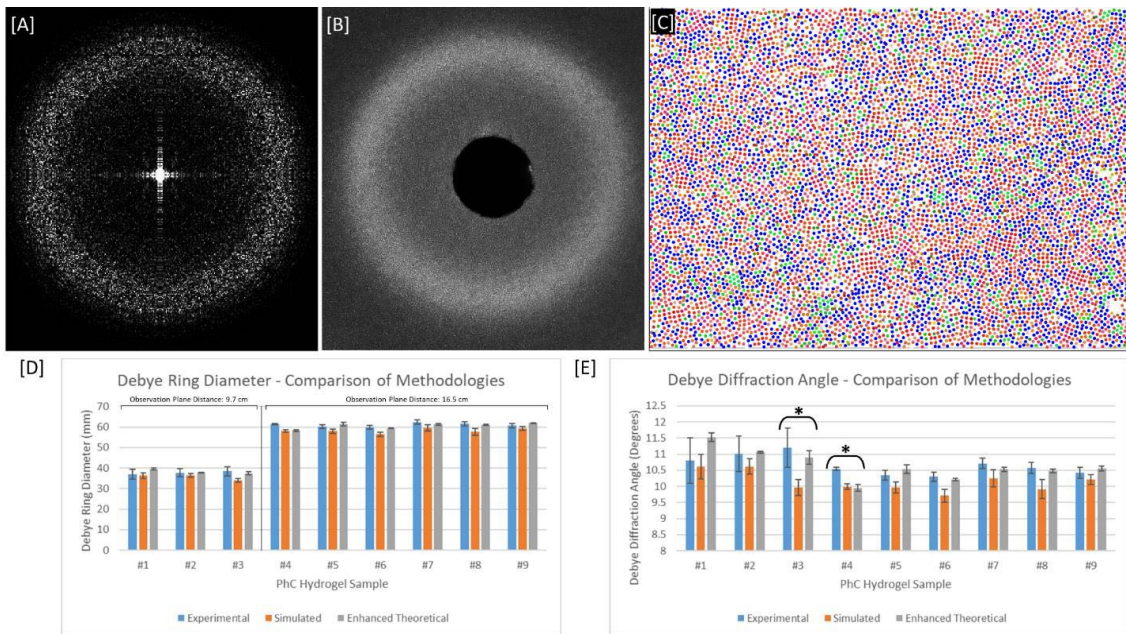
Figure 3.8 Experimental Study Results. *Representative images are shown for the simulated debye ring [A], experimental debye ring [B] and particle array colorized using the indexing algorithm [C]. Results with standard error bars are shown for both debye ring diameter [D] as well as debye diffraction angle [E] (calculated using the ring diameter and observation screen distance according to the equation $\tan(\theta) = \frac{debye\ ring\ radius}{screen\ distance}$. The debye ring diameter is smaller for the first three samples since the PhC was placed closer to the screen – a distance of 9.7 cm instead of the distance of 16.5 cm used in the later samples. As shown in the diameter comparison, the typical difference in the calculated Debye Ring diameter between each method within a single sample is only a few millimeters. A Kolmogorov-Smirnov test found no deviation from normality for any sample, so an ANOVA was performed on the debye diffraction angles for each sample to compare the 3 methodologies. For only samples 3 and 4 a significant difference was identified at the 0.05 significance level.*

Particle Indexing Validation

To demonstrate the efficacy and limitations of the particle indexing methodology, the computational model was used to create simulated polycrystals with varying ratios of crystallite configurations and quantities of microscopic error. These simulated polycrystals served as inputs to the indexing algorithm, which aimed to correctly characterize the relative proportion of each configuration (hexagonal vs 2D/Centered Square) and predict the experimental debye ring diameter more accurately than the existing theoretical models can provide. The theoretical model only provides solutions

80

for a perfect hexagonal or perfect 2D crystal, but experimental PhCs will always fall

between those two values, depending on the relative proportion of each configuration.

As shown in Figure 3.9, the ability to predict the configuration degrades as microscopic

error is added. Even under conditions without any microscopic error, the indexing

algorithm is superior at identifying 2D configurations over hexagonal configurations.

This is due to the potential for incorrect categorization when a nearest-neighbor search in

a hexagonal configuration finds 4 instead of 6 neighbors – for example at a crystallite

border. This is far more likely than the inverse scenario, leading to a better overall

accuracy for 2D crystallite identification. Despite this challenge, the algorithm provides

value for microscopic error up to approximately 20%, where it begins to rapidly degrade

due to the inability to trust nearest-neighbor particle counts for determining crystallite

structure.

Simulation Results

Microscopic Error		100% Hex 0% 2D	75% Hex 25% 2D	50% Hex 50% 2D	25% Hex 75% 2D	0% Hex 100% 2D
Microscopic Error	Expected Index	1.0	0.75	0.5	0.25	0
[A] 0%		0.9125	0.6976	0.4815	0.2480	0.0154
[B] 10%		0.9110	0.6948	0.4712	0.2413	0.0136
[C] 20%	Actual Index	0.6163	0.4797	0.3427	0.2358	0.1380
[D] 50%		0.3496	0.3450	0.3437	0.3372	0.3452

Figure 3.9 Impact of Microscopic Error on Particle Indexing. The impact of microscopic error and particle configuration on the indexing algorithm was tested. At low levels of microscopic error, the algorithm would more often misclassify hexagonal particles as 2D than misclassify 2D particles as hexagonal. This is attributed to the higher likelihood of 4 nearest-neighbor particles being found than 6 when microscopic error is present. Additionally, when microscopic error begins exceeding 20%, the ability of the algorithm substantially degrades.

82

Discussion & Conclusion

Summary of Accomplishments

Following the development of the computational model in Chapter 2, this chapter validates it by comparing its outcomes to experimental results and existing theoretical models. This process has led to the development of many novel and impactful advances in photonic crystal fabrication and analysis. First, this approach prompted the development of a PhC hydrogel fabrication methodology incorporating micron-scale fluorescent particles – typically nano-scale particles are used which have no fluorescent properties. Additionally, an analysis strategy was developed where fluorescent PhCs are imaged using confocal fluorescence microscopy, position of the particles are extracted using Bitplane Imaris and used as an input to both the computational model and in enhanced theoretical model. The enhanced theoretical model uses a novel particle indexing technique to assess the relative presence of 2D versus hexagonal crystallites within the larger crystal structure. This work is especially impactful as it demonstrates a mechanism for non-destructive particle position analysis within a PhC, as typical approaches commonly use destructive SEM as an analytical tool. Furthermore, by linking experimental, simulated, and enhanced theoretical results, this work will support researchers in linking the diffraction pattern dimensions to the underlying particle spacing.

PhC Hydrogel with Fluorescent Microparticles

Advantages

The use of fluorescent particles in the fabrication of PhC hydrogels enables a new opportunity to nondestructively assess the quality of the PhC hydrogel sensors. The particles can be easily visualized with a fluorescence microscope, avoiding the sputtering and vacuum pressure processes which are required to analyze the internal structure of the materials under scanning electron microscopy (SEM). SEM is the most common tool used for assessing microstructure of photonic crystal materials [130]. For hydrogels, SEM additionally requires a dehydration preparation step [131], which will substantially reduce the ability to predict its hydrated microstructure.

Disadvantages/Challenges

While these improved fabrication techniques are beneficial for later analysis, they create some accompanying challenges. Due to the use of fluorescently labeled particles, it is important to minimize light exposure to samples in order to maximize the later fluorescent signal. Additionally, fluorescent particles have limited long-term stability – typically between six months to a year, reducing the usable lifespan of the resultant PhC hydrogel.

PhC Hydrogel Evaluation Tools

A corresponding data analysis workflow was used to generate the position of each imaged particle in the crystal structure. The implementation of the previously described computational simulation and the new particle indexing method allows several advantages, such as cross-validation of the photonic crystal fabrication technique and prediction of the experimental Debye ring characteristics.

Particle Position Identification (Confocal Fluorescence Microscopy + Bitplane Imaris)

Advantages

The use of confocal fluorescence microscopy is very advantageous for particle position identification due to its ability to optically section the sample being imaged, allowing the collection of a very narrow focal plane. Through collection of a finely spaced Z-stack, the individual cross-sections of the microparticle imaged allow for a more accurate prediction of the centroid of the particle than would be allowed with widefield fluorescence microscopy. Furthermore, the use of fluorescence microscopy ensures high contrast between the fluorescent particle and the non-fluorescent medium, improving the likelihood of accurate particle positional identification. In conjunction with the Bitplane Imaris software, hundreds of thousands of particle centroids can be readily extracted.

Disadvantages/Challenges

A limitation of this methodology is the challenge of ensuring all the illuminated particles from experimental debye ring collection are captured during fluorescent mosaic scanning. While the spot size of the illuminating laser is only a few millimeters in diameter, this is still a larger area that can be reasonably captured using high-magnification fluorescence microscopy due to both the quantity of imaging time required as well as the gel hydration state, which slowly dehydrates during the scanning process. If a long, automated imaging routine is performed using fluorescence microscopy then the spacing of the particles will differ between its beginning and end due to hydration state changes.

<u>Computational and Enhanced Theoretical Models to Predict Diffraction Pattern</u>

Advantages & Disadvantages of Computational Model

The computational model is a valuable tool to transform the positional data extracted by Bitplane Imaris into a diffraction pattern whose geometric properties can then be compared with the experimentally imaged pattern. One of the limitations of the computational model is due to its use of the single-particle Mie scattering model, which results in incorrect intensity distribution information in the diffraction pattern. Despite this limitation, the computational model is still sufficient for predicting the geometric dimensions of the resulting diffraction pattern.

Advantages & Disadvantages of Enhanced Theoretical Model

The enhanced theoretical model provides a valuable improvement to the existing analytical equations which only work under the limited circumstances of a perfect square (2D array/centered square) and perfect hexagonal configuration. While this is a useful improvement, it requires extraction of per-particle positional data – requiring a workflow like the one presented in this chapter. A major disadvantage of this approach is its reliance on low microscopic error to be present in the experimental sample, which is challenging to control.

Challenges of Characterizing PhC Hydrogel Experimentally

While these experiments were successful in linking the results of the computational model, experimental diffraction pattern, and existing theoretical models, there are limitations based on the existing techniques. One of the most prominent is the dependence of results on the PhC hydration state. Once a PhC has been fully rehydrated and mounted on a glass slide for analysis, the gradual dehydration of the hydrogel slowly

reduces the average particle spacing as well as the flatness. Due to this, the average particle spacing which generates the experimental diffraction pattern will never be identical to the average particle spacing found when collecting experimental particle positions during fluorescent microscopy.

<u>Particle Organization Index</u>

Insights from Scientific Literature

Since the use of particle indexing in PhC hydrogels is novel, there is very limited available work for comparison in the scientific literature. The closest examples can be found in colloidal analysis. While fluorescent particle analysis is widespread for colloidal analysis, this has not yet been utilized to drive research on PhCs. Research on fluorescent particle colloids includes assessment of protein-protein interactions through the colloidal aggregation of surface protein-labeled fluorescent polystyrene microparticles [132]. This research similarly performs analysis of colloidal particle configurations, but its focus is primarily on the development of methods to drive programmed colloid assembly through surface protein associations. Additionally, research on pattern analysis in colloidal assembly identifies the value of a nearest-neighbor approach for identifying configurations of unit cells [129], providing evidence as to the value of the developed approach.

Furthermore, it is valuable to consider whether the mixture of particle configurations found in our experimental PhC hydrogels has been described in the scientific literature. One research team has put effort into performing a meta-analysis of outcomes across research groups [133]. This team created a directory of self-assembly outcomes across research groups, focusing on the self-assembly method and substrate to

identify the resulting crystalline properties. They found that certain techniques produce only square configurations, certain ones produce only hexagonal configurations, and some generate a mixture of the two – an outcome which was also found in our study. The combination of technique and substrate used in our protocol was found to have created both square and hexagonal configurations in other group's outcomes, validating our findings.

Potential Utilities

Using this knowledge of the relationship between indexing and analytical equations, experimenters studying debye ring diffraction patterns can better associate their experimental outcomes to the crystal structures of their experimental platforms. Furthermore, since unique combinations of self-assembly method and substrate can create either a single configuration or an expected combination of the two, researchers can better assess the outcome of their fabrication approach by considering how their experimental outcomes align with the two existing analytical equations.

Limitations

One of the major limitations of the particle indexing method is the potential mischaracterization of hexagonal configurations as square due to either microscopic error or crystallite borders. In both circumstances, if the expanding radial search algorithm finds only 4 particle neighbors the particle will be characterized as a 2D square configuration. This may be unavoidable in the presence of microscopic error, but future improvements in the underlying algorithm design may drive better identification of crystallite borders. Another significant limitation is the rapid degradation of indexing success as the quantity of microscopic error exceeds 20% of the average particle spacing.

Due to this, the computational model is invaluable as its effectiveness is independent of the positional error of the crystal.

<u>Future Work</u>

To overcome the risk of hydration state fluctuations during measurement, future work can include development of a sealable reservoir within which the PhC hydrogel can undergo both experimental diffraction pattern generation as well as confocal imaging without the worry of changes in hydration state. Additionally, the particle indexing algorithm can undergo further improvements to better identify the presence of crystallite borders, at which the indexing approach loses its accuracy.

Chapter 4: Biomedical Application of PhC Hydrogel: Ultrasound Detection

Introduction

Review of PhC Biomedical Sensors

      PhC hydrogel sensors are commonly used to detect chemical reagents, mechanical forces, and gases. Selective choices of hydrogel have allowed for the selective detection and quantification of analytes such as lectin [73] and glucose[74,75] as well as environmental conditions such as the pH[76,77] or concentration of ethanol[77]. When fabricated in unique geometries such as photonic crystal fibers, the platforms can become sensitive to mechanical forces including twist / torsion [85] [86] and vibration [89][90]. Finally, the porous nature of PhC hydrogels make them highly suitable for gas sensing, such as for methane [94].

Review of PhC Pressure Sensors

      Photonic crystals have been used as physical pressure sensors in the recent scientific literature. One interesting use case implemented photonic crystal fibers for the measurement of hydrostatic pressure[134], which measures the static pressure of a liquid column. Photonic crystal fibers due to their fabrication have intrinsic birefringence, and this birefringence can be monitored to detect changes in the hydrostatic pressure. Another use case was a nano-pressure physical sensor with a 13 nN detection limit which was fabricated through development of an inverse 2-dimensional PhC composed of a hexagonal lattice of air holes in Silica [135]. A waveguide is created by removing a single line of the air holes, which generated a nanocavity with a distinct resonant wavelength. A final example in the literature is an air-bridge silicon line photonic crystal slab waveguide which was used for measurement of physical pressure [136].

Under physical pressure, it is expected that the elastomeric hydrogel will flatten along the axis of pressure and stretch over the perpendicular plane. This will cause a proportional change in the nearest-neighbor particle spacing based on the degree of pressure, also thereby reducing the index of refraction of the photonic crystal. These changes will cause a subsequent shift in the diffraction pattern, which can be detected on the observation plane.

Review of Ultrasound Sensors

The use of ultrasonic transducers clinically has been steadily evolving for the past 50 years, with each developed transducer providing a unique center frequency, sensitivity and form factor [137]. Broadly, advancements in ultrasound detection can be divided into two technologies – traditional acoustic detection and optical detection. Optical detection provides the potential for contactless detection and the capability to tune detection wavelengths for focusing on particular tissue targets, although this comes at the cost of penetration depth [138]. Traditional acoustic detection using physical transducers can be further subdivided into conventional piezoelectric and micromachined transducers.

Acoustic Detection using Physical Transducers

Conventional piezoelectrics are the most common tools for commercial ultrasound detection and function based on a combination of the converse and direct piezoelectric effect. The converse piezoelectric effect is a phenomenon characterized by the generation of mechanical strain in a material due to an applied electrical field while the direct piezoelectric effect is characterized by the generation of electrical activity as a result of applied mechanical energy [139]. The converse piezoelectric effect thus converts an input electrical signal into an ultrasonic wave while the direct piezoelectric

91

effect allows for conversion of an ultrasonic wave striking a piezoelectric surface into a detectable electrical signal. The converse piezoelectric effect results in what is traditionally called 'transmission mode' of an ultrasonic transducer, where the alternating electric field across the piezoelectric material creates oscillating mechanical expansion and contraction [140]. The direct piezoelectric effect results in what is traditionally called 'receive mode' of an ultrasonic transducer, where the potential difference across the piezo-electrodes oscillate as an ultrasonic wave strikes. Piezoelectric transducers typically sandwich the piezoelectric element between a backing material and an impedance matching layer to reduce backscattered ringing. Piezoelectric materials are typically engineered to maximize the coupling coefficients, bandwidth and sensitivity, and include materials such as barium titanate[141], lithium niobite[142], zinc oxide [143], lead magnesium niobate-lead titanate [144] and lead zinc niobate-lead titanate [145].

Micromachined transducers are the newest generation of transducers, which leverage microfabrication processes. One category, capacitive micromachined ultrasonic transducers uses an array of miniature capacitors composed of a suspended membrane of silicon nitride resting on dielectric posts above a hollow cavity [146]. These capacitive transducers use electrostatic physical principles for ultrasonic wave generation and provide a lower-power option with improved stability, higher sensitivity and broader bandwidth [147]. An alternate micromachined transducer is the piezoelectric micromachined ultrasonic transducer, where a thin-film piezoelectric layer is deposited as a diaphragm on a silicon substrate. Compared to the larger piezoelectric transducers, micromachining reduces cost and improves sensitivity.

Acoustic Detection using Optical Transducers

Optical ultrasound detection can be subdivided into two categories – interferometric and refractometric [148]. Refractomeric techniques leverage the photoelastic principle, where acoustic waves induce mechanical stress in the medium – changing the refractive index proportionally with pressure. An optical interrogating beam will exhibit changes in the intensity, deflection angle or phase. Interferometric techniques monitor changes in the optical interference patterns induced by mechanical forces in the target material.

An example of interferometric techniques includes two-beam methods such as Michelson interferometry and Mach-Zehnder interferometry, where a laser beam is split into two paths – one disturbed by ultrasound and the other acting as a reference beam. At the interferometer output, the intensity of the beam is modulated by the ultrasound wave [148]. Resonator-type interferometric techniques have also been developed using common geometries such as the Fabry-Perot interferometer [149], micro-ring resonator [150] and fiber Bragg gratings[151].

Refractometric techniques are commonly classified as intensity sensitive, beam deflective and phase sensitive. Intensity sensitive methods are characterized by changes in intensity due to a beam transmitting through the interface of two media with different refractive indexes in the presence of ultrasonic waves [152]. Beam deflective methods are characterized by a small change in the angle as a beam transmits through a medium due to modulation of its refractive index, which is detected using a position-sensitive detector [153]. Finally, phase sensitive methods pass a beam affected by ultrasonic

waves through a spatial filter, with the components monitored by a CCD or CMOS camera [154].

Despite the benefits of optical transduction, the technology is slower than electrical transduction, attributed partly to the scanning time required. Furthermore, the reliance on continuous wave laser sources is problematic since these lasers can be sensitive to temperature and vibration.

Significance of PhC-based ultrasound sensors

Due to the sensitivity of PhC hydrogels to small changes in particle spacing, an intriguing biomedical use case for them is in the detection of ultrasonic waves. This relies on an underlying assumption that the periodic cycles of compression and rarefaction induced by an ultrasound source would cause displacement of the particles within the crystal, modulating the optical signal captured from the diffraction pattern. If this technique is fully validated, the ultrasound source could be replaced with a pulsed laser source and an all-optical ultrasound platform developed around the PhC hydrogel material. This is an exciting use case since all-optical ultrasound traditionally enhances the signal-to-noise ratio per unit area and detection bandwidths over traditional piezoelectric detectors [148]. Once commercialized, this technology can support a variety of use cases, including noncontact ultrasonic detection, interventional imaging, and magnetoacoustics.

Objective of this Chapter

In this chapter, photonic crystal hydrogels are evaluated as a material capable of sensing ultrasonic waves. It is expected that the debye ring diffraction pattern described previously will be modulated by the transverse waves generated in the elastomeric

material due to modification of the particle spacing. Material deformation will also modulate the bulk refractive index, resulting in a measurable change in the optical signal.

Prior to experimentation with ultrasonic pressure waves, preliminary experiments were carried out to verify the responsivity of the platform to physical pressure. An underlying hypothesis of this research aim is that the mechanism of physical and ultrasonic pressure responsivity would be similar enough that preliminary testing with physical pressure could serve as a prerequisite for ultrasonic pressure studies.

Unlike static physical pressure, ultrasonic pressure propagates through a medium by sinusoidally displacing molecules parallel to the propagation - described as longitudinal wave propagation. The propagation of wave alternates between compressions and rarefactions. In elastic solids, perpendicular displacement to the direction of propagation can be seen in addition to the parallel axis displacement. A core hypothesis of this research aim is that these transverse waves, which will be parallel to the plane of the 2D PhC, will cause periodic modulation of the particle spacing which reflects the same characteristics as the ultrasound wave being transmitted perpendicularly through the 2D PhC. This is only possible due to the elastomeric property of a PhC hydrogel.

Methods

<u>Physical Pressure Testing</u>

Before testing the PhC hydrogel's capability to detect high-frequency ultrasound, a preliminary study was carried out to assess the impact of static physical pressure on the diffraction pattern characteristics. To conduct this experiment, the PhC hydrogel was placed in between of a glass slide and cover glass attached to a 3D-printed apparatus,

which applied four points of equally spaced pressure, as shown in Figure 4.1 below. On

top of this apparatus is mounted a Mark-10 force gauge, which measures the pressure

applied to the photonic crystal. The entire system is mounted on a vertical positioning

system controlled by a handwheel. Gentle adjustment of the handwheel allowed a

controllable amount of pressure to be applied to the PhC, which is then displayed on the

Mark-10 digital display. A 532 nm laser (Edmund Optics, Sting Ray) was used to

illuminate the hydrogel to generate a diffraction pattern on the observation screen below,

which was then photographed and measured.
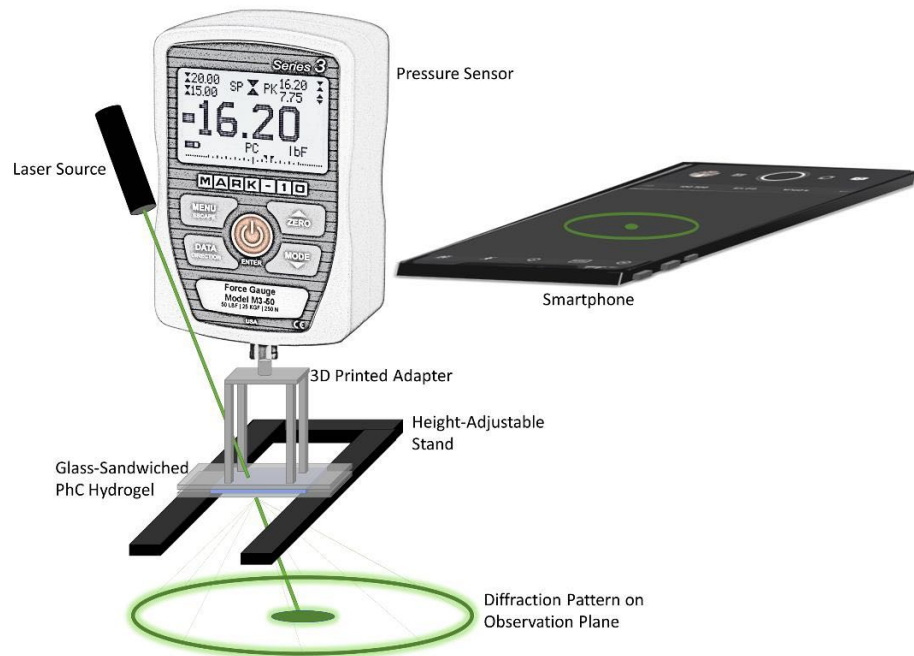
Figure 4.1 Physical Pressure Analysis Experimental Design. *To determine if physical pressure creates a measurable change in the diffraction pattern, a 3D-printed apparatus was developed which applies four points of equal pressure on the sandwiched PhC hydrogel. This apparatus is connected to a Mark-10 force gauge and the entire system can be raised or lowered on a vertical bar by a handwheel. Gentle adjustment of the handwheel compresses or relaxes the gel, with pressure displayed on the Mark-10 digital display. Throughout the process, a 532 nm laser generates a diffraction pattern below the apparatus. At distinct quantities of pressure, the diffraction pattern is imaged and later measured.*

Data Acquisition

Data acquisition occurred through incremental increases in pressure on the PhC hydrogel from 0 to 3 Newtons in approximately 0.4 Newton increments. Newtons of force was converted to kPa of pressure through measurement of the 2D surface area of the PhC hydrogel by which pressure was applied. This process was repeated three times to assess the pressure responsivity, which will be unique to the specific details of the fabrication process.

The image acquisition process was carried out using the same setup as in the previous chapter. A Xiaomi Redmi Note 7 smartphone was chosen as the tool for Debye ring characterization. While a smartphone is not as reliable for intensity characterization as a laboratory camera, it is sufficient for geometric measurements of Debye ring diameter. The smartphone collected the photographs using the FV-5 application, which allows fine control over image collection. This app was used to collect raw format, uncompressed camera data with automatic white balancing disabled. The following settings were used: F-stop: 1/8, ISO Speed: ISO-100, Exposure Time: 1/1000 seconds, Focal Length: 5 mm, Image Dimensions: 3000x4000, Bit Depth: 24. Images were loaded into Matlab and used to measure the Debye ring diameter through the same techniques as described in the previous chapter.

Ultrasonic Pressure Testing

To test the PhC hydrogel's capability to detect the presence of high-frequency ultrasound, the apparatus highlighted in Figure 4.2 was developed. Within a DI water filled clear acrylic container, a 3D printed apparatus was placed which mounts the PhC hydrogel, one of three possible ultrasonic transducers (Olympus, 2.25MHz/ V323-SM, 5

MHz/V310-SM, 10 MHz/V312-SM) and a glass reflector (a glass microscope slide). The glass reflector allows the laser source to directly transmit and strike the PhC hydrogel while also redirecting the vertical ultrasonic wave to a horizontal path which is directly on-axis with the laser source. This is a critical part of the experimental setup since the ultrasonic wavefront must be aligned with the target surface for the compression and rarefaction to be synchronized along the surface of the material. The ultrasonic transducer is driven by an ultrasound pulser board (Steval-ime009v1) with a programmable waveform. The laser light then exits the rear of the acrylic tank, generating a diffraction pattern on an observation screen behind. A photodetector [Thorlabs/PDA100A2] with an in-line amplifier was placed parallel to the observation plane and collects the resulting signal and routes it to an oscilloscope (Tektronix, TDS 2014B). The PDA100A2 as a silicone based optical amplifier is sensitive in the 400-1000 nm range with a low dark current.
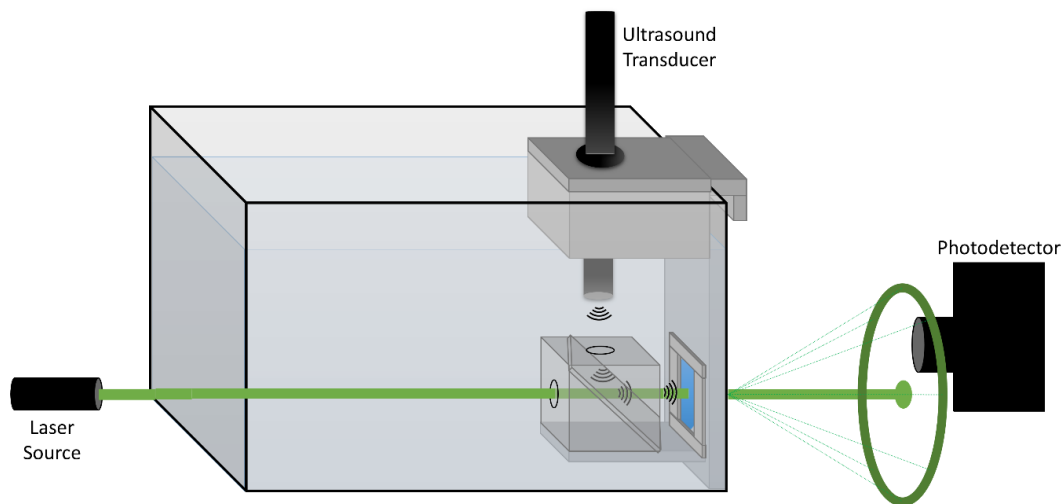
Figure 4.2 Ultrasound Pressure Analysis Experimental Design. The experimental ultrasound detection setup is designed to measure fluctuations in the laser intensity resulting from ultrasound interaction with the PhC hydrogel. 3D printed parts are used to ensure alignment of all optical and acoustic components, with the entire assembly placed within a clear acrylic container filled with DI water. A glass reflector is used to redirect ultrasonic waves to be aligned with the laser source. A photodetector detects the resulting intensity fluctuations.

Data Acquisition

To assess ultrasonic responsivity, a pressure sensitivity and a limit of detection analysis was performed on three photonic crystal hydrogel samples using three ultrasonic transducers with different central frequencies (2.25 MHz, 5 MHz, 10 MHz). Additionally, at each driving voltage for each transducer, a corresponding measurement was performed with a hydrophone placed at the same relative location to the transducer as the photonic crystal. The hydrophone measurement provides a scaling factor which can relate the amplitude of the ultrasonic wave to an absolute measurement of pressure in kPa. All measurements collected through the photodiode are routed to an oscilloscope

99

(Tektronix, TDS 2014B), which performs 128x averaging and then saves the resultant time-domain signal into a CSV file.

The first analysis – pressure sensitivity – was designed to measure the magnitude of the optical response at a variety of ultrasonic pressures. These pressures were generated by incrementing the transducer driving voltage from 0 Volts to 33 Volts in 3 Volt increments for each transducer. At each voltage level, each transducer generates five pulses at a frequency matching the central frequency of the corresponding transducer – either 2.25 MHz, 5 MHz or 10 MHz.

The second analysis – limit of detection – was designed to assess the minimum ultrasonic pressure which would generate an optical signal. To assess this, the driving voltage was gradually raised from 0 Volts until the oscilloscope began to display a signal. Once this is seen, the voltage was significantly reduced until it returned to the noise floor and then incrementally increased in 300 mV increments until a signal appears and then for a few more volts to ensure the limit of detection would be captured.

Data Analysis

To carry out pressure sensitivity and limit of detection analyses, the time domain signal was used and the waveform was converted to a single amplitude value using the maximum (peak) and minimum (trough) value of the signal. For signals generated by the hydrophone, the same technique was used, and the amplitude (Volts) was converted to pressure (kPa) using a corresponding calibration curve specific to the hydrophone. The amplitude of the optical signal at a specific combination of driving voltage and transducer was cross-referenced with the amplitude of the hydrophone signal to calculate the generated pressure on the photonic crystal at each combination of parameters. Assessing

pressure sensitivity requires plotting the magnitude of ultrasonic pressure against the amplitude of the optical signal generated. To provide additional validation that the signal from the PhC hydrogel was due to the ultrasonic transducer, frequency analysis of the detected optical signal was performed using a fast Fourier transform.

Calculation of the limit of detection was performed using the limit of quantitation criteria established by the Association of Analytical Communities (AOAC) which describes it calculation as the mean value of an expected zero value plus ten times the standard deviation of the zero value measurements [155][156]. The zero value was calculated by measuring the optical signal amplitude when the transducer power supply was reduced to zero volts.

Photodetector Placement Simulation

In the design of the previous experimental setup, the position of the photodetector on the observation screen is critical. The position of this photodetector should be at the location where the largest fluctuations are likely to occur in the diffraction pattern due to the ultrasound interaction with the PhC hydrogel. To determine the optimal location, a simulation was performed using the computational model described previously. A 25x25 hexagonal crystallite array was generated, each crystallite composing 10x10 particles – in total the simulated crystal encompassing approximately 500x500 µm. This crystal size was chosen as a balance between simulation execution time and parity to a potential experimental measurement. A high-resolution 2000x2000 pixel observation screen was simulated to maximize the spatial resolution of the simulated observation screen. This set of parameters was used to generate 5 unique diffraction patterns corresponding to 5 unique particle spacings (1.995, 1.999, 2.000, 2.001 and 2.005 µm). Spacings differ by

only a few nanometers in the simulation since the ultrasonic wave is not expected to generate a very significant positional offset during the compression-rarefaction cycle. These values were chosen based on a preliminary assessment of the expected change in particle spacing due to a 1 MPa applied pressure (collected from the hydrophone experimentally) and an expected bulk modulus of 42.8 Megapascals ([157]). This preliminary calculation generated an offset in particle spacing from 2 microns to 2.046 microns. Thus, particle offsets of only a few nanometers were chosen to ensure that results of the simulation would be scalable to an experimental scenario.

Each simulated diffraction pattern is analyzed using a simulated photodiode. The simulated photodiode is a square array of pixels on the diffraction pattern whose intensity is summed to predict the intensity of a photodiode at that location. This simulated photodiode is swept along the horizontal and vertical axes of the diffraction pattern to capture the intensity at various positions for a given particle spacing.   Comparison of the photodiode intensity profiles between the various particle spacings tested will reveal the photodiode placement which will create the most significant change in collected intensity caused by small changes in particle spacing.

Results

<u>PhC Physical Pressure Study</u>

A study of the impact of static physical pressure on the resulting diffraction pattern was performed as a preliminary assessment of the validity of pressure detection prior to the ultrasound study. The results of this assessment are shown in Figure 4.3

below. The debye ring diameter gradually decreased as the applied pressure was increased to 15 kPa. This provides preliminary evidence of the impact of mechanical waves on diffraction pattern.
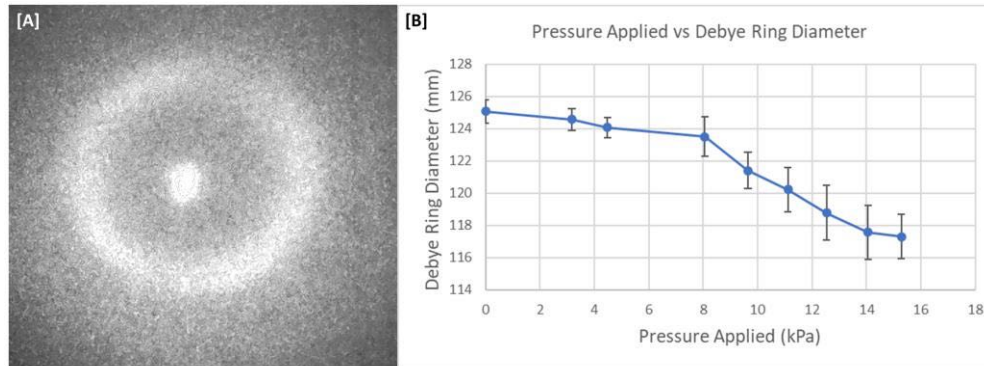
Figure 4.3 Results of Physical Pressure Study. *The static physical pressure study was designed to provide preliminary evidence that the ultrasound study could potentially modify the diffraction pattern. [A] A representative image of the diffraction pattern is shown. [B] The averaged results for four independent trials are shown, with error bars representing standard error. A Kruskal-Wallis test was executed to assess the significance of the effect of pressure across the various levels tested. The resultant p value, 0.0571, demonstrates significance at the $\alpha=0.1$ significance level and is nearly significant at the $\alpha=0.05$ significance level.*

Photodetector Placement Simulation

While the preliminary physical pressure study demonstrated diffraction pattern changes based on applied pressure, the ultrasound study required identification of where to put the small photodiode detector to maximize the detection of diffraction pattern changes due to ultrasound. To identify the optimal position, the computational model described in previous chapters was leveraged to create a corresponding simulation based on the expected compression induced volume changes described in the methods section. Additionally, the photodiode signal simulation from the previous chapter was used. Macroscopic defects but not microscopic defects were introduced in the simulated crystal since the random error introduced by microscopic defects may obscure the effect of the already very small spacing differences.

This simulation generated unique diffraction patterns which only differed based on the underlying particle spacing: 1.995, 1.999, 2.000, 2.001, 2.005 µm. The results of this simulation are provided below in Figure 4.4. These small differences in particle spacing create a very small, but measurable distance in the photodiode signal, as shown in 4D and 4E. The difference between the 1.995 and 2.005 µm is shown in 4F, with the laser spot size highlighted by a red box. The selection criteria for optimal location was the position which had the maximum intensity difference between the two spacings which is outside the spot size along the transmission axis. Surprisingly, the debye ring was not the ideal photodiode position – instead the optimal position was very close to the transmission axis. This spot was chosen for the subsequent ultrasound study. The intensity information from the model cannot be assumed to be completely accurate due to the lack of a multi-particle Mie scattering model – however it still provides a valuable assessment of relative intensity between these conditions.
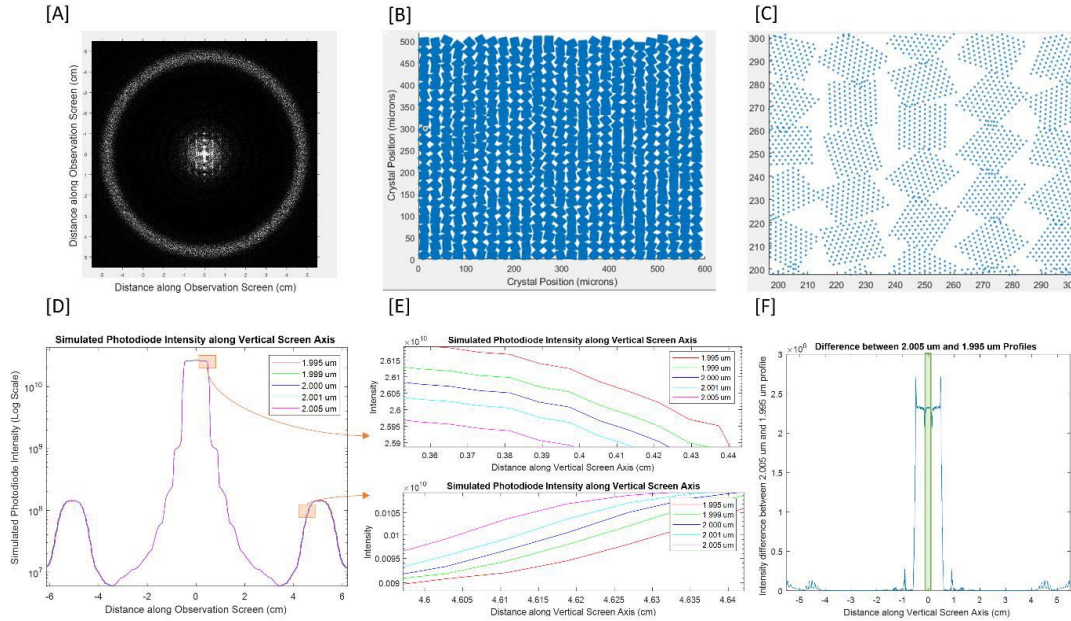
Figure 4.4 Simulation to Identify Ideal Photodiode Placement. The computational model and photodiode simulation both were utilized to identify an ideal photodiode placement. The simulation generated diffraction pattern [A] is created from a 25 x 25 crystallite polycrystal structure [B], with a zoomed image of microstructure shown in [C]. Five unique diffraction patterns were generated at unique particle spacings (1.995, 1.999, 2.000, 2.001, 2.005 μm) and the photodiode intensity simulator is used to assess the photodiode signal at discrete points in the image [D]. The small orange boxes located adjacent to the transmission axis and at the inner edge of the debye ring represents the regions used to create [E]. As expected, these nanometer-scale changes have no obvious visible effect in [D]. When zooming in closer, small changes in photodiode intensity become visible [E]. Comparing the y-scaling within the top image (adjacent region to transmission axis) and bottom image (inner edge of debye ring) of [E], the intensity changes are over 20x as significant next to the transmission axis as compared to the region around the Debye ring. After subtracting the 2.005 and 1.995 μm profiles, the most significant intensity fluctuations are validated as immediately adjacent to the transmission axis [F]. The green box represents the spot size along the transmission axis.

PhC Ultrasound Study

The PhC hydrogel ultrasound study began with validation that the optical signal generated by the ultrasound aligns with raw signal from the transducer and its pressure profile as measured with a hydrophone. As shown in Figure 4.5 below, representative data with a 2.25 MHz transducer shows clear alignment between the three signals. The time-domain pulse period as well as the frequency domain demonstrate the expected period of a 2.25 MHz pulse. The additional cycles found in the PhC hydrogel signal are likely due to its placement immediately adjacent to the wall of the experimental chamber,

where reflected ultrasound waves strike the PhC hydrogel after interacting with it and

striking the wall of the chamber.
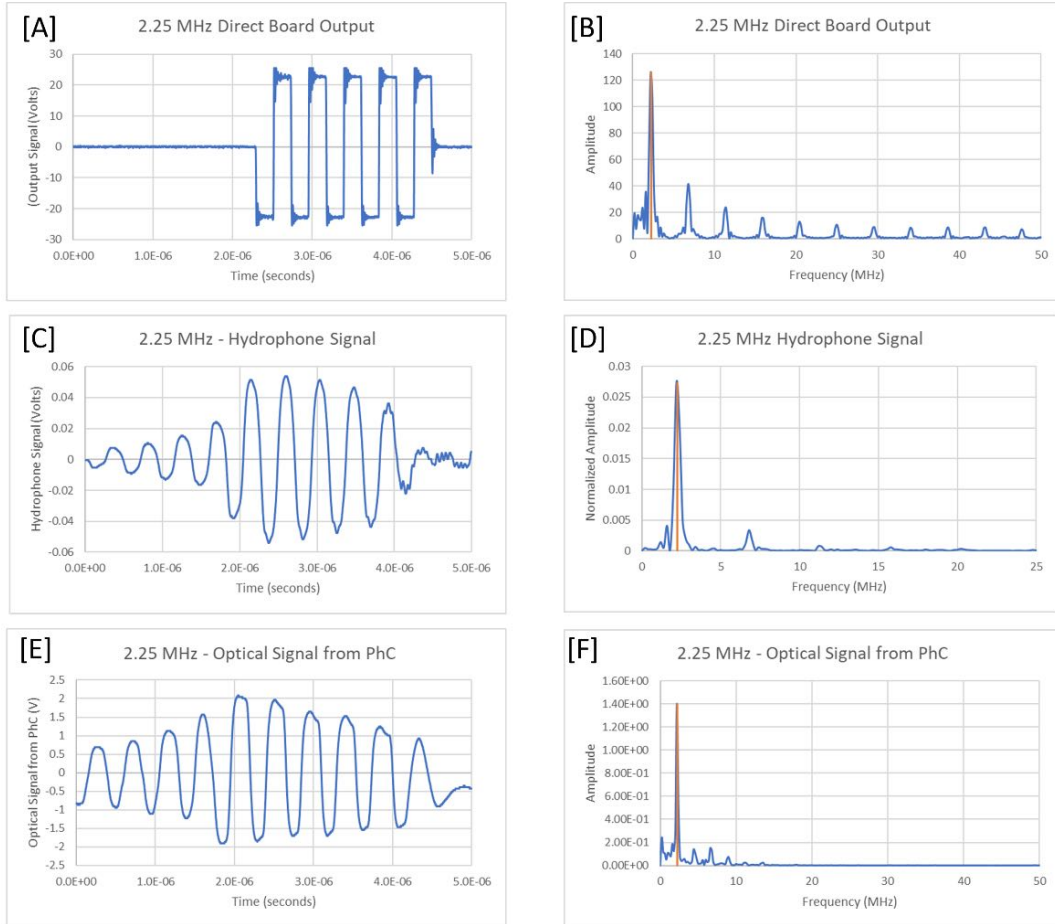
Figure 4.5 Representative Data of Ultrasound Signals. Representative data from the direct board output [A,B], a hydrophone signal captured from the transducer's output [C,D] and the PhC hydrogel optical signal [E,F] all demonstrate the expected time-domain period and frequency-domain peak. The red vertical line In the frequency domain represents a 2.25 MHz frequency. No window functions were applied to the FFT since its use is only to validate the peak frequency and no further quantitative analysis was performed using it.

Following validation, the next step of analysis was to characterize the pressure

responsivity of the PhC hydrogel at each of the three transducer frequencies available.

From 0 to 33 Volts in 3 volt increments, the transducer driving voltage was steadily

increased while the amplitude of the optical signal was monitored. The same procedure

was also carried out using a calibrated hydrophone to convert the transducer driving

voltage to pressure. The pressure responsivity of each transducer as well as the

hydrophone calibration curve is shown in Figure 4.6 below.
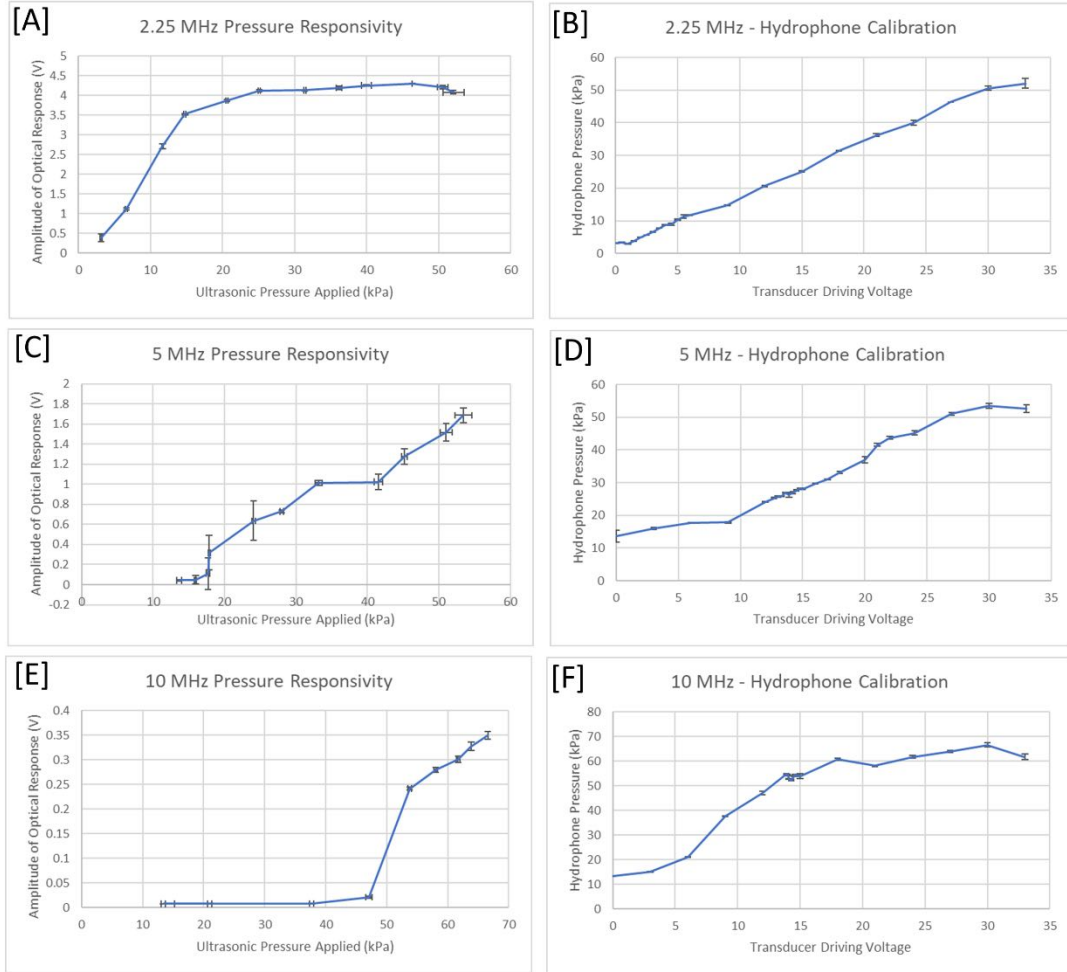
Figure 4.6 Pressure Responsivity of PhC Hydrogel. Pressure responsivity is shown for each of the three transducers (2.25 MHz, 5 MHz and 10 MHz) available at their corresponding central frequencies. Additionally, the hydrophone results were used to calibrate the transducer driving voltage to pressure conversion. Three unique PhC hydrogel samples were examined, and from each three repeated measurements were taken at each transducer driving voltage.

In addition to the individual gel responsivity, another valuable metric to consider

is the frequency bandwidth. This is demonstrated below in Figure 4.7, highlighting the

unique responsivity characteristics for each frequency. The 2.25 MHz responsivity has a

linear range within a much lower pressure than the other two frequencies but plateaued

afterwards. The 5 MHz responsivity curve generated a linear range that began

approximately when the one for 2.25 MHz ended and continued across all transducers

driving voltages tested. The 10 MHz responsivity curve began responding at higher

pressures than the other two frequencies and continued responding across all voltages

tested. Based on these results, it is evident that the bandwidth encompasses at a

minimum 2.25 MHz to 10 MHz.
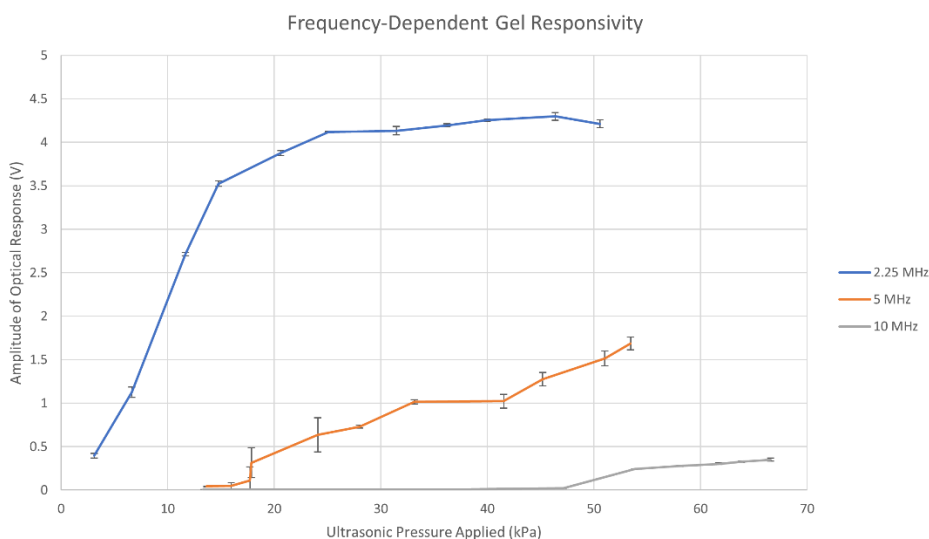
Figure 4.7 Frequency Bandwidth of PhC Hydrogel. Frequency bandwidth assessment of PhC hydrogel was tested with 2.25 MHz, 5 MHz and 10 MHz transducers. At 2.25 MHz a higher signal amplitude and a linear response towards the low-pressure range was seen. While at higher frequencies, such as at 5 MHz and 10 MHz, a lower signal amplitude but a linear response towards the higher pressures was observed.

A final assessment which was performed was the limit of detection (LOD), which

utilized a limit of quantitation criteria ($\bar{x}$ + 10 σ, where $\bar{x}$ = the mean signal at 0 Volt

transducer driving voltage and σ = the standard deviation of those signals) to identify the

smallest pressure which could be reliably detected as separate from the noise floor. As

shown in Figure 4.8 below, the LOD incrementally increased from 2.25 MHz (8.85 kPa)

to 5 MHz (25.58 kPa) and 10 MHz (54.17 kPa).
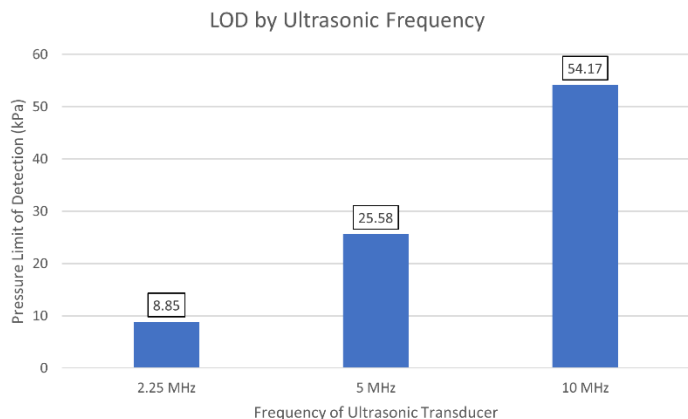
Figure 4.8 Limit of Ultrasound Pressure Detection of PhC Hydrogel. Limit of detection for each ultrasound transducer is shown, demonstrating a proportional relationship between ultrasound frequency and PhC hydrogel ultrasonic LOD.

Discussion & Conclusion

<u>Summary</u>

In this study, the sensitivity of the fabricated PhC hydrogel to physical and ultrasound pressure is investigated and the experimental design for the chamber used to characterize it is optimized. The PhC hydrogel physical pressure study demonstrated a clear reduction in debye ring diameter as incremental pressure was applied, matching theoretical expectations relating to the increase of particle spacing. The PhC hydrogel ultrasound study demonstrated sensitivity to all three transducers tested with a unique frequency bandwidth that favors low pressures at low frequencies and higher pressures at higher frequencies. In combination, these aspects demonstrate that the PhC hydrogel is pressure-sensitive to both physical and ultrasound pressure.

PhC Physical Pressure Study

The physical pressure study applied between 0 and 15 kPa of incrementally growing static pressure and demonstrated a clear gradual effect on debye ring thickness. While this approach was successful in generating a measurable difference in the diffraction pattern, the measured pressure applied cannot be directly compared to the ultrasound pressure measured later in the study due to the intrinsic difference between static and high-frequency pressure. Some of the core challenges of this study included the maintenance of hydration state which modifies the particle spacing over time. This challenge is mediated by carrying out the study rapidly and beginning the study when the PhC hydrogel is at full hydration.

PhC Ultrasound Study

At the outset of the photodetector placement study, it was assumed that the photodetector should be placed near the debye ring, either directly on the ring or immediately inside of the debye ring. If placed on the ring, it was believed that the modulation of the ring diameter would shift the energy the photodiode detects, generating a measurable signal. Experimentally, it was found that placement of the photodetector at the debye ring did provide a measurable ultrasonic signal – although it was extremely weak and therefore very difficult to locate. When shifting the photodetector to be next to the transmission axis, a far stronger optical signal was generated. These results demonstrated the value of the photodetector placement simulation in predicting the area of the diffraction pattern which exhibits the largest intensity fluctuations based on small changes in the particle spacing. Minimization of detector size also enhances detection sensitivity.

Assessment of the raw data generated by the pulser board, hydrophone and photodetector demonstrated a clear alignment between all three results. The square wave generated by the pulser board is well-reproduced in the time domain as it is transduced into a pressure wave by the ultrasound transducer, as measured by the hydrophone. Additionally, the optical signal measured based on the PhC hydrogel diffraction matches the hydrophone signal frequency, although additional cycles are present – likely due to reflections within the ultrasound chamber. Ringing artifacts were present in the pulser board time-domain signal, but were minimized through careful wire selection to match impedance between components. Assessment of the frequency spectra of the time-domain signals revealed that the central frequency of all three signals matches the input characteristics to the pulser board.

It is evident that there is a unique frequency-dependent response of the PhC material. Specifically, the lowest 2.25 MHz frequency had the smallest limit of detection but the narrowest linear response range while the limit of detection incrementally increased when moving to 5 MHz and 10 MHz. The results from this study suggest that 2.25 MHz is an ideal target for this PhC hydrogel if low pressures (below 20 kPa) are desired. If higher pressures are desired, higher frequencies should be used to ensure a linear responsivity.

Despite these promising results, several limitations must be considered. Since the maximum power supply voltage was limited, the maximum transducer driving voltage and thus ultrasonic pressure applied to the gel was limited. Furthermore, only three immersion ultrasonic transducers were available, limiting the ability to effectively characterize frequency bandwidth over a wider range. Finally, the limit of detection is

intrinsically dependent on the noise floor, which could have been lowered further if alternative instrumentation was used for the laser source and photodetector.

The underlying mechanism allowing ultrasound sensitivity may be either refractometric, interferometric, or a combination of the two. Refractometric influences emerge from the modulation of bulk refractive index due to oscillatory changes in the particle spacing. Interferometric influences emerge from changes in the generated diffraction pattern which form the debye ring pattern on the observation screen.

The majority of evidence in the scientific literature which examines the ultrasonic detection capabilities of photonic crystals utilize nanofabricated photonic crystal slabs, which are more geometrically complex and require significantly more advanced instrumentation than the technique described in this dissertation. One photonic crystal slab, fabricated using a periodic array of nanoholes etched into silicon oxide, was found to be responsive to ultrasound in the range of 2.5-8.5 MHz while a drum-effect photonic crystal slab platform was only sensitive at 5 MHz and with 1 MHz bandwidth [158]. These results appear to well align with the characteristics of our platform, although our assessment is limited since only three frequencies were tested. An additional PMMA overlayer has also been shown to improve sensitivity further[159]. Another research team similarly using periodic arrays of nanoholes on a silicon platform was able to achieve a more broadband response from 1-20 MHz with limits of detection of only a few kPa [160].

Conclusion and Future Work

These experiments demonstrate a successful proof-of-concept that the elastomeric PhC hydrogel platform is sensitive to ultrasonic pressure. The reporting of the unique linear

112

responsivity and minimum detectable pressure at multiple frequencies is not commonly reported in scientific literature will support other research teams in deciding whether this platform is applicable for their use case. Future work in this field should assess whether modifications to the PhC hydrogel structure can enhance sensitivity and bandwidth and allow for reflection mode detection and detection at the 1st order diffraction instead of the edge of the 0th order diffraction. Furthermore, the ultrasound source can be replaced with a pulsed laser source to assess whether the platform can utilize all-optical ultrasound. Despite the limitations of the platform, this chapter demonstrates a promising methodology for low-cost, low-complexity photonic crystal fabrication which exhibits a broad frequency response and a low limit of detection.

Chapter 5: Conclusion

Summary: Novelty & Impact

In Chapter 2, the outcomes of a novel computational model was provided which generated photonic crystal structures computationally and calculated the resulting diffraction pattern upon monochromatic illumination. This model was also validated against crystal structures with known analytical solutions. The photonic crystal particle position generation algorithm provided a novel approach to rapidly generating perfect crystals in varying crystal configurations and injecting microscopic or macroscopic error to generate polycrystalline structures. While other competing mathematical models exist in the scientific literature, the developed computational model is more accessible and able to process large quantities of particles rapidly on typical consumer hardware. Due to the flexibility of the simulation platform, research groups can efficiently use it to assist in the design of sensors which require known diffraction geometries.

In Chapter 3, the computational model is validated through generation of experimental photonic crystals and comparison of the computational model's output (based on microscopic particle position structure) and the experimental diffraction patterns generated. The fabrication techniques used were novel in not only the utility of fluorescent particles but also the micron-sized particles employed. This approach allowed particle position monitoring with conventional fluorescence microscopy instead of more destructive and conventional electron microscopy. Furthermore, the generation of a particle indexing approach to characterize the relative proportion of hexagonal versus 2D crystallite configurations allowed alignment between experimental, theoretical and simulated results.

In Chapter 4, the photonic crystal hydrogel was tested as an ultrasound sensor – which is expected due to its elastomeric structure and the resultant effect of ultrasonic waves on particle spacing. The platform was found to be sensitive to all three frequencies tested – 2.25, 5 and 10 MHz with a distinct responsivity and detection limit for each. These findings demonstrate the potential for using the proposed low-cost, simplistic fabrication as opposed to competing methodologies utilizing nanofabricated photonic crystal slabs.

Outcomes of Research Questions

Each of the research questions provided in the first chapter were resolved through the research conducted in this dissertation. From the first specific aim, the broad question posed was whether a computational model could be developed which combined diffraction and Mie theory to predict diffraction patterns of PhC hydrogels with configurable particle arrangements. This has been clearly resolved through the development and validation of the proposed computational model. Furthermore, the various sub-questions posed were also resolved, as the diffraction pattern was found to match analytical equations, published computational models and published experimental results as various experimental and crystal parameters were modified. The results of each of the hypotheses from the first specific aim are provided below.

- A PhC computational model can be built using diffraction and scattering theories.

  - Confirmed – Computational model was successfully created using diffraction and scattering theories.

- This computational model can predict diffraction patterns of PhCs with various 2D particle arrangements.

- o Confirmed – Computational model was used to generate various particle arrangements and defect characteristics.

- Simulated results from the computational model will match theoretical expectations resulting from varying particle configurations, particle spacing, illumination wavelengths, microscopic error and macroscopic error.

  - o Confirmed – Computational model was successfully validated, although accuracy is reduced as particle spacing grows.

From the second specific aim, the broad question provided asked whether fluorescent particles could be used during PhC hydrogel fabrication to facilitate nondestructive particle analysis during microscopy. This was resolved through the comparative analysis of experimental, computational and enhanced theoretical results which was only possible due to the particle position extraction enabled through fluorescent particle incorporation. Additionally, the indexing approach was validated, and despite its limitations was shown as a useful tool for improving existing analytical equations. The results of each of the hypotheses from the second specific aim are provided below.

- A 2D PhC can be composed of fluorescently-labeled particles while still retaining the optical properties of a traditional PhC, such as producing the Debye diffraction ring under laser illumination

  - o Confirmed – Fabricated PhC hydrogel formed Debye diffraction ring under monochromatic illumination

- A 2D PhC composed of fluorescently-labeled particles will allow monitoring of its configuration with fluorescence microscopy, a far more accessible and less expensive tool than conventional SEM.
  - Confirmed – Individual particles were visualized to support analysis of crystallite configurations and particle spacing.
- Fluorescence microscopy will allow the extraction of the unique position of each imaged particle, allowing for the PhC to be indexed based on its relative proportion of hexagonal vs 2D crystallites.
  - Confirmed – Individual particle locations were successfully extracted from fluorescence microscopy images and crystal structures indexed.
- The unique position of each imaged particle can serve as an input into the developed computational model to assess the degree to which an experimental debye ring's characteristics can be predicted using the computational model.
  - Confirmed – Individual particle positions were provided as input into computational model and the resulting diffraction pattern compared to experimental diffraction pattern.

From the final specific aim, the broad question posed asked whether the PhC hydrogel platform could provide ultrasound sensing. This capability has been clearly demonstrated using multiple transducers, each generating an optical fluctuation in the debye diffraction intensity corresponding to the ultrasound pressure and frequency. The additional questions provided, inquiring as to the frequency responsivity, sensitivity and limit of detection were all resolved through assessment over a wide range of ultrasound

pressures. The results of each of the hypotheses from the third specific aim are provided below.

- In response to ultrasonic pressure, the cyclic modulation of the effective refractive index due to alteration of particle spacing will create a measurable change in the intensity of optical diffraction, which can provide an ultrasound monitoring methodology.

  - Confirmed –Sinusoidal modulation was displayed by the optical signal when the ultrasound signal is generated.

- A PhC functioning as an ultrasound transducer will have a measurable frequency bandwidth, pressure sensitivity and limit of detection.

  - Confirmed – Frequency bandwidth, pressure sensitivity and limit of detection were all characterized.

- Incorporation of the computational model will allow prediction of the optimal photodetector location to capture the intensity fluctuations resulting from the ultrasonic wave.

  - Confirmed – Optimum photodiode positioning was successfully simulated using the computational model.

Future Work

While this dissertation demonstrates many enhancements, there are additional opportunities for improvements. For example, the computational simulation can be enhanced by considering the light polarization, the illumination beam vector, and the illumination beam diameter. Additional variables that can be considered include

temperature and chemical modifications. Furthermore, the simulation can be expanded to be more flexible in its characterization of multilayer particle arrays.

Experimental characterization of photonic crystals can also take advantage of many enhancements. The development of a sealed imaging chamber can reduce the gradual dehydration of the hydrated photonic crystal, allowing for longer imaging times. Furthermore, improvements in the fabrication method can reduce microscopic and macroscopic error, increasing the size of individual crystallites and minimizing defects. Finally, the particle indexing approach can be improved to better identify particles on crystallite boundaries – a typical source of error in indexing calculations.

This dissertation demonstrates that photonic crystal hydrogels can be utilized as ultrasound transducers. Furthermore, testing with multiple ultrasound transducers demonstrates a broad bandwidth across the entire range of frequencies tested – 2.25 to 10 MHz – with unique responsivities and limits of detection calculated at each. Thus, these results provide valuable insight into the potential of photonic crystal hydrogels as all-optical ultrasound platforms by leveraging their unique diffraction patterns to detect microscopic particle displacements.

Conclusion

PhCs are an exciting, nature-inspired biomimetic material that has many potential use cases in medical research. This dissertation provides an end-to-end analysis pipeline for their biomedical use, beginning with a computational simulation, validating the simulation through fabrication, and leveraging the simulation and fabrication to verify ultrasound biomedical applications. With additional refinement in fabrication and

characterization, this technology can prove instrumental in providing biosensing across

diverse disciplines.

References

[1]   T. Maka, D.N. Chigrin, S.G. Romanov, C.M. Sotomayor Torres, Three Dimensional Photonic Crystals in the Visible Regime, Prog. Electromagn. Res. PIER 41 (2003) 307–335. https://doi.org/10.2528/pier0201089e.

[2]   R.D. Meade, A.M. Rappe, K.D. Brommer, J.D. Joannopoulos, O.L. Alerhand, Accurate theoretical analysis of photonic band-gap materials, Phys. Rev. B. 48 (1993) 8434–8437. https://doi.org/10.1103/PhysRevB.48.8434.

[3]   S.A. Asher, J.M. Weissman, A. Tikhonov, R.D. Coalson, R. Kesavamoorthy, Diffraction in crystalline colloidal-array photonic crystals, Phys. Rev. E - Stat. Physics, Plasmas, Fluids, Relat. Interdiscip. Top. 69 (2004) 14. https://doi.org/10.1103/PhysRevE.69.066619.

[4]   L. Liu, P. Li, S.A. Asher, Fortuitously superimposed lattice plane secondary diffraction from crystalline colloidal arrays, J. Am. Chem. Soc. 119 (1997) 2729–2732. https://doi.org/10.1021/ja963885g.

[5]   E.M. Ahmed, Hydrogel: Preparation, characterization, and applications: A review, J. Adv. Res. 6 (2015) 105–121. https://doi.org/10.1016/j.jare.2013.07.006.

[6]   O. Guaresti, C. García–astrain, L. Urbina, A. Eceiza, N. Gabilondo, Reversible swelling behaviour of diels–alder clicked chitosan hydrogels in response to pH changes, Express Polym. Lett. 13 (2019) 27–36. https://doi.org/10.3144/expresspolymlett.2019.4.

[7]   R. V. Ulijn, N. Bibi, V. Jayawarna, P.D. Thornton, S.J. Todd, R.J. Mart, A.M. Smith, J.E. Gough, Bioresponsive hydrogels, Mater. Today. 10 (2007) 40–48. https://doi.org/10.1016/S1369-7021(07)70049-4.

[8]   J.E. Elliott, M. Macdonald, J. Nie, C.N. Bowman, Structure and swelling of poly(acrylic acid) hydrogels: effect of pH, ionic strength, and dilution on the crosslinked polymer structure, Polymer (Guildf). 45 (2004) 1503–1510. https://doi.org/10.1016/j.polymer.2003.12.040.

[9]   Z. Lei, Q. Wang, S. Sun, W. Zhu, P. Wu, A Bioinspired Mineral Hydrogel as a Self-Healable, Mechanically Adaptable Ionic Skin for Highly Sensitive Pressure Sensing, Adv. Mater. 29 (2017) 1700321. https://doi.org/10.1002/adma.201700321.

[10]   A.Z. Zardad, Y.E. Choonara, L.C. du Toit, P. Kumar, M. Mabrouk, P.P. Demarco Kondiah, V. Pillay, A review of thermo- and ultrasound-responsive polymeric systems for delivery of chemotherapeutic agents, Polymers (Basel). 8 (2016). https://doi.org/10.3390/polym8100359.

[11] C.-H. Wu, M.-K. Sun, J. Shieh, C.-S. Chen, C.-W. Huang, C.-A. Dai, S.-W. Chang, W.-S. Chen, T.-H. Young, Ultrasound-responsive NIPAM-based hydrogels with tunable profile of controlled release of large molecules, Ultrasonics. 83 (2018) 157–163. https://doi.org/10.1016/j.ultras.2017.03.019.

[12] L. Klouda, A.G. Mikos, Thermoresponsive hydrogels in biomedical applications, Eur. J. Pharm. Biopharm. 68 (2008) 34–45. https://doi.org/10.1016/j.ejpb.2007.02.025.

[13] Y. Dong, G. Jin, Y. Hong, H. Zhu, T.J. Lu, F. Xu, D. Bai, M. Lin, Engineering the Cell Microenvironment Using Novel Photoresponsive Hydrogels, ACS Appl. Mater. Interfaces. 10 (2018) 12374–12389. https://doi.org/10.1021/acsami.7b17751.

[14] S. Murdan, Electro-responsive drug delivery from hydrogels, J. Control. Release. 92 (2003) 1–17. https://doi.org/10.1016/S0168-3659(03)00303-1.

[15] E. Yablonovitch, Inhibited Spontaneous Emission in Solid-State Physics and Electronics, Phys. Rev. Lett. 58 (1987) 2059–2062. https://doi.org/10.1103/PhysRevLett.58.2059.

[16] S. John, Strong localization of photons in certain disordered dielectric superlattices, Phys. Rev. Lett. 58 (1987) 2486–2489. https://doi.org/10.1103/PhysRevLett.58.2486.

[17] E.S. Bol'shakov, A. V. Ivanov, A.A. Kozlov, S.D. Abdullaev, Photonic Crystal Sensors for Detecting Vapors of Benzene, Toluene, and o-Xylene, Russ. J. Phys. Chem. A. 92 (2018) 1530–1534. https://doi.org/10.1134/S0036024418080083.

[18] M.A. Haque, K. Mito, T. Kurokawa, T. Nakajima, T. Nonoyama, M. Ilyas, J.P. Gong, Tough and variable-band-gap photonic hydrogel displaying programmable angle-dependent colors, ACS Omega. 3 (2018) 55–62. https://doi.org/10.1021/acsomega.7b01443.

[19] G. Mayonado, S.M. Mian, V. Robbiano, F. Cacialli, Investigation Of The Bragg-Snell Law In Photonic Crystals, (2015) 60–63. https://doi.org/10.1119/bfy.2015.pr.015.

[20] X. Jia, K. Wang, J. Wang, Y. Hu, L. Shen, J. Zhu, Full-color photonic hydrogels for pH and ionic strength sensing, Eur. Polym. J. 83 (2016) 60–66. https://doi.org/10.1016/j.eurpolymj.2016.08.006.

[21] N.L. Smith, A. Coukouma, S. Dubnik, S.A. Asher, Debye ring diffraction elucidation of 2D photonic crystal self-assembly and ordering at the air–water

interface, Phys. Chem. Chem. Phys. 19 (2017) 31813–31822.
https://doi.org/10.1039/C7CP07130B.

[22] Y. Xu, B.Å.S. Gustafson, A generalized multiparticle Mie-solution: further experimental verification, J. Quant. Spectrosc. Radiat. Transf. 70 (2001) 395–419. https://doi.org/10.1016/S0022-4073(01)00019-X.

[23] M. V. Rybin, A.B. Khanikaev, M. Inoue, K.B. Samusev, M.J. Steel, G. Yushin, M.F. Limonov, Fano Resonance between Mie and Bragg Scattering in Photonic Crystals, Phys. Rev. Lett. 103 (2009) 1–4. https://doi.org/10.1103/PhysRevLett.103.023901.

[24] A. Tikhonov, Reflectivity enhanced two-dimensional dielectric particle array monolayer diffraction, J. Nanophotonics. 6 (2012) 063509. https://doi.org/10.1117/1.jnp.6.063509.

[25] L. Shang, W. Zhang, K. Xu, Y. Zhao, Bio-inspired intelligent structural color materials, Mater. Horizons. 6 (2019) 945–958. https://doi.org/10.1039/C9MH00101H.

[26] B.G. Prevo, O.D. Velev, Controlled, Rapid Deposition of Structured Coatings from Micro- and Nanoparticle Suspensions, Langmuir. 20 (2004) 2099–2107. https://doi.org/10.1021/la035295j.

[27] Y. Lan, M. Xue, L. Qiu, Z. Meng, Clinical Evaluation of a Photonic Crystal Sensor for Glucose Monitoring in Urine, ChemistrySelect. 4 (2019) 6547–6551. https://doi.org/10.1002/slct.201900840.

[28] F. Qi, Y. Lan, Z. Meng, C. Yan, S. Li, M. Xue, Y. Wang, L. Qiu, X. He, X. Liu, Acetylcholinesterase-functionalized two-dimensional photonic crystals for the detection of organophosphates, RSC Adv. 8 (2018) 29385–29391. https://doi.org/10.1039/c8ra04953j.

[29] G. Li, F. Xiao, S. Liao, Q. Chen, J. Zhou, Z. Wu, R. Yu, Label-free 2D colloidal photonic crystal hydrogel biosensor for urea and urease inhibitor, Sensors Actuators, B Chem. 277 (2018) 591–597. https://doi.org/10.1016/j.snb.2018.09.059.

[30] E. Tian, J. Wang, Y. Zheng, Y. Song, L. Jiang, D. Zhu, Colorful humidity sensitive photonic crystal hydrogel, J. Mater. Chem. 18 (2008) 1116. https://doi.org/10.1039/b717368g.

[31] Y. Dong, A. Bazrafshan, A. Pokutta, F. Sulejmani, W. Sun, J.D. Combs, K.C. Clarke, K. Salaita, Chameleon-Inspired Strain-Accommodating Smart Skin, ACS Nano. 13 (2019) 9918–9926. https://doi.org/10.1021/acsnano.9b04231.

[32] R. Xuan, Q. Wu, Y. Yin, J. Ge, Magnetically assembled photonic crystal film for humidity sensing, J. Mater. Chem. 21 (2011) 3672. https://doi.org/10.1039/c0jm03790g.

[33] L. Bai, Z. Xie, W. Wang, C. Yuan, Y. Zhao, Z. Mu, Q. Zhong, Z. Gu, Bio-Inspired Vapor-Responsive Colloidal Photonic Crystal Patterns by Inkjet Printing, ACS Nano. 8 (2014) 11094–11100. https://doi.org/10.1021/nn504659p.

[34] X. Hong, Y. Peng, J. Bai, B. Ning, Y. Liu, Z. Zhou, Z. Gao, A Novel Opal Closest-Packing Photonic Crystal for Naked-Eye Glucose Detection, Small. 10 (2014) 1308–1313. https://doi.org/10.1002/smll.201302788.

[35] Z.A. Zaky, A.M. Ahmed, A.S. Shalaby, A.H. Aly, Refractive index gas sensor based on the Tamm state in a one-dimensional photonic crystal: Theoretical optimisation, Sci. Rep. 10 (2020) 1–9. https://doi.org/10.1038/s41598-020-66427-6.

[36] B. Auguié, A. Bruchhausen, A. Fainstein, Critical coupling to Tamm plasmons, J. Opt. 17 (2015) 035003. https://doi.org/10.1088/2040-8978/17/3/035003.

[37] J.-G. Park, W. Benjamin Rogers, S. Magkiriadou, T. Kodger, S.-H. Kim, Y.-S. Kim, V.N. Manoharan, Photonic-crystal hydrogels with a rapidly tunable stop band and high reflectivity across the visible, Opt. Mater. Express. 7 (2017) 253. https://doi.org/10.1364/ome.7.000253.

[38] T. Li, X. Dong, C.C. Chan, K. Ni, S. Zhang, P.P. Shum, Humidity Sensor With a PVA-Coated Photonic Crystal Fiber Interferometer, IEEE Sens. J. 13 (2013) 2214–2216. https://doi.org/10.1109/JSEN.2012.2234100.

[39] D. Lopez-Torres, C. Elosua, J. Villatoro, J. Zubia, M. Rothhardt, K. Schuster, F.J. Arregui, Photonic crystal fiber interferometer coated with a PAH/PAA nanolayer as humidity sensor, Sensors Actuators B Chem. 242 (2017) 1065–1072. https://doi.org/10.1016/j.snb.2016.09.144.

[40] Y. Dou, J. Han, T. Wang, M. Wei, D.G. Evans, X. Duan, Fabrication of MMO–TiO2 one-dimensional photonic crystal and its application as a colorimetric sensor, J. Mater. Chem. 22 (2012) 14001. https://doi.org/10.1039/c2jm31560b.

[41] Y. Xu, Centrifugation and spin-coating method for fabrication of three-dimensional opal and inverse-opal structures as photonic crystal devices, J. Micro/Nanolithography, MEMS, MOEMS. 3 (2004) 168. https://doi.org/10.1117/1.1631005.

[42]   B. Van Duffel, R.H.A. Ras, F.C. De Schryver, R.A. Schoonheydt, Langmuir-Blodgett deposition and optical diffraction of two-dimensional opal, J. Mater. Chem. 11 (2001) 3333–3336. https://doi.org/10.1039/b102162l.

[43]   P. Massé, S. Reculusa, S. Ravaine, Elaboration of photonic crystal heterostructures by the Langmuir-Blodgett method, Colloids Surfaces A Physicochem. Eng. Asp. 284–285 (2006) 229–233. https://doi.org/10.1016/j.colsurfa.2005.12.035.

[44]   M. Parchine, J. McGrath, M. Bardosova, M.E. Pemble, Large Area 2D and 3D Colloidal Photonic Crystals Fabricated by a Roll-to-Roll Langmuir-Blodgett Method, Langmuir. 32 (2016) 5862–5869. https://doi.org/10.1021/acs.langmuir.6b01242.

[45]   J.R. Oh, J.H. Moon, S. Yoon, C.R. Park, Y.R. Do, Fabrication of wafer-scale polystyrene photonic crystal multilayers via the layer-by-layer scooping transfer technique, J. Mater. Chem. 21 (2011) 14167. https://doi.org/10.1039/c1jm11122a.

[46]   E. Armstrong, W. Khunsin, M. Osiak, M. Blömker, C.M.S. Torres, C. O'Dwyer, Ordered 2D colloidal photonic crystals on gold substrates by surfactant-assisted fast-rate dip coating, Small. 10 (2014) 1895–1901. https://doi.org/10.1002/smll.201303616.

[47]   Z. Cai, J.-T. Zhang, F. Xue, Z. Hong, D. Punihaole, S.A. Asher, 2D Photonic Crystal Protein Hydrogel Coulometer for Sensing Serum Albumin Ligand Binding, Anal. Chem. 86 (2014) 4840–4847. https://doi.org/10.1021/ac404134t.

[48]   G.T.H. Tran, M. Koike, T. Uchikoshi, H. Fudouzi, Fabrication of polystyrene colloidal crystal film by electrophoretic deposition, Adv. Powder Technol. (2020). https://doi.org/10.1016/j.apt.2020.05.029.

[49]   K. Katagiri, Y. Tanaka, K. Uemura, K. Inumaru, T. Seki, Y. Takeoka, Structural color coating films composed of an amorphous array of colloidal particles via electrophoretic deposition, NPG Asia Mater. 9 (2017) e355–e355. https://doi.org/10.1038/am.2017.13.

[50]   J. Ge, Y. Hu, Y. Yin, Highly Tunable Superparamagnetic Colloidal Photonic Crystals, Angew. Chemie Int. Ed. 46 (2007) 7428–7431. https://doi.org/10.1002/anie.200701992.

[51]   A. You, Y. Cao, G. Cao, Facile fabrication of a magnetically assembled colloidal photonic crystal film via radical polymerization, RSC Adv. 5 (2015) 93945–93950. https://doi.org/10.1039/C5RA13900G.

[52] W. Shen, M. Li, C. Ye, L. Jiang, Y. Song, Direct-writing colloidal photonic crystal microfluidic chips by inkjet printing for label-free protein detection, Lab Chip. 12 (2012) 3089. https://doi.org/10.1039/c2lc40311k.

[53] Y. Zhao, Z. Xie, H. Gu, L. Jin, X. Zhao, B. Wang, Z. Gu, Multifunctional photonic crystal barcodes from microfluidics, NPG Asia Mater. 4 (2012) e25–e25. https://doi.org/10.1038/am.2012.46.

[54] M.C. Fuertes, F.J. López-Alcaraz, M.C. Marchi, H.E. Troiani, V. Luca, H. Míguez, G.J.D.A.A. Soler-Illia, Photonic crystals from ordered mesoporous thin-film functional building blocks, Adv. Funct. Mater. 17 (2007) 1247–1254. https://doi.org/10.1002/adfm.200601190.

[55] G. von Freymann, V. Kitaev, B. V. Lotsch, G.A. Ozin, Bottom-up assembly of photonic crystals, Chem. Soc. Rev. 42 (2013) 2528–2554. https://doi.org/10.1039/c2cs35309a.

[56] B. V. Lotsch, C.B. Knobbe, G.A. Ozin, A step towards optically encoded silver release in 1D photonic crystals, Small. 5 (2009) 1498–1503. https://doi.org/10.1002/smll.200801925.

[57] I. Pavlichenko, A.T. Exner, M. Guehl, P. Lugli, G. Scarpa, B. V. Lotsch, Humidity-Enhanced Thermally Tunable TiO_2/SiO_2 Bragg Stacks, J. Phys. Chem. C. 116 (2012) 298–305. https://doi.org/10.1021/jp208733t.

[58] B. V. Lotsch, F. Scotognella, K. Moeller, T. Bein, G.A. Ozin, Stimuli-responsive Bragg stacks for chemo-optical sensing applications, Photonic Cryst. Mater. Devices IX. 7713 (2010) 77130V. https://doi.org/10.1117/12.854703.

[59] L. Wang, S. Zhang, J.L. Lutkenhaus, L. Chu, B. Tang, S. Li, W. Ma, All nanoparticle-based P(MMA–AA)/TiO_2 one-dimensional photonic crystal films with tunable structural colors, J. Mater. Chem. C. 5 (2017) 8266–8272. https://doi.org/10.1039/C7TC02166F.

[60] Z. Wang, J. Zhang, J. Li, J. Xie, Y. Li, S. Liang, Z. Tian, C. Li, Z. Wang, T. Wang, H. Zhang, B. Yang, Colorful detection of organic solvents based on responsive organic/inorganic hybrid one-dimensional photonic crystals, J. Mater. Chem. 21 (2011) 1264–1270. https://doi.org/10.1039/C0JM02655G.

[61] M.C. Chiappelli, R.C. Hayward, Photonic multilayer sensors from photo-crosslinkable polymer films, Adv. Mater. 24 (2012) 6100–6104. https://doi.org/10.1002/adma.201202459.

[62] L.D. Bonifacio, B. V. Lotsch, D.P. Puzzo, F. Scotognella, G.A. Ozin, Stacking the nanochemistry deck: Structural And compositional diversity in one-dimensional photonic crystals, Adv. Mater. 21 (2009) 1641–1646. https://doi.org/10.1002/adma.200802348.

[63] W. Fan, M. Chen, S. Yang, L. Wu, Centrifugation-assisted Assembly of Colloidal Silica into Crack-Free and Transferrable Films with Tunable Crystalline Structures, Sci. Rep. 5 (2015) 1–10. https://doi.org/10.1038/srep12100.

[64] A.E. Coukouma, N.L. Smith, S.A. Asher, Removable interpenetrating network enables highly-responsive 2-D photonic crystal hydrogel sensors, Analyst. 140 (2015) 6517–6521. https://doi.org/10.1039/C5AN01204J.

[65] W. Tang, C. Chen, Hydrogel-based colloidal photonic crystal devices for glucose sensing, Polymers (Basel). 12 (2020) 1–18. https://doi.org/10.3390/polym12030625.

[66] Q. Li, U. Jonas, X.S. Zhao, M. Kappl, The forces at work in colloidal self-assembly: a review on fundamental interactions between colloidal particles, Asia-Pacific J. Chem. Eng. 3 (2008) 255–268. https://doi.org/10.1002/apj.144.

[67] L. V. Woodcock, Entropy difference between the face-centred cubic and hexagonal close-packed crystal structures, Nature. 385 (1997) 141–143. https://doi.org/10.1038/385141a0.

[68] Z. Mu, X. Zhao, Y. Huang, M. Lu, Z. Gu, Photonic Crystal Hydrogel Enhanced Plasmonic Staining for Multiplexed Protein Analysis, Small. 11 (2015) 6036–6043. https://doi.org/10.1002/smll.201501829.

[69] N.L. Smith, Z. Hong, S.A. Asher, Responsive ionic liquid-polymer 2D photonic crystal gas sensors, Analyst. 139 (2014) 6379–6386. https://doi.org/10.1039/c4an01485e.

[70] W. Lu, S.A. Asher, Z. Meng, Z. Yan, M. Xue, L. Qiu, D. Yi, Visual detection of 2,4,6-trinitrotolune by molecularly imprinted colloidal array photonic crystal, J. Hazard. Mater. 316 (2016) 87–93. https://doi.org/10.1016/j.jhazmat.2016.05.022.

[71] J.T. Zhang, X. Chao, X. Liu, S.A. Asher, Two-dimensional array debye ring diffraction protein recognition sensing, Chem. Commun. 49 (2013) 6337–6339. https://doi.org/10.1039/c3cc43396j.

[72] Z. Cai, D.H. Kwak, D. Punihaole, Z. Hong, S.S. Velankar, X. Liu, S.A. Asher, A Photonic Crystal Protein Hydrogel Sensor for Candida albicans, Angew. Chemie - Int. Ed. 54 (2015) 13036–13040. https://doi.org/10.1002/anie.201506205.

[73]   Z. Cai, A. Sasmal, X. Liu, S.A. Asher, Responsive Photonic Crystal Carbohydrate Hydrogel Sensor Materials for Selective and Sensitive Lectin Protein Detection, ACS Sensors. 2 (2017) 1474–1481. https://doi.org/10.1021/acssensors.7b00426.

[74]   M.M. Ward Muscatello, L.E. Stunja, S.A. Asher, Polymerized crystalline colloidal array sensing of high glucose concentrations, Anal. Chem. 81 (2009) 4978–4986. https://doi.org/10.1021/ac900006x.

[75]   C. Chen, Z.-Q. Dong, J.-H. Shen, H.-W. Chen, Y.-H. Zhu, Z.-G. Zhu, 2D Photonic Crystal Hydrogel Sensor for Tear Glucose Monitoring, ACS Omega. 3 (2018) 3211–3217. https://doi.org/10.1021/acsomega.7b02046.

[76]   K. Lee, S.A. Asher, Photonic crystal chemical sensors: pH and ionic strength, J. Am. Chem. Soc. 122 (2000) 9534–9537. https://doi.org/10.1021/ja002017n.

[77]   X. Xu, A. V. Goponenko, S.A. Asher, Polymerized polyHEMA photonic crystals: pH and ethanol sensor materials, J. Am. Chem. Soc. 130 (2008) 3113–3119. https://doi.org/10.1021/ja077979+.

[78]   J.P. Walker, K.W. Kimble, S.A. Asher, Photonic crystal sensor for organophosphate nerve agents utilizing the organophosphorus hydrolase enzyme, Anal. Bioanal. Chem. 389 (2007) 2115–2124. https://doi.org/10.1007/s00216-007-1599-y.

[79]   F. Yan, S. Asher, Cation identity dependence of crown ether photonic crystal Pb2+ sensing, Anal. Bioanal. Chem. 387 (2007) 2121–2130. https://doi.org/10.1007/s00216-006-1088-8.

[80]   Z. Yan, M. Xue, Q. He, W. Lu, Z. Meng, D. Yan, L. Qiu, L. Zhou, Y. Yu, A non-enzymatic urine glucose sensor with 2-D photonic crystal hydrogel, Anal. Bioanal. Chem. 408 (2016) 8317–8323. https://doi.org/10.1007/s00216-016-9947-4.

[81]   A.K. Yetisen, Y. Montelongo, F. Da Cruz Vasconcellos, J.L. Martinez-Hurtado, S. Neupane, H. Butt, M.M. Qasim, J. Blyth, K. Burling, J.B. Carmody, M. Evans, T.D. Wilkinson, L.T. Kubota, M.J. Monteiro, C.R. Lowe, Reusable, robust, and accurate laser-generated photonic nanosensor, Nano Lett. 14 (2014) 3587–3593. https://doi.org/10.1021/nl5012504.

[82]   M.R. Lee, P.M. Fauchet, Two-dimensional silicon photonic crystal based biosensing platform for protein detection, Opt. Express. 15 (2007) 4530. https://doi.org/10.1364/oe.15.004530.

[83]   G. Deng, K. Xu, Y. Sun, Y. Chen, T. Zheng, J. Li, High sensitive immunoassay for multiplex mycotoxin detection with photonic crystal microsphere suspension array, Anal. Chem. 85 (2013) 2833–2840. https://doi.org/10.1021/ac3033728.

[84] A.M.R. Pinto, M. Lopez-Amo, Photonic Crystal Fibers for Sensing Applications, J. Sensors. 2012 (2012) 1–21. https://doi.org/10.1155/2012/598178.

[85] H.Y. Fu, S.K. Khijwania, H.Y. Tam, P.K.A. Wai, C. Lu, Polarization-maintaining photonic-crystal-fiber-based all-optical polarimetric torsion sensor, Appl. Opt. 49 (2010) 5954. https://doi.org/10.1364/AO.49.005954.

[86] H.-M. Kim, T.-H. Kim, B. Kim, Y. Chung, Temperature-Insensitive Torsion Sensor With Enhanced Sensitivity by Use of a Highly Birefringent Photonic Crystal Fiber, IEEE Photonics Technol. Lett. 22 (2010) 1539–1541. https://doi.org/10.1109/LPT.2010.2068043.

[87] C. Jewart, K.P. Chen, B. McMillen, M.M. Bails, S.P. Levitan, J. Canning, I. V. Avdeev, Sensitivity enhancement of fiber Bragg gratings to transverse stress by using microstructural fibers, Opt. Lett. 31 (2006) 2260. https://doi.org/10.1364/OL.31.002260.

[88] T. Geernaert, G. Luyckx, E. Voet, T. Nasilowski, K. Chah, M. Becker, H. Bartelt, W. Urbanczyk, J. Wojcik, W. De Waele, J. Degrieck, H. Terryn, F. Berghmans, H. Thienpont, Transversal Load Sensing With Fiber Bragg Gratings in Microstructured Optical Fibers, IEEE Photonics Technol. Lett. 21 (2009) 6–8. https://doi.org/10.1109/LPT.2008.2007915.

[89] H. V. Thakur, S.M. Nalawade, Y. Saxena, K.T.V. Grattan, All-fiber embedded PM-PCF vibration sensor for Structural Health Monitoring of composite, Sensors Actuators, A Phys. 167 (2011) 204–212. https://doi.org/10.1016/j.sna.2011.02.008.

[90] G. Rajan, M. Ramakrishnan, Y. Semenova, A. Domanski, A. Boczkowska, T. Wolinski, G. Farrell, Analysis of vibration measurements in a composite material using an embedded PM-PCF polarimetric sensor and an FBG sensor, IEEE Sens. J. 12 (2012) 1365–1371. https://doi.org/10.1109/JSEN.2011.2172412.

[91] S. Hadzialic, S. Kim, A.F. Sarioglu, A.S. Sudbo, O. Solgaard, Displacement Sensing With a Mechanically Tunable Photonic Crystal, IEEE Photonics Technol. Lett. 22 (2010) 1196–1198. https://doi.org/10.1109/LPT.2010.2050584.

[92] C. Lee, J. Thillaigovindan, Optical nanomechanical sensor using a silicon photonic crystal cantilever embedded with a nanocavity resonator, Appl. Opt. 48 (2009) 1797. https://doi.org/10.1364/AO.48.001797.

[93] B.T. Tung, D.V. Dao, T. Ikeda, Y. Kanamori, K. Hane, S. Sugiyama, Investigation of strain sensing effect in modified single-defect photonic crystal nanocavity, Opt. Express. 19 (2011) 8821. https://doi.org/10.1364/OE.19.008821.

[94] Y. Zhang, Y. Zhao, Q. Wang, Measurement of methane concentration with cryptophane E infiltrated photonic crystal microcavity, Sensors Actuators B Chem. 209 (2015) 431–437. https://doi.org/10.1016/j.snb.2014.12.002.

[95] H. Xu, P. Wu, C. Zhu, A. Elbaz, Z.Z. Gu, Photonic crystal for gas sensing, J. Mater. Chem. C. 1 (2013) 6087. https://doi.org/10.1039/c3tc30722k.

[96] Z. Wang, C.T. Chan, W. Zhang, N. Ming, P. Sheng, Three-dimensional self-assembly of metal nanoparticles: Possible photonic crystal with a complete gap below the plasma frequency, Phys. Rev. B. 64 (2001) 113108. https://doi.org/10.1103/PhysRevB.64.113108.

[97] S. Lin, W. Zhu, Y. Jin, K.B. Crozier, Surface-Enhanced Raman Scattering with Ag Nanoparticles Optically Trapped by a Photonic Crystal Cavity, Nano Lett. 13 (2013) 559–563. https://doi.org/10.1021/nl304069n.

[98] W. Zhao, X. Li, S. Gao, Y. Feng, J. Huang, Understanding mechanical characteristics of cellulose nanocrystals reinforced PHEMA nanocomposite hydrogel: in aqueous cyclic test, Cellulose. 24 (2017) 2095–2110. https://doi.org/10.1007/s10570-017-1244-7.

[99] J.H. Lim, K.S. Lee, J.C. Kim, B.H. Lee, Tunable fiber gratings fabricated in photonic crystal fiber by use of mechanical pressure, Opt. Lett. 29 (2004) 331. https://doi.org/10.1364/ol.29.000331.

[100] C. Wu, H.Y. Fu, K.K. Qureshi, B.-O. Guan, H.Y. Tam, High-pressure and high-temperature characteristics of a Fabry–Perot interferometer based on photonic crystal fiber, Opt. Lett. 36 (2011) 412. https://doi.org/10.1364/ol.36.000412.

[101] H.Y. Fu, H.Y. Tam, L.Y. Shao, X. Dong, P.K.A. Wai, C. Lu, S.K. Khijwania, Pressure sensor realized with polarization-maintaining photonic crystal fiber-based Sagnac interferometer, Appl. Opt. 47 (2008) 2835–2839. https://doi.org/10.1364/AO.47.002835.

[102] Pressure Sensor, RS Components Pty Ltd. (n.d.).

[103] Y.J. Yoo, W. Kim, J.H. Ko, Y.J. Kim, Y. Lee, S.G. Stanciu, J. Lee, S. Kim, J. Oh, Y.M. Song, Large-Area Virus Coated Ultrathin Colorimetric Sensors with a Highly Lossy Resonant Promoter for Enhanced Chromaticity, Adv. Sci. (2020) 2000978. https://doi.org/10.1002/advs.202000978.

[104] H.R. Lin, S.H. Wang, C.C. Chiang, Y.C. Juang, F.A. Yu, L. Tsai, High strain-rate response of injectable PAA hydrogel, J. Biomater. Sci. Polym. Ed. 26 (2015) 534–544. https://doi.org/10.1080/09205063.2015.1034598.

[105] A. Chiappini, L.T.N. Tran, P.M. Trejo-García, L. Zur, A. Lukowiak, M. Ferrari, G.C. Righini, Photonic Crystal Stimuli-Responsive Chromatic Sensors: A Short Review, Micromachines. 11 (2020) 290. https://doi.org/10.3390/mi11030290.

[106] P. Urone, R. Hinrichs, eds., Waves and their properties, in: Physics (College. Park. Md)., 1st ed., OpenStax, Houston, 2020: pp. 389–406. https://doi.org/10.32388/ZLFLKB.

[107] S. Ling, J. Sanny, B. Moebs, eds., Energy Carried by Electromagnetic Waves, in: Univ. Phys., 1st ed., OpenStax CNX, California, 2020.

[108] W. Bragg, R. James, H. Lipson, The Crystalline State, Macmillan, New York, 1934.

[109] W. Hergert, T. Wriedt, eds., The Mie Theory: Basics and Applications, Springer Berlin Heidelberg, Berlin, Heidelberg, 2012. https://doi.org/10.1007/978-3-642-28738-1.

[110] T. Wriedt, Mie Theory: A Review, in: Springer Ser. Opt. Sci., 2012: pp. 53–71. https://doi.org/10.1007/978-3-642-28738-1_2.

[111] A. Egel, L. Pattelli, G. Mazzamuto, D.S. Wiersma, U. Lemmer, CELES: CUDA-accelerated simulation of electromagnetic scattering by large ensembles of spheres, J. Quant. Spectrosc. Radiat. Transf. 199 (2017) 103–110. https://doi.org/10.1016/j.jqsrt.2017.05.010.

[112] S. Berisha, T. van Dijk, R. Bhargava, P.S. Carney, D. Mayerich, BIM-Sim: Interactive Simulation of Broadband Imaging Using Mie Theory, Front. Phys. 5 (2017). https://doi.org/10.3389/fphy.2017.00005.

[113] S. Prahl, Mie Scattering Calculator, OMLC. (n.d.). https://omlc.org/calc/mie_calc.html.

[114] T. Tsutaoka, T. Tokunaga, T. Umeda, T. Maehara, Observation of the two-dimensional reciprocal lattice by use of lattice grating sheets and a laser pointer, Eur. J. Phys. 35 (2014) 055021. https://doi.org/10.1088/0143-0807/35/5/055021.

[115] J.M. Luque-Raigón, Angular optical behavior of photonic-crystal-based dye-sensitized solar cells, J. Photonics Energy. 9 (2019) 1. https://doi.org/10.1117/1.JPE.9.025501.

[116] R. Li, L. Li, B. Wang, L. Yu, Preparation of Quantum Dot-Embedded Photonic Crystal Hydrogel and Its Application as Fluorescence Sensor for the Detection of Nitrite, Nanomaterials. 11 (2021) 3126. https://doi.org/10.3390/nano11113126.

[117] Z. Yu, L. Chen, S. Chen, Uniform fluorescent photonic crystal supraballs generated from nanocrystal-loaded hydrogel microspheres, J. Mater. Chem. 20 (2010) 6182. https://doi.org/10.1039/c0jm00400f.

[118] V.-P. Dinh, D.-K. Nguyen, Q.-H. Nguyen, T.-T. Luu, T.H.Y. Pham, T.T.H. Vu, H.-S. Chuang, H.-P. Pham, Fabrication of SiO2/PEGDA Inverse Opal Photonic Crystal with Fluorescence Enhancement Effects, J. Anal. Methods Chem. 2021 (2021) 1–7. https://doi.org/10.1155/2021/6613154.

[119] T. Fujishima, H.T. Miyazaki, H. Miyazaki, Y. Jimba, T. Kasaya, K. Sakoda, Y. Ogawa, F. Minami, Light propagation from a fluorescent particle embedded in a photonic cluster of micrometer-sized dielectric spheres, Opt. Express. 16 (2008) 20706. https://doi.org/10.1364/OE.16.020706.

[120] F. Xue, Z. Meng, F. Wang, Q. Wang, M. Xue, Z. Xu, A 2-D photonic crystal hydrogel for selective sensing of glucose, J. Mater. Chem. A. 2 (2014) 9559–9565. https://doi.org/10.1039/C4TA01031K.

[121] F. Xue, Z. Meng, F. Qi, M. Xue, F. Wang, W. Chen, Z. Yan, Two-dimensional inverse opal hydrogel for pH sensing, Analyst. 139 (2014) 6192–6196. https://doi.org/10.1039/C4AN00939H.

[122] N. Liu, Z. Zheng, D. Yu, W. Hong, H. Liu, X. Chen, Programmable Invisible Photonic Patterns with Rapid Response Based on Two-Dimensional Colloidal Crystals, Polymers (Basel). 13 (2021) 1926. https://doi.org/10.3390/polym13121926.

[123] J.C. Crocker, D.G. Grier, Methods of Digital Video Microscopy for Colloidal Studies, J. Colloid Interface Sci. 179 (1996) 298–310. https://doi.org/10.1006/jcis.1996.0217.

[124] G. Milne, Y. Zhao, D.T. Chiu, High-Precision Measurement and Analysis of Colloidal Monolayers, Anal. Chem. 82 (2010) 3943–3949. https://doi.org/10.1021/ac902722d.

[125] U. Gasser, B. Zhou, Accurate detection of spherical objects in a complex background, Opt. Express. 29 (2021) 37048. https://doi.org/10.1364/OE.434652.

[126] H. Yücel, S.K.P. Velu, Toolbox for tracking and analyzing crowded mixture of colloidal particles, Colloid Interface Sci. Commun. 45 (2021) 100546. https://doi.org/10.1016/j.colcom.2021.100546.

[127] V. Lotito, T. Zambelli, Approaches to self-assembly of colloidal monolayers: A guide for nanotechnologists, Adv. Colloid Interface Sci. 246 (2017) 217–274. https://doi.org/10.1016/j.cis.2017.04.003.

[128] V. Lotito, T. Zambelli, Pattern Formation in Binary Colloidal Assemblies: Hidden Symmetries in a Kaleidoscope of Structures, Langmuir. 34 (2018) 7827–7843. https://doi.org/10.1021/acs.langmuir.8b01411.

[129] V. Lotito, T. Zambelli, Pattern detection in colloidal assembly: A mosaic of analysis techniques, Adv. Colloid Interface Sci. 284 (2020) 102252. https://doi.org/10.1016/j.cis.2020.102252.

[130] C.C. Cheng, Fabrication of photonic band-gap crystals, J. Vac. Sci. Technol. B Microelectron. Nanom. Struct. 13 (1995) 2696. https://doi.org/10.1116/1.588051.

[131] H. Muri, L. Hoang, D. Hjelme, Mapping Nanoparticles in Hydrogels: A Comparison of Preparation Methods for Electron Microscopy, Appl. Sci. 8 (2018) 2446. https://doi.org/10.3390/app8122446.

[132] M. Obana, B.R. Silverman, D.A. Tirrell, Protein-Mediated Colloidal Assembly, J. Am. Chem. Soc. 139 (2017) 14251–14256. https://doi.org/10.1021/jacs.7b07798.

[133] R. van Dommelen, P. Fanzio, L. Sasso, Surface self-assembly of colloidal crystals for micro- and nano-patterning, Adv. Colloid Interface Sci. 251 (2018) 97–114. https://doi.org/10.1016/j.cis.2017.10.007.

[134] T. Martynkien, M. Szpulak, G. Statkiewicz, G. Golojuch, J. Olszewski, W. Urbanczyk, J. Wojcik, P. Mergo, M. Makara, T. Nasilowski, F. Berghmans, H. Thienpont, Measurements of sensitivity to hydrostatic pressure and temperature in highly birefringent photonic crystal fibers, Opt. Quantum Electron. 39 (2007) 481–489. https://doi.org/10.1007/s11082-007-9084-6.

[135] S. Olyaee, A.A. Dehghani, Nano-pressure sensor using high quality photonic crystal cavity resonator, in: 2012 8th Int. Symp. Commun. Syst. Networks Digit. Signal Process., IEEE, 2012: pp. 1–4. https://doi.org/10.1109/CSNDSP.2012.6292729.

[136] J. Sabarinathan, A. Bakhtazad, B. Poulsen, M. Zylstra, Photonic crystal thin-film micro-pressure sensors, J. Phys. Conf. Ser. 619 (2015) 012020. https://doi.org/10.1088/1742-6596/619/1/012020.

[137] T.L. Szabo, P.A. Lewin, Ultrasound Transducer Selection in Clinical Imaging Practice, J. Ultrasound Med. 32 (2013) 573–582. https://doi.org/10.7863/jum.2013.32.4.573.

[138] R. Manwar, K. Kratkiewicz, K. Avanaki, Overview of Ultrasound Detection Technologies for Photoacoustic Imaging, Micromachines. 11 (2020) 692. https://doi.org/10.3390/mi11070692.

[139] S. V. Kalinin, B. Mirman, E. Karapetian, Relationship between direct and converse piezoelectric effect in a nanoscale electromechanical contact, Phys. Rev. B. 76 (2007) 212102. https://doi.org/10.1103/PhysRevB.76.212102.

[140] K. Zhang, J.X.J.; Hoshino, Chapter 6 Mechanical Transducers: Cantilevers, Acoustic Wave Sensors, and Thermal Sensors, in: Mol. Sensors Nanodevices, Elsevier, Cambridge, MA, 2018. https://doi.org/10.1016/C2012-0-07668-5.

[141] M. Acosta, N. Novak, V. Rojas, S. Patel, R. Vaish, J. Koruza, G.A. Rossetti, J. Rödel, BaTiO 3 -based piezoelectrics: Fundamentals, current status, and perspectives, Appl. Phys. Rev. 4 (2017) 041305. https://doi.org/10.1063/1.4990046.

[142] T. Yamada, N. Niizeki, H. Toyoda, Piezoelectric and Elastic Properties of Lithium Niobate Single Crystals, Jpn. J. Appl. Phys. 6 (1967) 151–155. https://doi.org/10.1143/JJAP.6.151.

[143] P.X. Gao, Z.L. Wang, Nanoarchitectures of semiconducting and piezoelectric zinc oxide, J. Appl. Phys. 97 (2005) 044304. https://doi.org/10.1063/1.1847701.

[144] P. Kumar, S. Singh, O.P. Thakur, C. Prakash, T.C. Goel, Study of Lead Magnesium Niobate–Lead Titanate Ceramics for Piezo-Actuator Applications, Jpn. J. Appl. Phys. 43 (2004) 1501–1506. https://doi.org/10.1143/JJAP.43.1501.

[145] W. Ren, S.-F. Liu, B.K. Mukherjee, Nonlinear behavior of piezoelectric lead zinc niobate–lead titanate single crystals under ac electric fields and dc bias, Appl. Phys. Lett. 83 (2003) 5268–5270. https://doi.org/10.1063/1.1635069.

[146] O. Oralkan, A.S. Ergun, J.A. Johnson, M. Karaman, U. Demirci, K. Kaviani, T.H. Lee, B.T. Khuri-Yakub, Capacitive micromachined ultrasonic transducers: next-generation arrays for acoustic imaging?, IEEE Trans. Ultrason. Ferroelectr. Freq. Control. 49 (2002) 1596–1610. https://doi.org/10.1109/TUFFC.2002.1049742.

[147] B.T. Khuri-Yakub, Ö. Oralkan, Capacitive micromachined ultrasonic transducers for medical imaging and therapy, J. Micromechanics Microengineering. 21 (2011) 054004. https://doi.org/10.1088/0960-1317/21/5/054004.

[148] G. Wissmeyer, M.A. Pleitez, A. Rosenthal, V. Ntziachristos, Looking at sound: optoacoustics with all-optical ultrasound detection, Light Sci. Appl. 7 (2018) 53. https://doi.org/10.1038/s41377-018-0036-7.

[149] E. Zhang, J. Laufer, P. Beard, Backward-mode multiwavelength photoacoustic scanner using a planar Fabry-Perot polymer film ultrasound sensor for high-resolution three-dimensional imaging of biological tissues, Appl. Opt. 47 (2008) 561. https://doi.org/10.1364/AO.47.000561.

[150] C. Chao, S. Ashkenazi, S. Huang, M. O'Donnell, L. Guo, High-frequency ultrasound sensors using polymer microring resonators, IEEE Trans. Ultrason. Ferroelectr. Freq. Control. 54 (2007) 957–965. https://doi.org/10.1109/TUFFC.2007.341.

[151] D.H. Wang, P.G. Jia, Z.G. Ma, L.F. Xie, Q.B. Liang, Tip-sensitive fibre-optic Bragg grating ultrasonic hydrophone for measuring high-intensity focused ultrasound fields, Electron. Lett. 50 (2014) 649–650. https://doi.org/10.1049/el.2013.3961.

[152] P. Hajireza, W. Shi, K. Bell, R.J. Paproski, R.J. Zemp, Non-interferometric photoacoustic remote sensing microscopy, Light Sci. Appl. 6 (2017) e16278–e16278. https://doi.org/10.1038/lsa.2016.278.

[153] S.M. Maswadi, B.L. Ibey, C.C. Roth, D.A. Tsyboulski, H.T. Beier, R.D. Glickman, A.A. Oraevsky, All-optical optoacoustic microscopy based on probe beam deflection technique, Photoacoustics. 4 (2016) 91–101. https://doi.org/10.1016/j.pacs.2016.02.001.

[154] C.I. Zanelli, S.M. Howard, Schlieren metrology for high frequency medical ultrasound, Ultrasonics. 44 (2006) e105–e107. https://doi.org/10.1016/j.ultras.2006.06.062.

[155] A. Shrivastava, V. Gupta, Methods for the determination of limit of detection and limit of quantitation of the analytical methods, Chronicles Young Sci. 2 (2011) 21. https://doi.org/10.4103/2229-5186.79345.

[156] AOAC, Appendix F: Guidelines for Standard Method Performance Requirements, in: J. AOAC Int. Off. Method Anal., 2016: p. 9. http://www.eoma.aoac.org/app_f.pdf.

[157] J.M. Walker, A.M. Myers, M.D. Schluchter, V.M. Goldberg, A.I. Caplan, J.A. Berilla, J.M. Mansour, J.F. Welter, Nondestructive Evaluation of Hydrogel Mechanical Properties Using Ultrasound, Ann. Biomed. Eng. 39 (2011) 2521–2530. https://doi.org/10.1007/s10439-011-0351-0.

[158] E.Y. Zhu, C. Rewcastle, R. Gad, L. Qian, O. Levi, Sensing ultrasound optically with photonic crystal slabs: a tale of two mechanisms (Conference Presentation), in: A.A. Oraevsky, L. V. Wang (Eds.), Photons Plus Ultrasound Imaging Sens. 2019, SPIE, 2019: p. 20. https://doi.org/10.1117/12.2508998.

[159] E.Y. Zhu, M.C. Charles, C. Rewcastle, R. Gad, L. Qian, O. Levi, All-optical ultrasound sensing in photonic crystal slabs aided by PMMA (Conference Presentation), in: A.A. Oraevsky, L. V. Wang (Eds.), Photons Plus Ultrasound Imaging Sens. 2020, SPIE, 2020: p. 37. https://doi.org/10.1117/12.2545146.

[160] E.Y. Zhu, C. Rewcastle, R. Gad, L. Qian, O. Levi, Refractive-index-based ultrasound sensing with photonic crystal slabs, Opt. Lett. 44 (2019) 2609. https://doi.org/10.1364/ol.44.002609.

VITA

MEHENUR SARWAR

2010	B.A., Biochemistry & Molecular Biology Jahangirnagar University Savar, Bangladesh
2012	M.A., Biochemistry & Molecular Biology Jahangirnagar University Savar, Bangladesh
2022	M.S. & PhD, Biomedical Engineering Florida International University Miami, Florida

PUBLICATIONS

William, A., Li, C.Z., Sarwar, M. (2015). Paper-based 3D Cell Culture Devices for Rapid, Antibiotic Assays. Journal of the Mississippi Academy of Sciences

Zhu, X., Sarwar, M., Yue, Q., Chen, C., & Li, C. Z. (2017). Biosensing of DNA oxidative damage: a model of using glucose meter for non-glucose biomarker detection. International journal of nanomedicine, 12, 979.

Leichner, J., Sarwar, M., Nilchian, A., Zhu, X., Liu, H., Shuang, S., & Li, C. Z. (2017). Electrochemical lateral flow paper strip for oxidative-stress induced DNA damage assessment. In Biosensors and Biodetection (pp. 23-39). Humana Press, New York, NY.

Zhu, X., Sarwar, M., Zhu, J. J., Zhang, C., Kaushik, A., & Li, C. Z. (2019). Using a glucose meter to quantitatively detect disease biomarkers through a universal nanozyme integrated lateral fluidic sensing platform. Biosensors and Bioelectronics, 126, 690-696.

Sarwar, M., Leichner, J., Naja, G. M., & Li, C. Z. (2019). Smart-phone, paper-based fluorescent sensor for ultra-low inorganic phosphate detection in environmental samples. Microsystems & nanoengineering, 5(1), 1-10.

Sarwar, M., & Nilchian, A. (2019). 9.1 Nanomaterials and Toxicity. Toxicity of Nanomaterials: Environmental and Healthcare Applications, 215.

Sarwar, M., Nilchian, A., & Li, C. Z. (2019). Lab-on-a-Chip-Based Devices for Rapid and Accurate Measurement of Nanomaterial Toxicity. In Toxicity of Nanomaterials (pp. 215-241). CRC Press.

Sarwar, M., Rodriguez, P., & Li, C. Z. (2019). Sweat-Based in Vitro Diagnostics (IVD): From Sample Collection to Point-of-Care Testing (POCT). Journal of Analysis and Testing, 3(1), 80-88.

Ouyang, M., Tu, D., Tong, L., Sarwar, M., Bhimaraj, A., Li, C., ... & Di Carlo, D. (2021). A review of biosensor technologies for blood biomarkers toward monitoring cardiovascular diseases at the point of care. Biosensors and Bioelectronics, 112621.